Robotic System Development for Precision MRI-Guided

Needle-Based Interventions

by

Gang Li

A dissertation submitted to The Worcester Polytechnic Institute in conformity with

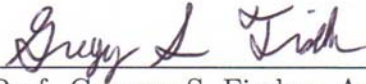the requirements for the degree of Doctor of Philosophy

in

Mechanical Engineering

Worcester, Massachusetts

June, 2016

Approved by:

_____
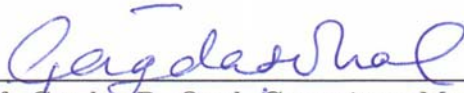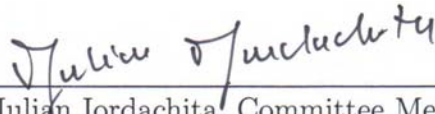Prof. Gregory S. Fischer, Advisor
Worcester Polytechnic Institute

_____
Prof. John M. Sullivan, Committee Member
Worcester Polytechnic Institute

_____
Prof. Cagdas D. Onal, Committee Member
Worcester Polytechnic Institute

_____
Prof. Iulian Iordachita, Committee Member
Johns Hopkins University

_____
Prof. Raghvendra V. Cowlagi, Graduate Committee Representative
Worcester Polytechnic Institute

Abstract

This dissertation describes the development of a methodology for implementing robotic systems for interventional procedures under intraoperative Magnetic Resonance Imaging (MRI) guidance. MRI is an ideal imaging modality for surgical guidance of diagnostic and therapeutic procedures, thanks to its ability to perform high resolution, real-time, and high soft tissue contrast imaging without ionizing radiation. However, the strong magnetic filed and sensitivity to radio frequency signals, as well as tightly confined scanner bore render great challenges to developing robotic systems within MRI environment. Discussed are potential solutions to address engineering topics related to development of MRI-compatible electro-mechanical systems and modeling of steerable needle interventions.

A robotic framework is developed based on a modular design approach, supporting varying MRI-guided interventional procedures, with stereotactic neurosurgery and prostate cancer therapy as two driving exemplary applications. A piezoelectrically actuated electro-mechanical system is designed to provide precise needle placement in the bore of the scanner under interactive MRI-guidance, while overcoming the chal-

lenges inherent to MRI-guided procedures. This work presents the development of the robotic system in the aspects of requirements definition, clinical workflow development, mechanism optimization, control system design and experimental evaluation.

A steerable needle is beneficial for interventional procedures with its capability to produce curved path, avoiding anatomical obstacles or compensating for needle placement errors. Two kinds of steerable needles are discussed, i.e. asymmetric-tip needle and concentric-tube cannula. A novel Gaussian-based ContinUous Rotation and Variable-curvature (CURV) model is proposed to steer asymmetric-tip needle, which enables variable curvature of the needle trajectory with independent control of needle rotation and insertion. While concentric-tube cannula is suitable for clinical applications where a curved trajectory is needed without relying on tissue interaction force.

This dissertation addresses fundamental challenges in developing and deploying MRI-compatible robotic systems, and enables the technologies for MRI-guided needle-based interventions. This study applied and evaluated these techniques to a system for prostate biopsy that is currently in clinical trials, developed a neurosurgery robot prototype for interstitial thermal therapy of brain cancer under MRI guidance, and demonstrated needle steering using both asymmetric tip and pre-bent concentric-tube cannula approaches on a testbed.

iv

Acknowledgments

I would first like to express my gratitude to my advisor Prof. Gregory S. Fischer for his mentoring, guidance and support throughout the years of my PhD study. Prof. Fischer has been an incredible supervisor and is knowledgeable in all aspects of medical robotics. His academic enthusiasm and technical expertise has enriched my insights to the research of medical robotics and sets solid foundation of that. Prof. Fischer has provided me so much intellectual support, academic guidance and professional assistance, which have been invaluable treasure for my doctoral research.

I want also to thank Prof. John Sullivan, Prof. Cagdas Onal, Prof. Iulian Iordachita, and Prof. Raghvendra Cowlagi for serving on my thesis committee as committee members and representative. Their insightful reviews have improved the content throughout the dissertation.

I want to acknowledge our collaborators who provide valuable engineering and clinical contributions for this dissertation: Prof. Clare Tempany, Prof. Nobuhiko Hata and Prof. Junichi Tokuda from Brigham and Women's Hospital, Harvard Medical School; Prof. Iulian Iordachita and Dr. Sohrab Eslami from Johns Hopkins Univer-

sity; Prof. Julie Pilitsis from Albany Medical College; Prof. Matt Gounis and Dr.
Shaokuan Zheng from Umass Medical School; Prof. Reinhold Ludwig and Prof. Gene
Bogdanov from WPI; Prof. Robert J. Webster III from Vanderbilt University; Prof.
D. Caleb Rucker from University of Tennessee; Dr. Clif Burdette, Emery Williams,
Tamas Heffter, and Paul Neubauer from Acoustic MedSystems Inc.; Prof. Sarthak
Misra, Dr. Pedro Moreira, and Tim van Katwijk from University of Twente.

I would also like to thank my lab mates from Automation and Interventional
Medicine (AIM) Robotics Research Laboratory for collaborative work and friendship:
Nirav Patel, Marek Wartenberg, Chris Nycz, Adnan Munawar, Paulo Carvalho, Alex
Camilo, Kevin Harrington, Hao Su, Weijian Shang, Wenzhi Ji, Yunzhao Ma, Hanlin
Hong, Yi Wang, Xiaoan Yan, Zhixian Zhang, Miaobo Li, Michael Delph, Gregory
Cole, and Satya Janga. I have very much enjoyed our days and nights working in the
lab.

I want to thank mechanical and robotics engineering staff: Barbara Edilberti, Bar-
bara Furhman, Randy Robinson, Erica Stults, Deborah Baron, and Shannon Cotter
for their generous and patient help.

Finally, I am deeply thankful to my family and my wife, for their love, under-
standing, encouragement and support. I could never have come this far without

them.

This work would not have been possible without the help and support of my family, advisor, colleagues and friends. I would like to expressly thank everyone who has helped me over the past 5 years of my PhD life.

Dedication

This dissertation is dedicated to my wife Yan Liu, my parents Qingong Li and Qinglan Bu, and my sister Hongyan Li.

Contents

List of Tables

List of Figures

Acronyms

ABS Acrylonitrile Butadiene Styrene

ASTM The American Society for Testing and Materials

CAD Computer Aided Design

CT Computed Tomography

CURV ContinUous Rotation and Variable-curvature

DOF Degree of Freedom

FDA Food and Drug Administration

FPGA Field Programmable Gate Array

FPI Fabry-Perot Interferometer

MRI Magnetic Resonance Imaging

MRTI Magnetic Resonance Thermal Imaging

NEMA National Electronic Manufacturers Association

NIH National Institutes of Health

IGT Image-Guided Therapy

IRB Institutional Review Board

OTS Optical Tracking System

PEEK Polyetheretherketone

PID Proportional-Integral-Derivative

RAS Right Anterior Superior

RF Radio Frequency

RMS Root Mean Square

SNR Signal-to-Noise Ratio

TRUS Transrectal Ultrasound

US Ultrasound

Chapter 1

Introduction

Needle-based percutaneous interventions are common approaches for diagnostic and therapeutic procedures including tissue biopsy, delivery of therapeutic agents, and tumor ablation. Image-guided therapy (IGT) affords higher precision and greater outcomes for interventional procedure, by providing visualized anatomic structure feedback during a procedure. Magnetic resonance imaging (MRI) is an ideal guidance tool for IGT due to its ability to perform high quality, real-time, volumetric imaging without ionizing radiation. However, the strong magnetic and radio frequency field, as well as the tightly confined scanner bore renders great challenges to the development of robotic system that is compatible to MRI environment. This thesis addresses the fundamental challenges of MRI-guided robotic interventional system and enables the technologies for MRI-guided stereotactic neurosurgery, prostate cancer therapy and steerable needle intervention.

1.1 Background and Motivation

Image-guided therapy is a common approach for interventional procedures, which integrates advanced medical imaging and navigation with surgical workflow to localize, visualize, monitor and target clinical procedures. IGT can improve the conventional interventions with enhanced precision and superior outcomes. However, for most current image-guided approaches only static pre-operative images are accessible for guidance, which are unable to provide live and updated information during a surgical procedure. Therefore, there is an essential unmet need for introducing intra-operative imaging into the clinical workflow, and enabling the incorporation of human experience and intelligence in a controlled, closed-loop fashion. MRI is an ideal imaging modality for surgical guidance of diagnostic and therapeutic procedures, with its ability to perform high resolution, real-time, high soft tissue contrast imaging without ionizing radiation. Robotic assistance can enable high accuracy and reliability surgical procedures, and can streamline the clinical workflow. Integrating the advanced robotic techniques with intra-operative MRI guidance offers significant benefits for surgical procedures. But, the high magnetic field, electrical interference, and limited access of closed-bore MRI render great and unique challenges to developing robotic systems that can perform inside a diagnostic high-field MRI while obtaining interactively updated MR images.

1.1.1 Interventional MRI for Diagnostic and Therapeutic Procedures

MRI has unmatched potential advantages over other medical imaging counterparts, such as Computed Tomography (CT) and Ultrasound, making it an excellent guidance tool for interventional procedures. The major advantages of MRI includes:

1) High spatial resolution and soft tissue contrast, allows precise detection and localization of suspicious focal lesion, and avoid critical physiological structure in the insertion pathway [1], which is ideal for soft tissue such as prostate and brain tissue etc.;

2) Real-time and arbitrary plane imaging, enables intra-operative continuous tracking of surgical tools and on-the-fly adjustment of imaging plane. It enables closed-loop control of needle insertion with dynamic image-based position feedback, as discussed in Sec. 4.2.4;

3) Multi-parameters imaging, such as MR thermal imaging (MRTI), functional MRI (fMRI), diffusion, dynamic contrast, various weightings, etc.. This unique imaging feature allows visualization and monitoring biomechanical and physiological tissue properties, such as thermal monitoring for brain tumor ablation, as introduced in Sec. 2.3;

4) Providing no ionizing radiation safety hazard to patient and clinicians.

1.1.2 Motivation of Robotic System for MRI-Guided Therapy

Integrating the robotic technologies with interventional MRI could essentially benefit the clinical procedures with greater outcomes, in the following aspects:

1) Increase accuracy. Robot mechanism could be designed incredible dexterous, stable, and reliable, attenuating errors caused by manual operation, such as vibrations. With high resolution sensor, position feedback, and closed-loop control, robotic system can perform micro scale positioning.

2) Improved workflow. With powerful computing and sensory capability, the robotic system is able to reduce the computational burden of clinicians to register and track the surgical tools and targets. With simultaneous imaging and robotic manipulation, it could also alleviate the necessity of iterative and time-consuming procedures to move in patient for imaging and move out of bore for interventions.

3) Enhanced ergonomics. The tightly confined closed-bore scanner (60-70cm in diameter and 170cm in length) leads to awkward ergonomics for performing intervention manually. Using the robot-assisted device could eliminate the needs to manually place the needle inside the scanner bore.

1.1.3 Challenges and Requirements for MRI-Compatible Robotic System

Challenges of developing robotic systems in the MRI environment include: 1) the tightly confined scanner bore (typically $60-70cm$ in diameter) restricts the accessible space and results in awkward ergonomics for manually placing surgical tools inside the MRI machine; and 2) the strong magnetic (usually 1.5T to 3T) and radio frequency (RF) fields. Ferromagnetic materials can be exposed to extremely strong magnetic force and may be a fatal safety hazard. Hence, electromagnetic actuators (e.g. typical DC motors), are contraindicated for use in the MRI room. Further, electric signals may cause significant image degradation due to electromagnetic interference. The American Society for Testing and Materials (ASTM) classified the devices for the MRI environment as MR safe, MR Conditional and MR Unsafe (ASTM F2503), as summarized in Table. 1.1.

Significant efforts have been made to overcome these critical issues for MRI-compatible robotic systems. In terms of actuation principles, MRI-guided robotic assistants may be classified as hydraulic, pneumatic, and piezoelectric actuation. Hydraulic actuation potentially could be MRI-safe, but it is seldom employed in MRI robots because of the potential for fluid leakage and cavitation [2] as well as the inconvenience of having to reset a closed hydraulic system for each use if not permanently installed. Pneumatic actuation fundamentally can be designed MRI-safe, and pneu-

Table 1.1: ASTM Classification for Items in The MRI Environment

Term	Icon	Definition
MR Safe	MR	An item that poses no known hazards resulting from exposure to any MR environment. MR Safe items are composed of materials that are electrically nonconductive, nonmetallic, and nonmagnetic.
MR Conditional	/MR\	An item with demonstrated safety in the MR environment within defined conditions. At a minimum, address the conditions of the static magnetic field, the switched gradient magnetic field and the radiofrequency fields. Additional conditions, including specific configurations of the item, may be required.
MR Unsafe	MR	an item which poses unacceptable risks to the patient, medical staff or other persons within the MR Environment

matically actuated MRI robotic systems based on pneumatic cylinders include [3–5]. Custom pneumatic actuators such as the PneuStep pneumatic step motor were developed by Stoianovici et al. [6], and have been adopted for prostate interventions [7,8]. Schouten et al. presented a pneumatic turbine-based actuator [9] and tested it clinically for MRI-guided transrectal prostate biopsy [10]. A servo-pneumatic drive system developed by Innomotion (Innomedic, Herxheim, Germany) was applied to the first cadaver study of transgluteal biopsies [11], and then tested clinically in patients [12]. Although the pneumatic actuation has the intrinsic features of being MRI-safe, its major limitations are the difficulty of precise and stable servo control, especially when long pneumatic transmission line is utilized, and the typically relatively bulky profile.

Nonmagnetic piezoelectric actuators, in contrast, are able to provide high precision positioning (submicron) with excellent dynamic performance. Moreover, they can be

made compact in size with high power density. Song et al. presented a 2-DOF motorized needle guide template with ultrasonic motors to resemble the conventional TRUS-guided prostate intervention [13]. Krieger et al. designed a compact prototype of piezoelectrically actuated robot for transrectal MRI-guided needle intervention with 2-DOF motorized needle driver mounted on a 6-DOF passive arm [14]. Nevertheless, significant image degradation is a major problem for piezoelectric actuators that utilize off-the-self drivers. MR image signal-to-noise ratio (SNR) may be reduced by as much as 80% without RF shielding, and even with RF shielding the SNR may still be degraded by 40% - 60% [14, 15].

1.1.4 Motivation of Steerable Needle Intervention

Percutaneous needle-based interventions are common approaches for diagnostic and therapeutic procedures including tissue biopsy, delivery of therapeutic agents, and tumor ablation. Straight needle insertion paths are typically applied for such procedures, but in some cases specified paths with preplanned curves are required to avoid anatomical obstacles (e.g. delicate organs, vasculature, nerves, and bones), or compensate for placement errors, or reach varying region through single entry point. Fig. 1.1, demonstrates the examples of merits of steerable needle intervention. However, following a desired path within the tissue is challenging, due to needle deflection, tissue deformation, patient movement, image registration, and other sources of error during the interventions. Therefore, steerable needles are investigated with consider-

able research effort for its capability to produce curved trajectory in the narrow and winding scenario.
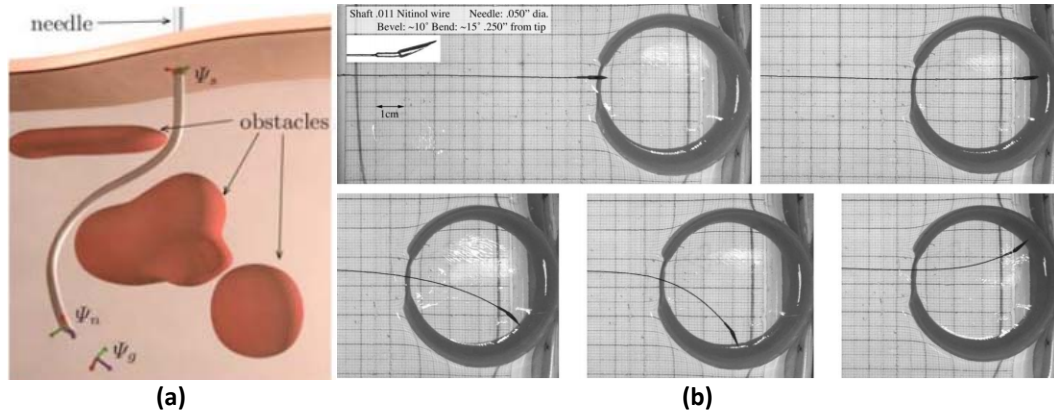
Figure 1.1: Example of merits of steerable needle intervention. (a) avoiding anatomical obstacles [16] ©Springer-Verlag Berlin Heidelberg 2010. (b) reaching varying area through single entry point [17] ©2010 by the Congress of Neurological Surgeons.

1.2 Literature Review

MRI-guided robotic systems have been developed for a wide range of applications. In this dissertation, my research endeavors focus on the applications for stereotatic neurosurgery, prostate cancer therapy and steerable needle interventions. Related work is discussed in this section.

1.2.1 MRI-Guided Neurosurgery Robots

Stereotactic neurosurgery is one of most commonly investigated clinical procedures using MRI-guided robotics technologies, thanks to its excellent brain tissue imaging.
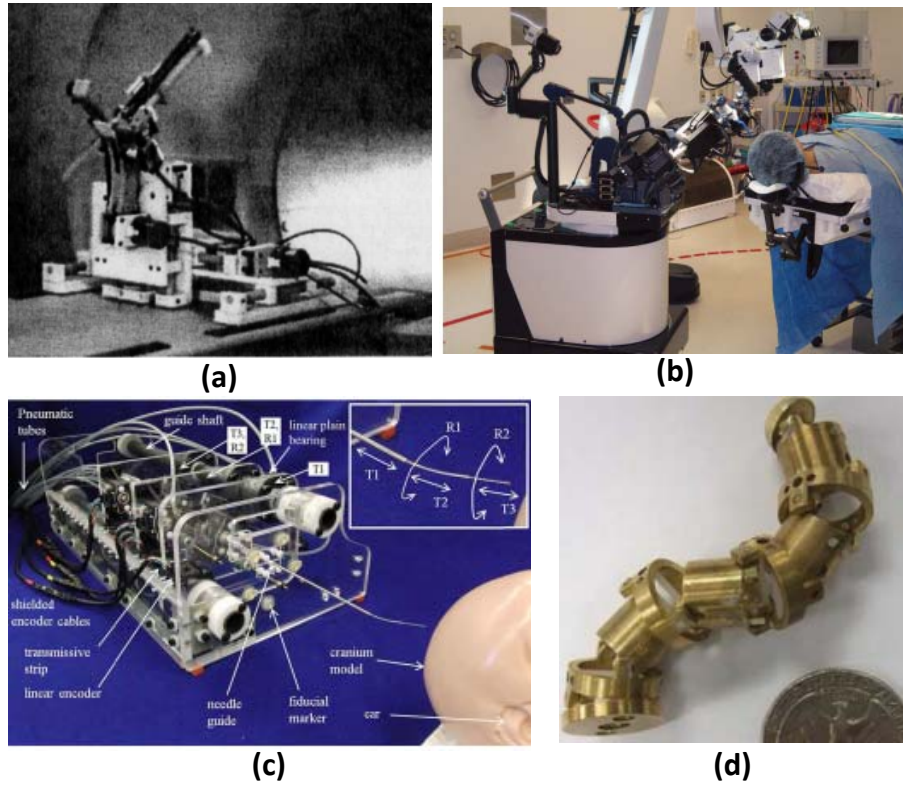
Figure 1.2: Examples of MRI-compatible neurosurgical robot. (a) Ultrasonically actuated needle insertion manipulator for stereotactic neurosurgery [18] ©1996 Wiley-Liss, Inc. (b) neuroArm, a teleoperated surgical robotic system with intraoperative MRI [19] ©2008 IEEE. (c) Precision pneumatic active cannula Robot, [20] ©2014 ASME. (d) Meso-scale SMA-actuated MRI-compatible neurosurgical robot [21] ©2011 IEEE.

Masamune et al. [18] designed an MRI-guided robot for neurosurgery with ultrasonic motors (USR30-N4, Shinsei Corporation, Japan) inside low field strength scanners (0.5 Tesla) in 1995. Sutherland et al. [22] developed NeuroArm robot, a manipulator consisting of dual dexterous arms driven by piezoelectric motors (HR2-1N-3, Nanomotion Ltd, Israel) for operation under MR guidance. Since this general purpose neurosurgery robot aims to perform both stereotaxy and microsurgery with a number of tools, the cost could be formidably high. Ho et al. [21] developed a shape-

9

memory-alloy driven finger-like neurosurgery robot. This technology shows promise, however, it is still in the early development and requires high temperature intracranially with very limited bandwidth. Comber et al. [20] presented a pneumatically actuated concentric tube robot for MRI-guided neurosurgery. However, the inherent nonlinearity and positioning limitation of pneumatic actuation, as demonstrated in [23], present significant design challenge. Augmented reality has also been shown effectiveness to improve the MRI-guided interventions by Liao et al. [24] and Hirai et al. [25].

1.2.2   MRI-Guided Prostate Robots

MRI-guided robotic systems for prostate cancer therapy have been studied extensively from varying clinical perspectives, including transperineal, transrectal and transgluteal approaches. From the actuation perspective, they can classified as hydraulic, pneumatic, and piezoelectric actuation.

Hydraulic actuation potentially could be MRI-safe, but it is seldom employed in MRI robots because of the potential for fluid leakage and cavitation [2] as well as the inconvenience of having to reset a closed hydraulic system for each use if not permanently installed.

Pneumatic actuation fundamentally can be designed MRI-safe. Based on typical pneumatic cylinders, Fischer et al. [3] designed a pneumatically actuated robotic system for prostate biopsy and intervention, and further refined by Song et al [4],
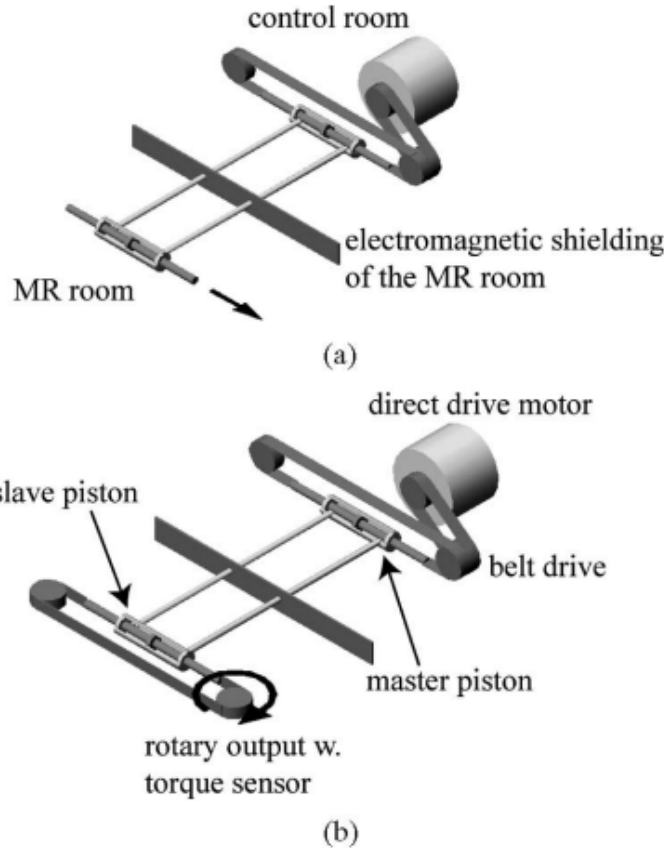
Figure 1.3: Example of MR-compatible (a) linear and (b) rotary actuator concept with hydrostatic transmission. [2] ©2006 IEEE

replacing the 2-DOF Cartesian motion with a 4-DOF parallel platform enabling needle angulation. Custom pneumatic actuators such as the PneuStep pneumatic step motor were developed by Stoianovici et al. [6], and have been adopted for prostate interventions [7,8]. Schouten et al. presented a pneumatic turbine-based actuator [9] and tested it clinically for MRI-guided transrectal prostate biopsy [10]. A servo-pneumatic drive system developed by Innomotion (Innomedic, Herxheim, Germany) was applied to the first cadaver study of transgluteal biopsies [11], and then tested clinically in patients [12]. Although the pneumatic actuation has the intrinsic fea-

tures of being MRI-safe, its major limitations are the difficulty of precise and stable

servo control, especially when long pneumatic transmission line is utilized, and the

typically relatively bulky profile.

Figure 1.4: Examples of pneumatically actuated prostate robot: (a) 4-DOF needle guide pneumatic robot [3] ©2008 IEEE; (b)4-DOF robot for MRI-guided transperineal prostate needle placement. [4] ©2012 John & Wiley Sons, Ltd.;(c)MRI-compatible robot with six PneuStep motors [6] ©2007 IEEE;(d) MR-compatible Robot for Transrectal Prostate Biopsy. [10] ©2011 RSNA.

Piezoelectric actuators are able to provide high precision positioning (submicron)

with excellent dynamic performance and compact footprint. Song et al. presented a

2-DOF motorized needle guide template with ultrasonic motors to resemble the con-

ventional TRUS-guided prostate intervention [13]. Krieger et al. designed a compact

prototype of piezoelectrically actuated robot for transrectal MRI-guided needle inter-

vention with 2-DOF motorized needle driver mounted on a 6-DOF passive arm [14].

Nevertheless, significant image degradation is a major problem for piezoelectric actu-

ators that utilize off-the-self drivers. MR image signal-to-noise ratio (SNR) may be

reduced by as much as 80% without RF shielding, and even with RF shielding the

SNR may still be degraded by 40% - 60% [14, 15].
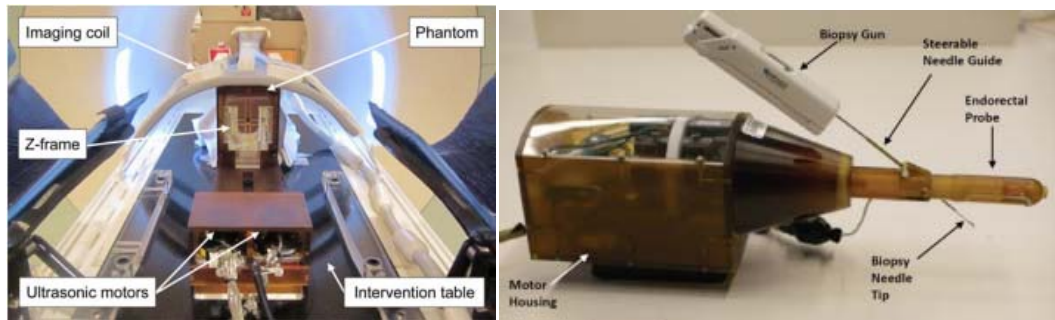
Figure 1.5: Examples of piezoelectrically actuated prostate robot: (left) ultrasonic actuated needle guide template [13] ©2013 IEEE; (right)APT-III actuated robot for prostate intervention [14] ©2011 IEEE.

1.2.3   Steerable Needle Intervention

Approaches for steering flexible needles have been investigated with great efforts,

including tip-based needle steering [26], pre-curved needle manipulating [27], concen-

tric continuum tubes [28,29], and actuated flexible needles [30–33]. Instead of steering

the needle itself within the tissue, approaches for manipulating the base [34, 35] or

tissue [36] also have been proposed to achieve desired needle path. Moreover, special

shapes of asymmetric tips are also investigated, including an airfoil tip [37] and a

bio-inspired programmable bevel tip [38]. A comprehensive review of robotic needle

steering approaches is summarized in [39,40]. Fig. 1.6 illustrates the common mech-
anisms to steer the needle, and Fig. 1.7 summarizes the example robotic devices for
varying steering method.
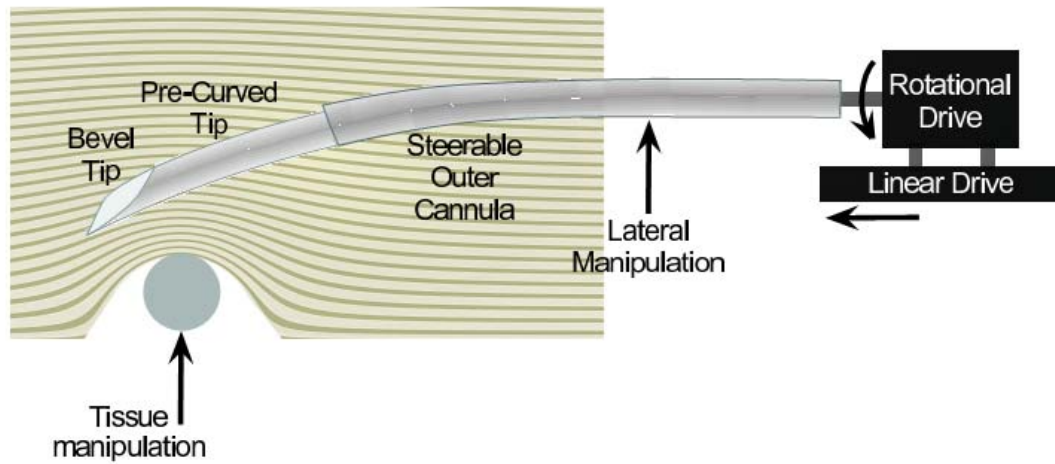
Figure 1.6: Schematic diagram illustrating the common mechanisms to steer the
needle: asymmetric tip, pre-curved tip, lateral manipulation, tissue manipulation
and steerable cannula [39]. ©2011 Springer.

Figure 1.7: Example robotic devices for varying steering method [39]. ©2011 Springer.

1.3   Dissertation Contributions

The endeavors of this dissertation are to address research topics related to developing MRI-compatible electromechanical systems and modeling steerable needle interventions, to enable the technologies for the development of MRI-guided robotic systems. The major contributions of this dissertation are summarized as follows:

System Development for MRI-Guided Interventions

Developed a robotic framework for implementing MRI-guided interventions based on a modular design approach, including requirements definition, workflow development, mechanism design, system integration, control algorithm modeling and implementation. The proposed modular design approach makes the system readily transported and setup for supporting clinical workflow of MRI-guided procedures, as well as readily extensible and reconfigurable to other clinical applications.

Robotic System for MRI-Guided Stereotactic Neurosurgery

Designed two generations of MRI-compatible robot that is kinematically equivalent to a Leksell frame for stereotatic neurosurgery. Analyzed robot-assisted workflow and demonstrated the potential to reduce procedure time. Evaluated the imaging quality and targeting accuracy of the robotic system.

Robotic System for MRI-Guided Transperineal Prostate Interventions

Developed robot motion control system and integrated system modules for a clinical grade system for prostate biopsy, which has been approved by the Institutional Review Board (IRB) for clinical trials on human. Evaluated the clinical grade system

with pre-clinical MRI phantom studies and a preliminary patient study. Assisted the clinical team to perform 18 clinical trials of prostate biopsy. Developed and evaluated a fully actuated robotic system for automated prostate biopsy and brachytherapy.

MRI-Guided Steerable Needle Interventions

Proposed a novel Gaussian-based ContinUous Rotation and Variable-curvature (CURV) steering approach, enabling effective variable curvature control with continuous smooth rotation and independent insertion control. Implemented closed-loop control of CURV steering under continuous intraoperative MRI-guidance, correcting the modeling error on-line and improving position accuracy. Validated the CURV steering model and closed-loop control approach with phantom studies. Integrated the concentric tube continuum robotics with advanced MRI-guidance techniques. Demonstrated available redundancy of MRI-guided concentric tube continuum robot. Assessed the system accuracy with MRI phantom and ex vivo tissue studies.

1.4 Dissertation Overview

This dissertation discussed three main studies of MRI-guided interventional procedures, namely 1) stereotactic neurosurgery, 2) prostate cancer therapy, and 3) steerable needle interventions. This introductory chapter introduces the background and motivation for intraoperative MRI-guided robotic system, and related work on MRI-guided robotic systems.

Chapter 2 presents the design of two generations of robotic system for MRI-guided stereotactic neurosurgery. A 5-DOF electrode alignment robot with manual lead insertion is firstly designed for Deep Brain Stimulation (DBS). Based on it, an 8-DOF fully actuated robotic assistant is further developed for performing MRI-guided precision conformal ablation of brain tumors. The architecture and clinical workflow of the system is presented, the electromechanical and motion control system design is described, and the system is evaluated in the aspects of MRI-compatibility and targeting accuracy within MRI environment.

Chapter 3 describes the development of two generations of robotic system for MRI-guided prostate cancer therapy. A clinical grade 4-DOF parallel needle placement manipulator with manual insertion is first designed for transperineal prostate biopsy. Secondly, a prototype version 6-DOF fully actuated robotic assistant is presented for autonomous prostate biopsy and brachytherapy. The clinical grade system has been approved by the institutional review board (IRB) for clinical trials. First-in-man trials to evaluate the system's effectiveness and accuracy for MR image-guided prostate biopsy are underway. This chapter articulates the architecture and clinical workflow of the system, electromechanical design, and navigation and robot control software. The system is assessed with pre-clinical phantom study and preliminary clinical study under live MRI-guidance. The fully actuated prototype system is discussed to leverage the robotic system to enable simultaneous needle placement and MR imaging.

Chapter 4 reports the modeling and control of two methods of steerable needle

interventions, namely Gaussian-based ContinUous Rotation and Variable-curvature (CURV) steering model, and concentric-tube continuum robot. First, a novel CURV steering approach is proposed based on the nonholonomic kinematic model, which enables variable curvature of the needle trajectory with independent control of needle rotation and insertion. Closed-loop control of CURV steering model is further implemented using continuously acquired intraoperative MR images as position feedback, which could compensate modeling error and increase the positioning accuracy. Second, a concentric-tube continuum robot is studied, allowing MRI-guided deployment of a precurved and steerable concentric tube continuum mechanism, which is suitable for clinical applications where a curved trajectory is needed.

This dissertation is concluded and future work is discussed in Chapter 5.

Chapter 2

Robotic System for MRI-Guided Stereotactic Neurosurgery

This chapter presents the development of two generations of robotic system for stereotactic neurosurgery under live MRI-guidance. A 5-DOF electrode alignment robot with manual lead insertion is firstly designed for Deep Brain Stimulation (DBS). Based on it, an 8-DOF fully actuated robotic assistant is further developed for performing MRI-guided precision conformal ablation of brain tumors.

Utilizing the modular hardware and software, the 5-DOF electrode alignment robot for DBS with manual lead insertion offers the potential of reducing procedure duration while improving targeting accuracy and enhancing safety. This is achieved through simultaneous robotic manipulation of the instrument and interactively updated in situ MRI guidance that enables visualization of the anatomy and interventional

instrument. During simultaneous actuation and imaging, the system has demonstrated less than 15% signal-to-noise ratio (SNR) variation and less than 0.20% geometric distortion artifact without affecting the imaging usability to visualize and guide the procedure. Optical tracking and MRI phantom experiments streamline the clinical workflow of the prototype system, corroborating targeting accuracy with 3-axis root mean square error $1.38 \pm 0.45mm$ in tip position and $2.03 \pm 0.58°$ in insertion angle.

Based on the endeavor of earlier version of manual insertion, an 8-DOF fully actuated robotic assistant is further developed. The improved design with motorized ablator manipulator enables fully actuated mechanism with compact profile. Fully actuated mechanisms inside the scanner bore makes it readily to utilize real-time MRI-guidance during the procedures, alleviating the needs for moving the patient out of the scanner and streaming the workflow.

Some sections of this chapter has been published as "Robotic System for MRI-Guided Stereotactic Neurosurgery", IEEE Transactions on Biomedical Engineering, 2015 [41]. This work is performed in collaboration with Julie G. Pilitsis at Albany Medical Center; Matt Gounis at University of Massachusetts Medical School; Clif Burdette at Acoustic MedSystems Inc.

2.1   Introduction

Stereotactic neurosurgery enables surgeons to target and treat diseases affecting deep structures of the brain, such as through stereotactic electrode placement for deep brain stimulation (DBS), and thermal ablator delivery for brain tumor ablation. However, the procedure is still very challenging and often results in non-optimal outcomes. This procedure is very time-consuming, and may take $5-6$ hours with hundreds of steps. It follows a complicated workflow including preoperative MRI (typically days before the surgery), preoperative Computed Tomography (CT), and intraoperative MRI-guided intervention (where available). The procedure suffers from tool placement inaccuracy that is related to errors in one or more steps in the procedure, or is due to brain shift that occurs intraoperatively. According to [42], the surface of the brain is deformed by up to 20 mm after the skull is opened during neurosurgery, and not necessarily in the direction of gravity. The lack of interactively updated intraoperative image guidance and confirmation of instrument location renders this procedure nearly "blind" without any image-based feedback.

Deep Brain Stimulation

DBS, one clinical focus of this chapter, is a surgical implant procedure that utilizes a device to electrically stimulate specific structures, as shown in Fig. 2.1. DBS is commonly used to treat the symptoms of motion disorders such as Parkinson's disease, and has been shown effective for various other disorders including obsessive-compulsive disorder and severe depression. Unilateral lead is implanted to the sub-

thalamic nucleus (STN) or globus pallidus interna (GPi) for Parkinson's disease and dystonia. While bilateral leads are implanted to the ventral intermediate nucleus of the thalamus (VIM). Recently, improvement in intervention accuracy has been achieved through direct MR guidance in conjunction with manual frames such as the NexFrame (Medtronic, Inc, USA) [43] and Clearpoint (MRI Interventions, Inc., USA) [44] for DBS. However, four challenges are still not addressed. First, manual adjustment of the position and orientation of the frame is non-intuitive and time-consuming. Moreover, the clinician needs to mentally solve the inverse kinematics to align the needle. Second, manually-operated frames have limited positioning accuracy, inferior to a motorized closed-loop control system. Third, the operational ergonomics, especially the hand-eye coordination, is awkward during the procedure (the operator has to reach about 1 meter inside the scanner) while observing the MRI display (outside of the scanner). Fourth, most importantly, real-time confirmation of the instrument position is still lacking.

Brain Tumor Ablation

Brain metastases (BM), the other clinical focus of this chapter, are the most common site of metastases from systemic cancer in North America. 1.6 million Americans are diagnosed with cancer annually and 25% to 40% of them develop BM. Craniotomy can be effective for tissue diagnosis, rapid relief of symptoms, and local disease control, but it is highly invasive and has a 5% risk of complications that can affect quality of life. Stereotactic radio surgery (SRS) or whole brain radiation therapy
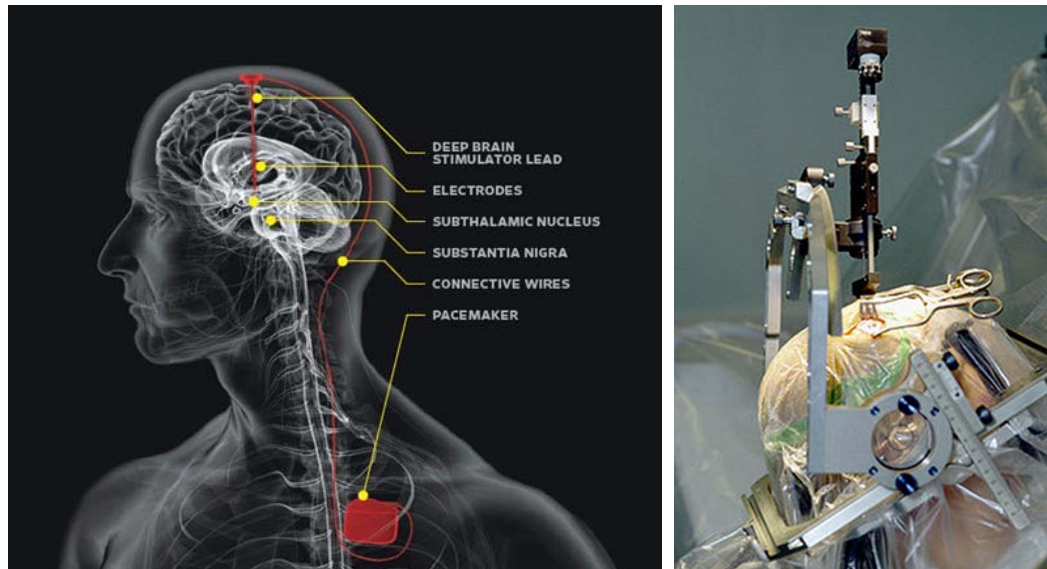
Figure 2.1: (Left)Diagram of DBS electrode implantation device (Credit: biomed.brown.edu). (Right) Stereotactic neurosurgery for DBS with Leksell frame (right)(Credit:wikipedia.org).

(WBRT), in contrast, is a non-invasive approach that can provide meaningful benefit and improve survival, but symptom relief is longer and diagnostic confirmation is not allowed. In addition, non-pathologic tissue at the periphery of tumor is often radiated, and thereby use of radiation near vital structures (e.g. optic nerve or brainstem) is limited. Interstitial conformal ablative ultrasound offers an alternative option that is less invasive than craniotomy but allows for immediate tissue diagnosis, enabling rapidly lower tumor burden beginning within 2-3 days of treatment and substantially more over a 3-4 week period. The current technical challenge is how to deliver an ultrasonic thermal ablator to a BM accurately and efficiently. Existing commercially available manual stereotactic frames, like Leksell and NexFrame have to be firmly mounted on the skull or scalp, which may cause incisions to the patient. Moreover,

manual adjustment of the frame is time consuming and may also introduce needle placement errors. Fig. 2.2 shows the MR images of brain tumor, and a treatment approach with laser probe.
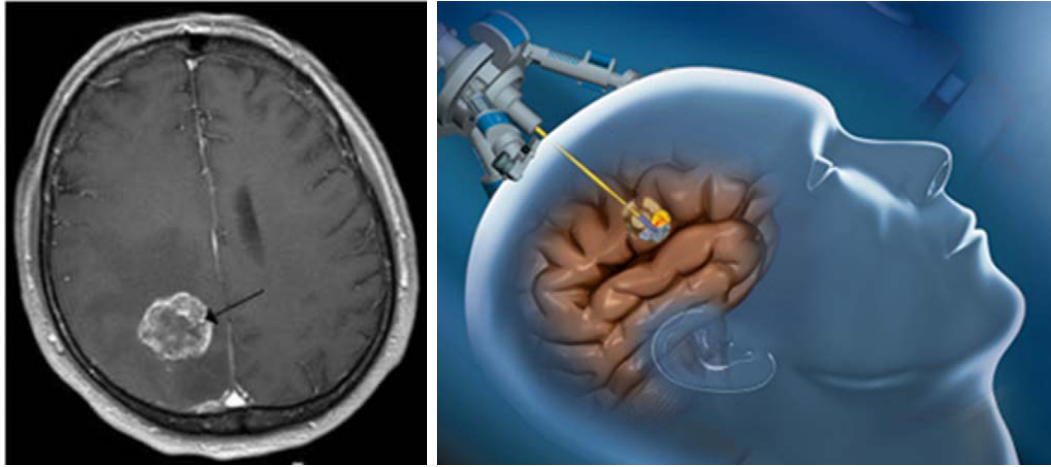
Figure 2.2: (Left)Brain metastasis in the right cerebral hemisphere from lung cancer on MRI (Credit:wikipedia.org). (Right) Brain tumor treatment with laser probe (Credit: Monteris NeuroBlate System).

There is a critical unmet need for an alternative approach that is more efficient, more accurate, and safer than traditional stereotactic neurosurgery or manual MR-guided approaches. To address these unmet clinical needs, this chapter proposes a piezoelectrically-actuated needle placement robotic assistant that allows simultaneous imaging and intervention without negatively impacting MR image quality for neurosurgery, specifically for DBS lead placement and brain tumor ablation. The primary contributions of this chapter include: 1) design of two generations MRI-guided robot that is kinematically equivalent to a Leksell frame; 2) a piezoelectric motor control system that allows simultaneous robot motion and imaging without affecting the imaging usability to visualize and guide the procedure; 3) robot-assisted work-

flow analysis demonstrating the potential to reduce procedure time, and 4) imaging quality and accuracy evaluation of the robotic system.

2.2 Precision Deep Brain Stimulation Probe Placement

In this section, we first discuss the study of the 5-DOF electrode alignment robot with manual lead insertion for deep brain stimulation.

2.2.1 System Architecture

A modular design approach is utilized to develop the system, supporting many typical needle-based percutaneous interventions. This system comprises five major modules: 1) navigation and treatment planning software, 2) robot control interface software, 3) MRI robot controller, 4) the interventional robot, and 5) MRI scanner, as shown in Fig. 2.3. The open-source image navigation software 3D Slicer [45] is utilized to visualize and select targets in the image space, as well as generate treatment plan. The robot control software is designed to organize the dataflow and solve robot kinematics. Custom developed MRI compatible robot controller provides high-precision closed-loop position control of the robot manipulator with sensory feedback on each axis, such as positioning encoders. The desired targets are selected on navi-

gation software and sent to robot control software via OpenIGTLink communication protocol [46]. Therein, the targets position are resolved to motion commands of each joint based on robot kinematics and then transmitted to the controller to drive the motors and thus place the probe to desired targets. Data transmission between robot control software (running on a laptop inside control console room) and robot controller (residing inside MRI scanner room) is established via fiber optic Ethernet, which runs through the shielded patch panel, to eliminate electric noise that may be introduced into imaging due to transmission of electrical signals. The actual probe position is fed back to navigation software for visualization and verification. Fig. 2.4 shows the configuration of the MRI-guided robotic neurosurgery system inside MRI scanner environment.
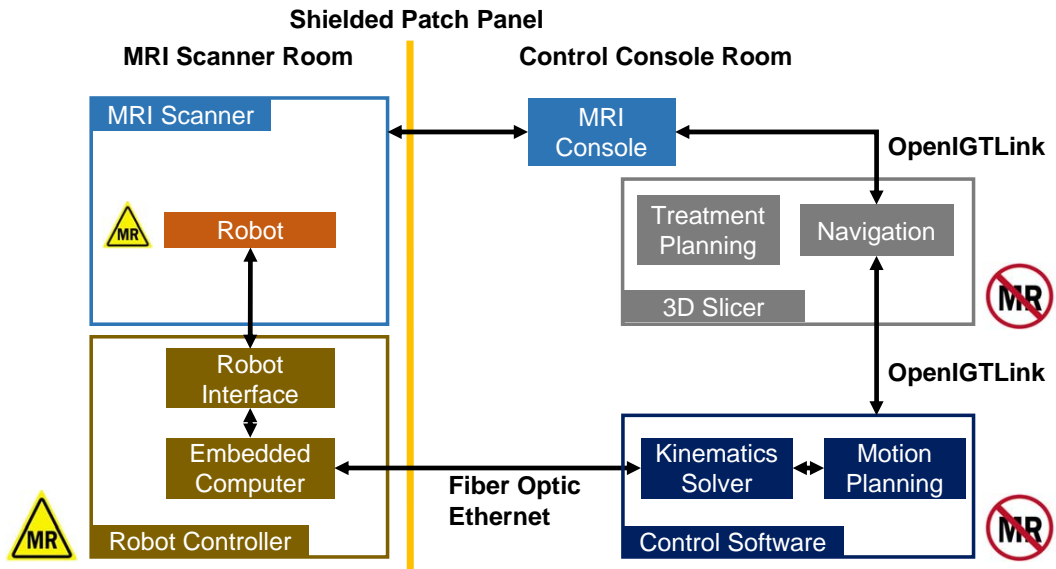
Figure 2.3: System architecture of robotic system for MRI-guided precision DBS electrode placement.
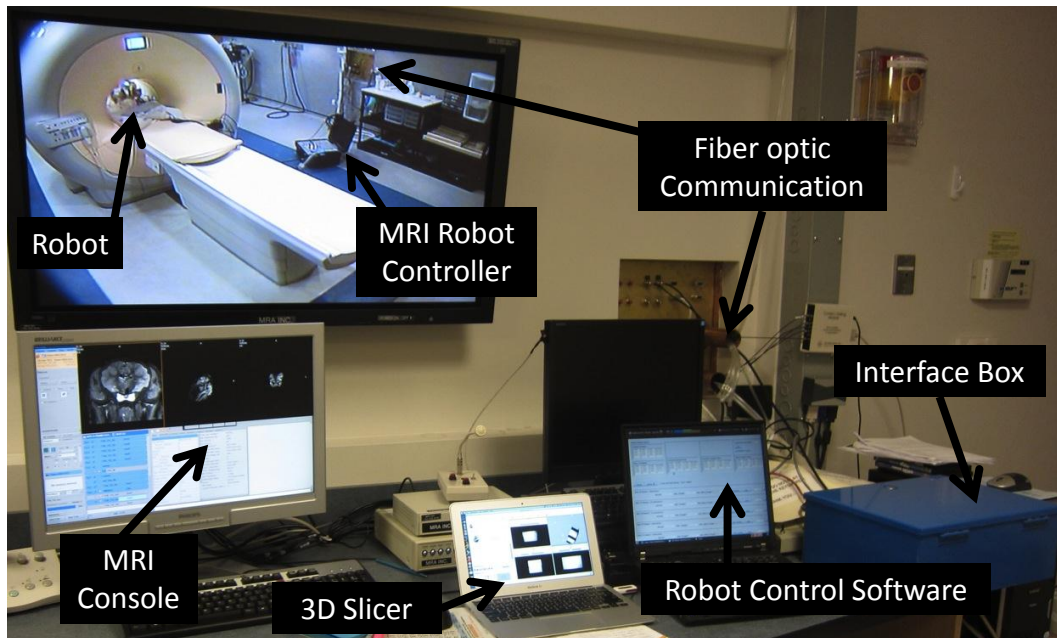
Figure 2.4: Configuration of the MRI-guided robotic neurosurgery system. The stereotactic manipulator is placed within the scanner bore and the MRI robot controller resides inside the scanner room. The robot controller communicates with the control computer within the Interface Box through a fiber optic link. The robot control software running on the control computer communicates with navigation software through OpenIGTLink.

2.2.2 Clinical Workflow

The current typical workflow for DBS stereotactic neurosurgery involves numerous steps. The following list describes the major steps as illustrated in Fig. 2.5 (a):

1. Acquire MR images prior to day of surgery;

2. Perform preoperative surgical planning;

3. Surgically attach fiducial frame;

4. Interrupt procedure to acquire CT images;

5. Fuse preoperative MRI-based plan to preoperative CT;

6. Use stereotactic frame to align the cannula guide and place the cannula.

7. Optionally confirm placement with non-visual approach such as microelectrode recording (MER, a method that uses electrical signals in the brain to localize the surgical site) and/or visual approach such as fluoroscopy which can localize the instrument but not the target anatomy.
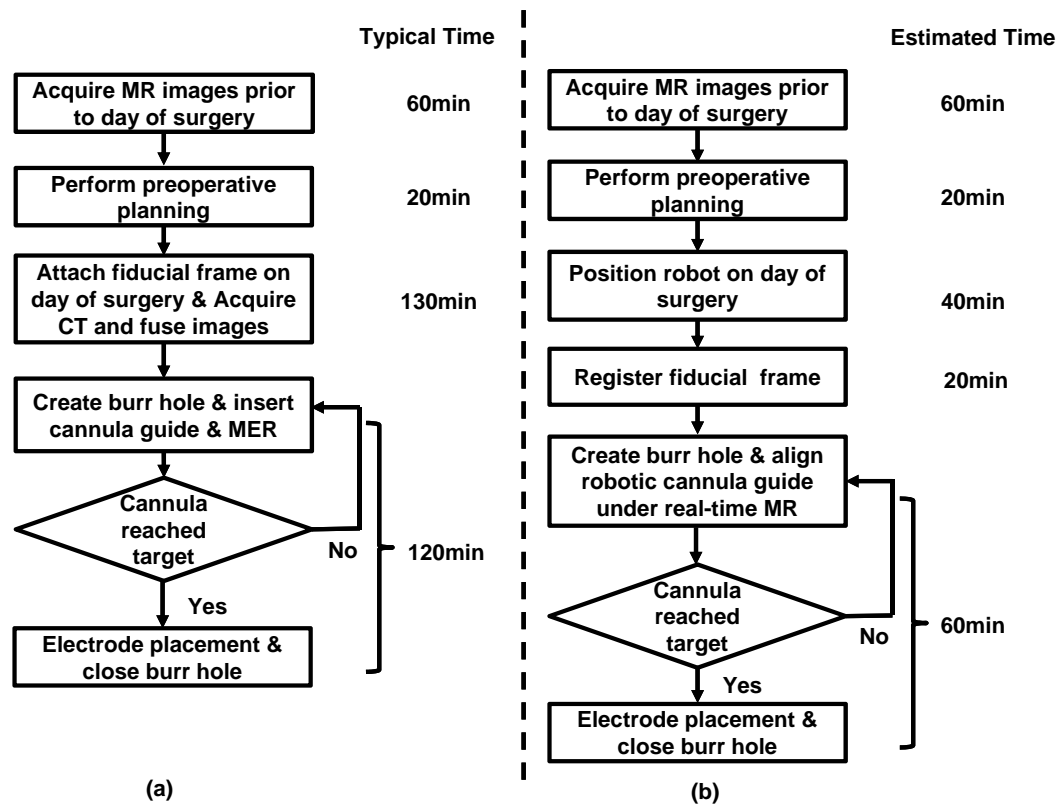
Figure 2.5: Workflow comparison of manual frame-based approach and MRI-guided robotic approach for unilateral DBS lead placement. (a) Workflow of a typical lead placement with measured average time per step. (b) Workflow of an MRI-guided robotic lead placement with estimated time per step.

During the workflow, there are many points where errors could be introduced, these errors are categorized as three main subtypes : 1) those associated with planning, 2) with the frame, and 3) with execution of the procedure. Our approach, especially the new workflow, as shown in Fig. 2.5 (b), addresses all these three errors. First, error due to discrepancies between the preoperative plan and the actual anatomy (because of brain shift) may be attenuated through the use of intraoperative MR imaging. Second, closed-loop controlled robotic needle alignment eliminates the mental registration between image and actual anatomy, while providing precise motion control in contrast to the inaccurate manual frame alignment. Third, errors that arise with execution would be compensated with intraoperative interactively updated MR image feedback. To sum up, by attenuating all three error sources, these advantages enabled by the robotic system could potentially improve interventional accuracy and outcomes.

The procedure duration is potentially reduced significantly from two aspects: 1) avoiding a CT imaging session and corresponding image fusion and registration, and 2) using direct image guidance instead of requiring additional steps using MER. As shown in Fig. 2.5 (b) : 1) The proposed approach completely removes the additional perioperative CT imaging session potentially saving about one hour of procedure time and the complex logistics of breaking up the surgical procedure for CT imaging. 2) During the electrode placement, the current guidance and confirmation method relies on microelectrode recording, a one-dimensional signal to indirectly localize the target.

MER localization takes about 40 minutes in an optimal scenario, and could take one hour more if not in an optimal scenario. In contrast to the indirect, iterative approach with MER, the proposed system utilizes MR imaging to directly visualize placement. Eliminating the need for MER may reduce about one hour of procedure time per electrode, and in the typical DBS procedure with bilateral insertion this would result in a benefit of two hours. Therefore, for a bilateral insertion the benefit in reduced intraoperative time could potentially be as great as three hours, on top of the benefits of improved planning and accurate execution of that plan.

2.2.3   Mechanism Design

2.2.3.1   Design Requirements

As discussed in Section 1.1.3, the robot should meet the requirements of classification for MR safe or MR conditional. The interference of a robotic system with the MR scanner is attributed to its mechanical (primarily material) and electrical properties. From materials perspective, ferromagnetic materials must be avoided entirely, though non-ferrous metals such as aluminum, brass, nitinol and titanium, or composite materials can be used with caution. In this robot, all electrical and metallic components are isolated from the patient's body. Non-conductive materials are utilized to build the majority of the components of the mechanism, i.e. base structure are made of 3D printed plastic materials and linkages are made out of high strength, bio-compatible

plastics including Ultem and PEEK.

From electrical perspective, conductors passing through the patch panel or wave guide could act as antennas, introducing stray RF noise into scanner room and thus resulting in image quality degradation. For this reason, the robot controller is designed to be placed inside scanner room and communicate with a computer in the console room through fiber optic medium.

Non-magnetic piezoelectric actuators are used to drive the mechanism. There are two primary types of piezoelectric motors, harmonic and non-harmonic. Harmonic motors, such as Nanomotion motors (Nanomotion Ltd., Israel) and Shinsei motors (Shinsei Corporation, Japan), are generally driven with fixed frequency sinusoidal signal. Non-harmonic motors, such as PiezoLegs motors (PiezoMotor AB, Sweden), require a complex shaped waveform on four channels generated with high precision at fixed amplitude. In this study, PiezoLegs motors have been selected. PiezoLegs motor has the required torque (50 mNm) with with small footprint ($\oslash$ 23 $\times$ 34 mm). Shinsei motors can provide more torque 0.1 Nm but with relative big footprint ($\oslash$ 67 $\times$ 45 mm).

Optical encoders (US Digital, Vancouver, WA) EM1-0-500-I linear (0.0127 mm/count) and EM1-1-1250-I rotary (0.072°/count) encoder modules are used. The encoders are placed on the joint actuators and reside in the scanner bore, to provide position feedback for each joint. Differential signal drivers sit on the encoder module, and the signals are transmitted via shielded twisted pairs cables to the controller.

The encoders have been incorporated into the robotic device and perform without any evidence of stray or missed counts.

From the perspective of kinematic structure, the interventonal procedure is characterized by relatively large angluar mobility about a single point within a limited spatial volume. There are two basic design approaches, as summrized in a compresive review paper on medical robotics [47]. One approach utilizes a passive wrist to allow the surgical tools to pivot about the insertion point, such as the mechanism implemented in the commercial robotic systems Aesop [48] and Zeus [49]. The other approach employs a mechanically constrained remote center of motion (RCM), which naturally decouples rotations and translations of instruments at a point some distance from the mechanical structure of the robot. The RCM approach has been used by daVinci robot [50] and many other medical robotic research platforms [51,52], due to its three major advantages: 1) it decouples the translational motion from the pivoting motion, 2) it allows actuators and transmission mechanism to be installed away from the entry point, and therefore enables relative large orientation for the tools with a compact mechanism, 3) simplifies the system control and safety checking, as summarized in [53]. Hence, the RCM mechanism is employed as a central design feature in this study. Please note that the RCM point in this design is at the target point, which is different than some systems like the daVinci robot which is at the entry point.

The robotic manipulator is designed to be kinematically equivalent to the commonly used Leksell stereotactic frame, and configured to place an electrode within a

confined standard 3 Tesla Philips Achieva scanner bore with 60 cm diameter. The manual frame's #1, #2 and #3 axes set the target position, and #4 and #5 align the orientation of the electrode as shown in Fig. 2.6 (left). The Iterative design process is conducted involving several iterations of prototyping and testing. A preliminary design for the robotic manipulator based upon these requirements is implemented through a parrallelogram linkage and cable driven yoke as described in our early work [54] where neither the actuator, motion transmission nor the encoder design was covered. The current work presents the first fully-developed functional prototype of this robot that has 5-axis motorized and encoded motion.
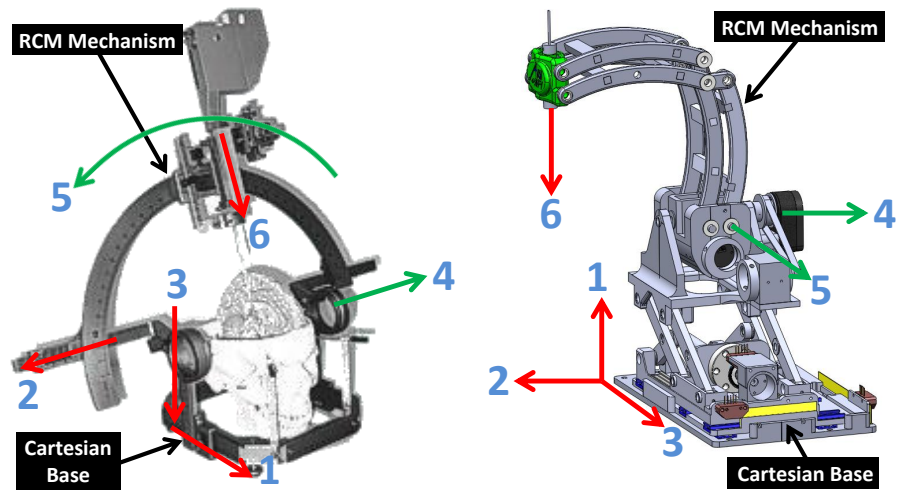
Figure 2.6: Equivalence of the degrees of freedom of a traditional manual stereotactic frame (left) and the proposed robotic system (right). Translation DOF in red, rotational DOF in green.

To mimic the functionality and kinematic structure of the manual stereotactic frame, a combination of a 3-DOF prismatic Cartesian motion base module and a 2-DOF remote center of motion (RCM) mechanism module are employed, as shown in

Fig. 2.6 (right). The robot provides three prismatic motions for Cartesian positioning ($DOF\#1 - DOF\#3$), two rotary motions corresponding to the arc angles ($DOF\#4$ and $DOF\#5$), and a manual cannula guide ($DOF\#6$). To achieve high stiffness of the robot in spite of the plastic material structure, three approaches have been implemented. 1) Parallel mechanism is used for the RCM linkage and Scott-Russell vertical motion linkages to take advantage of the enhanced stiffness due to the closed-chain structure; 2) High strength plastic Ultem (flexural modulus 1,300,000 pounds per square inch (PSI)) is machined to construct the RCM linkage. The Cartesian motion module base is primarily made of 3D printed ABS plastic (flexural modulus 304,000 PSI); 3) Non-ferrous aluminum linear rails constitutes mechanical backbone to maintain good structural rigidity.

Table 2.1: Joint Space Kinematic Specifications of The Robot

Axis	Motion	Robot
1	x	± 35mm
2	y	± 35mm
3	z	± 35mm
4	Sagittal plane angle	0-90°
5	Transverse plane angle	±45°
6	Needle insertion	0-75mm

2.2.3.2   Orientation Motion Module

As portrayed in Fig. 2.7, the manipulator allows $0° - 90°$ rotation motion in the sagittal plane. The neutral posture is defined when the cannula/electrode (1) inside

the headstock (2) is in vertical position. In the transverse plane, the required range of motion is ±45° about the vertical axis as specified in Table 2.1. A mechanically constrained RCM mechanism, in the form of a parallelogram linkage (3) was designed. In order to reduce backlash, rotary actuation of RCM DOF are achieved via Kevlar reinforced timing belt transmissions (7), which are loaded via eccentric locking collars (11), eliminating the need for additional tension pulleys. The primary construction materials for this mechanism is polyetherimide (Ultem), due to its high strength, machinability, and suitability for chemical sterilization. This module mimics the arc angles of the tractional manual frame.
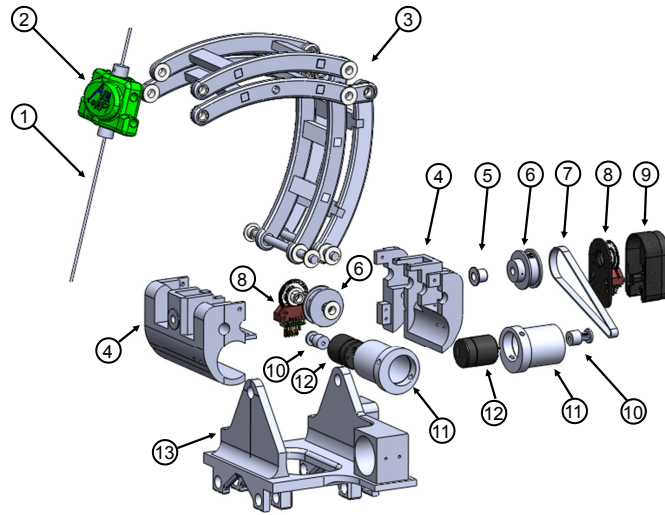
Figure 2.7: Exploded view of the RCM orientation module, showing (1) instrument/electrode, (2) headstock with cannula guide, (3) parallel linkage mechanism, (4) manipulator base frame, (5) flange bearings, (6) pulleys, (7) timing belts, (8) rotary encoders, (9) encoder housings, (10) pulleys, (11) eccentric locking collars, (12) rotary piezoelectric motors, (13) manipulator base.

2.2.3.3   Cartesian Motion Module

As shown in Fig. 2.8, linear travel through DOF #2 and #3 is achieved via direct drive where a linear piezoelectric motor (PiezoLegs LL1011C, PiezoMotor AB, Sweden), providing 6 N holding force and 1.5 cm/s speed, controls each decoupled 1-DOF motion. DOF #1 is actuated via scissor lift mechanism (known as Scott-Russell mechanism) driven by a rotary actuator (PiezoLegs, LR80, PiezoMotor AB, Sweden) and an aluminum anodized lead screw (2 mm pitch). This mechanism is compact and attenuates structural flexibility due to plastic linkages and bearings.
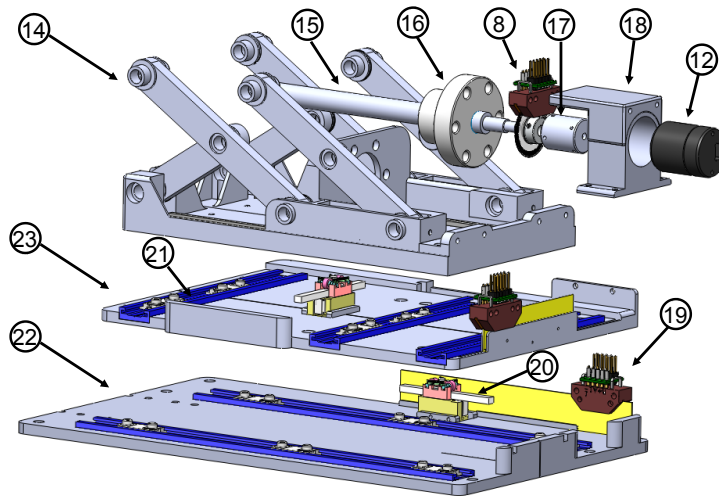
Figure 2.8: Exploded view of the Cartesian motion module, showing (14) Scott-Russell scissor mechanism, (15) lead-screw, (16) nut, (17) motor coupler, (18) motor housing, (19) linear encoder, (20) linear piezoelectric motor, (21) linear guide, (22) horizontal motion stage, (23) lateral motion stage.

2.2.3.4 Workspace Analysis

The range of motion of the robot was designed to cover the clinically required set of targets and approach trajectories (STN, GPi and VIM of the brain). As illustrated in Table 2.1, the range of motion for placement of the robot's center of rotation is ± 35 mm, ± 35 mm and ± 35 mm in x, y and z axes respectively. With respect to this neutral posture, the robot has $0° - 90°$ rotation motion in the sagittal plane and $\pm 45°$ in the transverse plane. For an electrode with 75 mm insertion depth, the reachable workspace of the robot for target locations is illustrated in Fig. 2.9 with respect to a representative skull model based on the head and face anthropometry of adult U.S. civilians [55]. The 95% percentile male head breath, length, and stomion to top of head measurements are 16.1, 20.9 and 19.9 cm respectively. This first prototype of the robot is able to cover the majority of brain tissue inside the skull. Basal ganglia area is the typical DBS treatment target, which is approximated as a ellipsoid in Fig. 2.9. Although the workspace is slightly smaller than the skull, all typical targets and trajectories for the intended application of DBS procedures are reachable. The current robot workspace is also smaller than the Leksell frame since the later is a generic neurosurgery mechanism, while this robot is primarily tailored for DBS which has a much smaller workspace requirement.
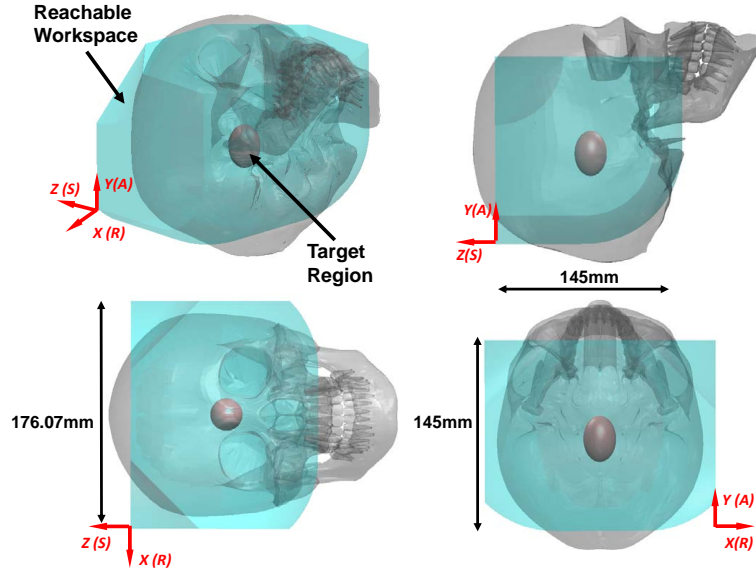
Figure 2.9: Reachable workspace of the stereotactic neurosurgery robot overlaid on a representative human skull. The red ellipsoid represents the typical DBS treatment target, i.e. the basal ganglia area.

2.2.4 Motion Control System

A key reason that commercially available piezoelectric motor drivers affect image quality is due to the high frequency switching signal. While a low-pass filter may provide benefit, it has not been effective in eliminating the interference and often significantly degrades motor performance. To address this issue, a custom MR conditional motor controller is developed as a team effort by the lab [56]. The controller utilizes linear regulators and direct digital synthesizers (DDS) to produce the driving signal in combination with analog π filters. The control system comprises of four primary units as illustrated in Fig. 2.10: 1) the power electronics unit, 2) the piezoelectric driver, which unit directly interfaces with the piezoelectric motors, 3) backplane controller unit, an embedded computer which translates high level motion

information into device level commands, and 4) an interface box containing the fiber optic Ethernet communication hardware. The power electronics unit, piezoelectric drive unit and backplane controller unit are enclosed in an an electro-magnetic interference (EMI) shielded enclosure. A user workstation, connected to the interface box in the console room, which operates the navigation software 3D Slicer is the direct interface for the physician.

The robot controller contains piezoelectric motor driver modules plugged into a backplane. The corresponding power electronics consists of cascaded regulators. The primary regulator (F48-6-A+, SL Power Electronics, USA) converting from the isolated, grounded 120 V AC supply in the MR scanner room to 48 V DC is a linear regulator chosen for its low noise. Two switching regulators modified to operate at ultra low frequencies with reduced noise generate the 5 V DC and 12 V DC (QS-4805CBAN, OSKJ, USA) power rails that drive the logic and analog preamplifiers of the control system, respectively. The 48 V DC from the linear regulator directly feeds the linear power amplifiers for the motor drive signals (through a safety circuit).

An innovation of the custom-developed motor driver is to use linear power amplifiers for each of the four drive channels of the piezoelectric motors and a field-programmable gate array (FPGA, Cyclone EP2C8Q208C8, Altera Corp., USA)-based direct digital synthesizer (DDS) as a waveform generator to fundamentally avoid these high frequency signals. As shown in Fig. 2.11, each motor control card module of the piezoelectric driver unit, consists of four DDS waveform generators. These generators
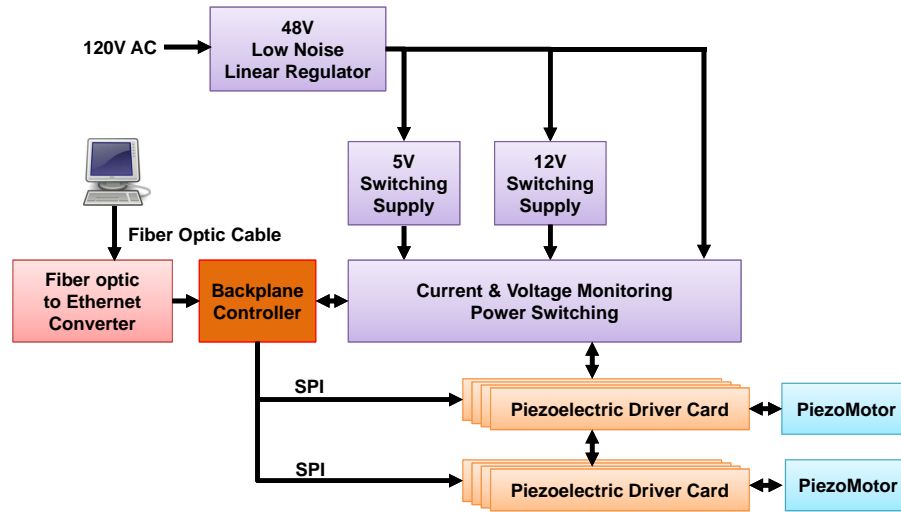
Figure 2.10: Block diagram of the MRI robot control system. The power electronics and piezoelectric actuator drivers are contained in a shielded enclosure and connected to an interface unit in the console room through a fiber optic Ethernet connection.

output to two dual-channel high speed (125 million samples per second) digital-to-analog converters (DAC2904, Texas Instruments, USA) and then connect to four 48 V linear power amplifiers (OPA549, Texas Instruments, USA). The motor control card also has two Low-Voltage Differential Signaling (LVDS) receivers that connect to two quadrature encoders (one of which may be replaced with differential home and limit sensors). The motor control card has a microcontroller (PIC32MX460F512L, Microchip Tech., USA) that loads a predefined waveform image from a Secure Digital (SD) card into the FPGA's DDS and then operates a feedback loop using the encoder output. The motor control cards are interconnected via Serial Peripheral Interface (SPI) bus to one backplane controller which communicates over fiber optic 100-FX Ethernet to the interface box in the room where a control PC running the user interface is connected.
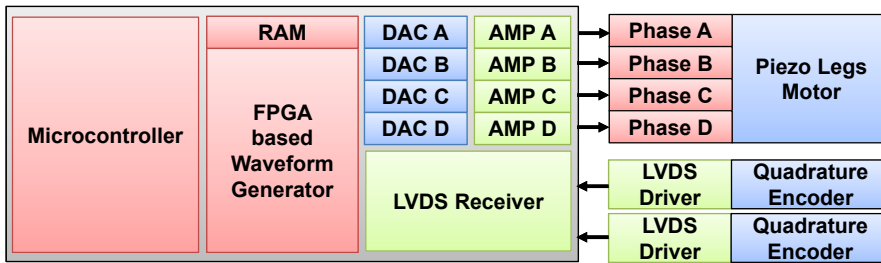
Figure 2.11: Block diagram showing the key components of a piezoelectric motor driver card-based module.

2.2.5 Robot Registration and Control Software

Open source navigation software 3D Slicer is used for surgical planning and navigation [45]. The desired target is visualized and defined in 3D slicer, as shown in Fig. 2.12, and then sent to robot control software over a network via OpenIGTLink communication protocol.
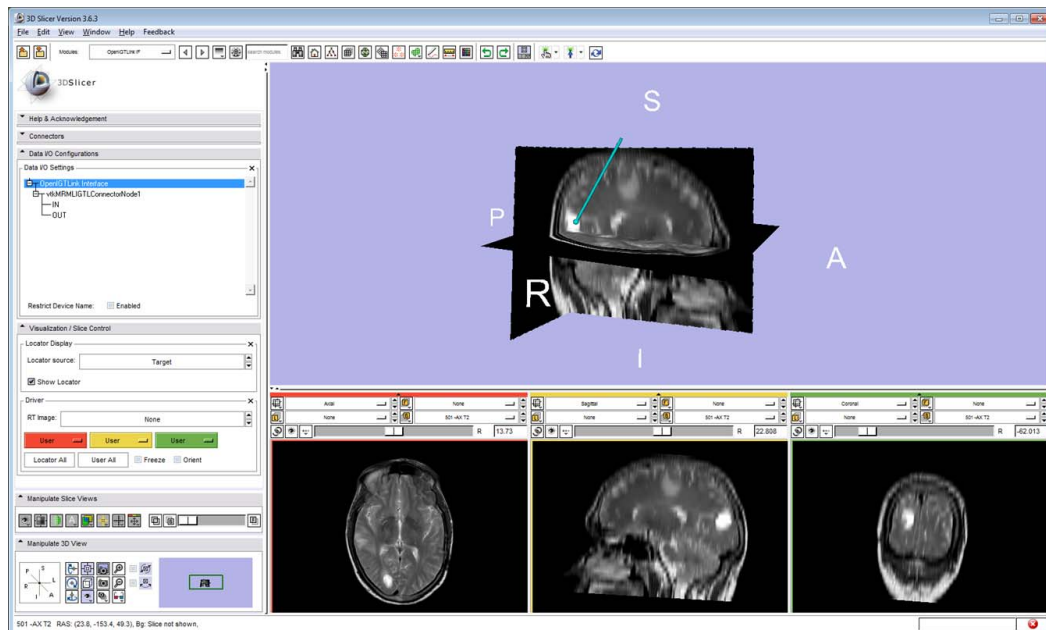
Figure 2.12: 3D Slicer navigation software showing a virtual locater pointing to the selected target on an MR brain image.

A fiducial-based registration is used to localize the base of the robot in the MRI

scanner. To register the robot to the image space, the serial chain of homogeneous transformations is used, as shown in Fig. 2.13.

$$T_{Tip}^{RAS} = T_Z^{RAS} \cdot T_{Base}^Z \cdot T_{Rob}^{Base} \cdot T_{Tip}^{Rob} \tag{2.1}$$

where T_{Tip}^{RAS} is the needle tip in the RAS (Right, Anterior, Superior) patient coordinate system, T_Z^{RAS} is the Z-shaped fiducial's coordinate in RAS coordinates, as shown in Fig. 2.14, which is localized in 6-DOF from MR images via a Z-frame fiducial marker based on multi-image registration method as described in more detail in our previous study [57]. The fiducial is rigidly fixed to the base and positioned near the scanner isocenter; once the robotic system is registered, this device is removed. Since the robot base is fixed in scanner coordinates, this registration is only necessary once. T_{Base}^Z is a fixed calibration of the robot base with respect to the fiducial frame, T_{Rob}^{Base} is the constant offset between robot origin and a frame defined on the robot base, and T_{Tip}^{Rob} is the needle tip position with respect to the robot origin, which is obtained via the robot kinematics.

2.2.6 Experiments and Results

Two primary sets of experiments were run to assess imaging compatibility with the MRI environment and positioning accuracy of the system. The effect of the robot on image quality was assessed through quantitative SNR analysis, quantitative geometric
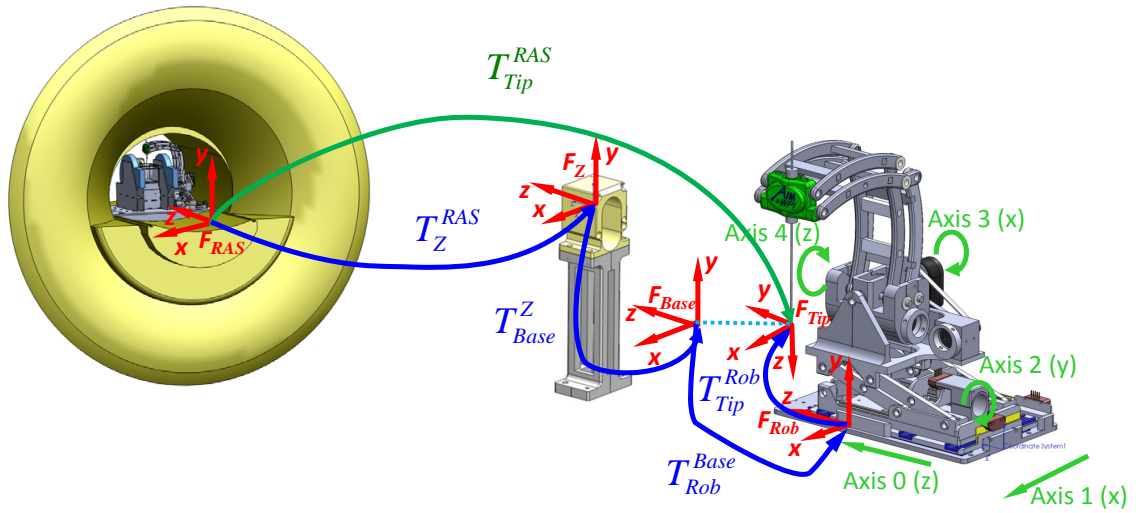
Figure 2.13: Coordinate frames of the robotic system for registration of robot to MR image space.

distortion analysis and qualitative human brain imaging. Targeting accuracy of this system was assessed in free space tested using an optical tracking system (OTS), and image-guided targeting accuracy was assessed in a Philips Achieva 3 Tesla scanner.

2.2.6.1 Quantitative and Qualitative Evaluation of Robot-Induced Image Interference

To understand the impact of the robotic system to the imaging quality, SNR analysis based on the National Electrical Manufacturers Association (NEMA) standard (MS1-2008) is utilized as a metric to quantify noise induced by the robot. Furthermore, even with sufficiently high SNR, geometric distortion might exist due to factors including eddy current and magnetic susceptibility effects. Geometric distortion of
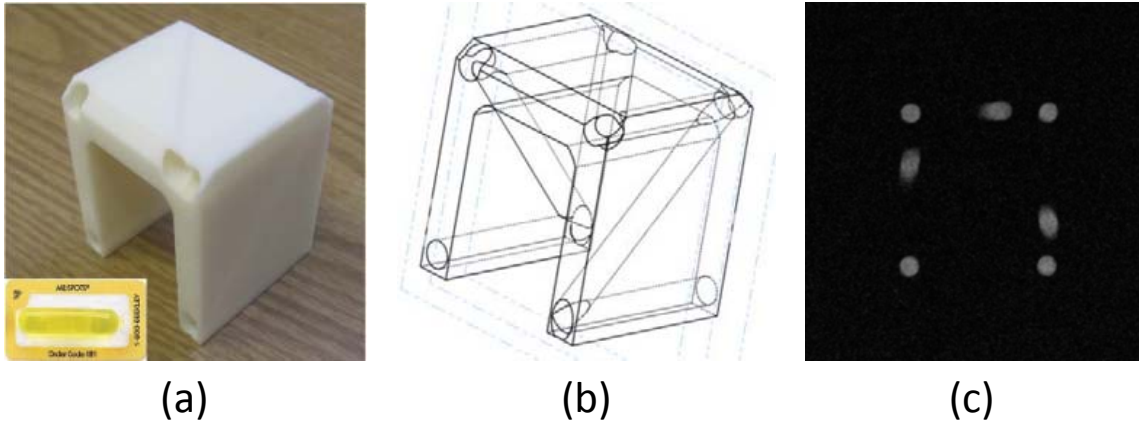
Figure 2.14: (a) The Z-shaped fiducial frame. Inset: MR visible fiducial marker tube, (b) CAD model showing the Z-shape in 3 orthogonal planes, (c) Cross-sectional MR image of the fiducial frame.

the image is characterized based on the NEMA standard (MS2-2008). The analysis utilized a Periodic Image Quality Test (PIQT) phantom (Philips, Netherlands) that has complex geometric features, including cylindrical cross section, arch and pin section, as shown in Fig. 2.15. To mimic the actual scenario of the robot and control position, the robot is placed 5 mm away from the phantom. The controller was placed approximately 2 meters away from the scanner bore inside the scanner room (in a configuration similar to that shown in Fig. 2). In addition to the quantitative analysis, a further experiment qualitatively compared the image quality of a human brain under imaging with the robot in various configurations.

A. Signal-to-Noise Ratio Based Compatibility Analysis

To thoroughly evaluate the noise level, three clinically applied imaging protocols were assessed with parameters listed in Table 2.2. The protocols include 1) diagnostic imaging T1-weighted fast field echo (T1W-FFE), 2) diagnostic imaging T2-weighted
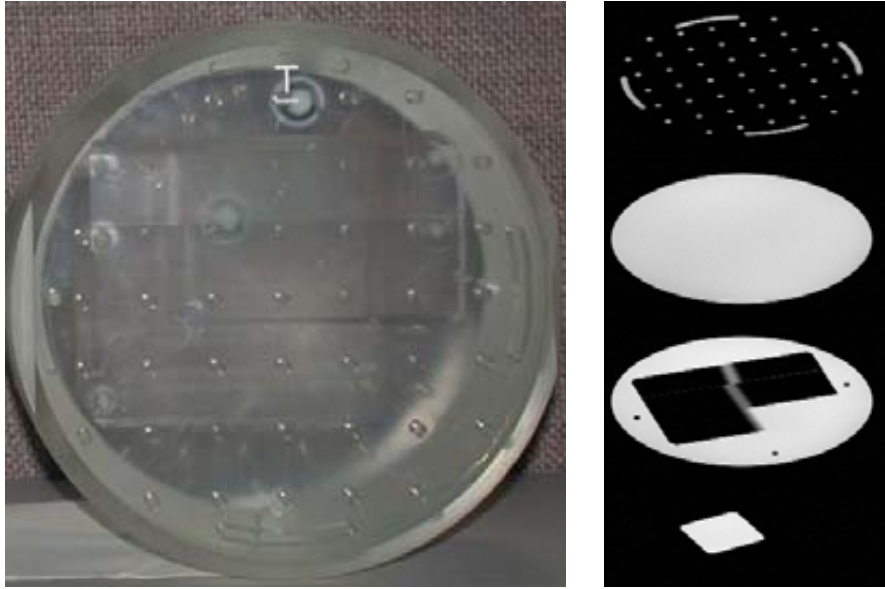
Figure 2.15: PIQT phantom and corresponding cross-sectional MR image showing complex geometric features.

turbo spin echo for needle/electrode confirmation (T2W-TSE), and 3) a typical T2-weighted brain imaging sequence (T2W-TSE-Neuro). All sequences were acquired with field of view (FOV) 256 mm×256 mm, 512×512 image matrix and 0.5 mm×0.5 mm pixel size. The first two protocols were used for quantitative evaluation, while the third was used for qualitative evaluation with a human brain.

Table 2.2: Scan Parameters for Compatibility Evaluation

Protocol	TE (ms)	TR (ms)	FA (deg)	Slice (mm)	Bandwidth (Hz/pixel)
T1W-FFE	2.3	225	75	2	1314
T2W-TSE	115	3030	90	3	271
T2W-TSE-Neuro	104	4800	90	3	184

Five configurations of the robot were assessed to identify the root cause of image quality degradation: baseline with phantom only inside scanner, robot present but

unpowered, robot powered, robot running during imaging, and then a repeated base-line with phantom only, as shown in Fig. 2.16. Fig. 2.17 illustrates the representative images of SNR test with T1W-FFE and T2W-TSE images in the first four configu-rations. For the quantitative analysis, SNR is calculated as the mean signal in the center of the phantom divided by the noise outside the phantom. Mean signal is de-fined as the mean pixel intensity in the region of interest. The noise is defined as the average mean signal intensity in the four corners divided by 1.25 [58]. Fig. 2.18 shows the boxplot of the SNR for five robot configurations under these two scan protocols.
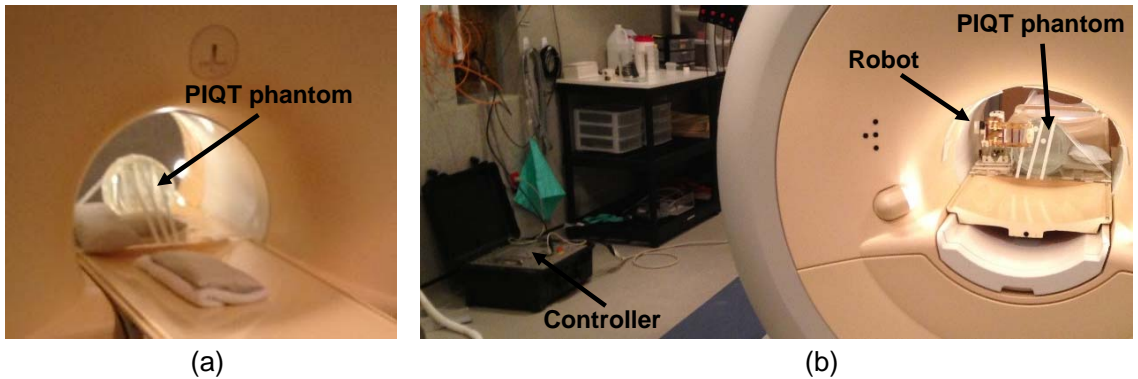
Figure 2.16: Robot configurations for SNR analysis showing: (a) baseline with phan-tom only, (b) Robot and controller placed inside scanner closed to phantom.

The results from this plot are indicative of three primary potential sources of im-age artifact, namely *materials of the robot* (difference between baseline and robot present but unpowered), *power system and wiring* (difference between robot present but unpowered and robot powered), and *drive electronics* (difference between robot powered and robot running). The repeated baseline indicates the imaging quality shift caused by the scanner system itself. The mean SNR reduction from baseline for
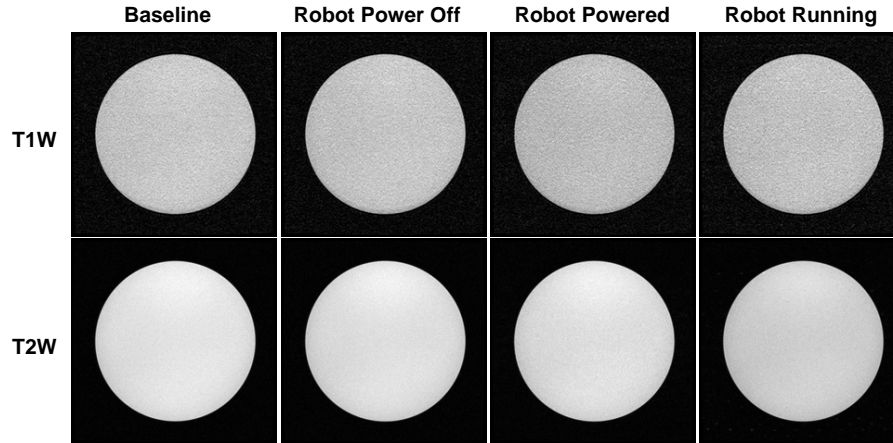
Figure 2.17: MRI of the homogeneous section of the phantom in four configurations with two imaging protocols demonstrating visually unobservable image artifacts.

these three differences are 2.78%, 6.30%, and 13.64% for T1W-FFE and 2.56%, 8.02% and 12.54% for T2W-TSE, respectively. Note that Fig. 2.17 shows this corresponding to visually unobservable image artifacts.

Elhawary et al. [59] demonstrated that SNR reduction for the same PiezoLegs motor (non-harmonic motor) using a commercially available driver is 26% with visually observable artifact. In terms of harmonic piezoelectric motors, Krieger et al. [60] showed that the mean SNR of baseline and robot motion using NanoMotion motors under T1W imaging reduced approximately from 250 to 50 (80%) with striking artifact. Though the focus of this work is on the use of non-harmonic PiezoLegs motors for this application, we also demonstrated the control system capable of generating less than 15% SNR reduction for NanoMotion motors in our previous work [61]. Our system shows significant improvement with PiezoLegs motor over commercially available motor drivers when the robot is in motion. Even though there is no specific

standard about SNR and image usability, the visually unobservable image artifact in our system is a key differentiator with that of [59] which used the same motors but still showed significant visual artifact.
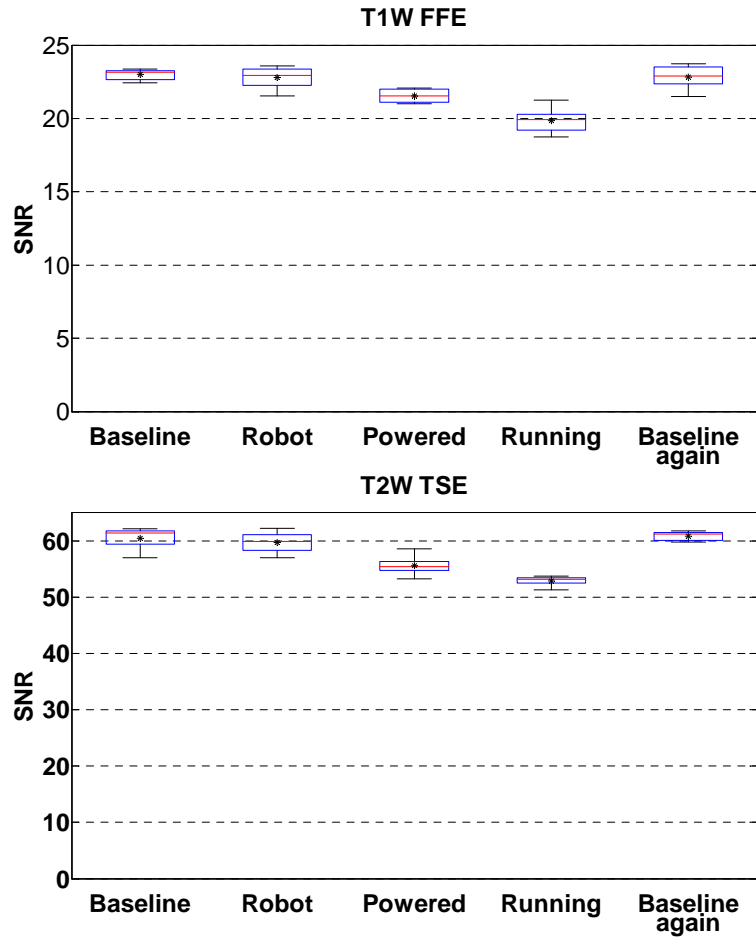
Figure 2.18: Boxplots showing the range of SNR values for each of five robot configurations evaluated in two clinically appropriate neuro imaging protocols (T1W FFE & T2W TSE). The configurations include Baseline (no robotic system components present in room), Robot (robot presented but not powered), Powered (Robot connected to power on controller), Running (Robot moving during imaging), and a repeated baseline with no robotic system components present.

B. Geometric Distortion Based Compatibility Analysis

The NEMA standard (MS2-2008) defines 2D geometric distortion as the maximum percent difference between measured distances in an image and the actual corre-

sponding phantom dimensions. Eight pairs of radial measurements (i.e. between points spanning the center of the phantom), are used to characterize the geometric distortion as shown in Fig. 2.19 for T1W-FFE and T2W-TSE protocols.
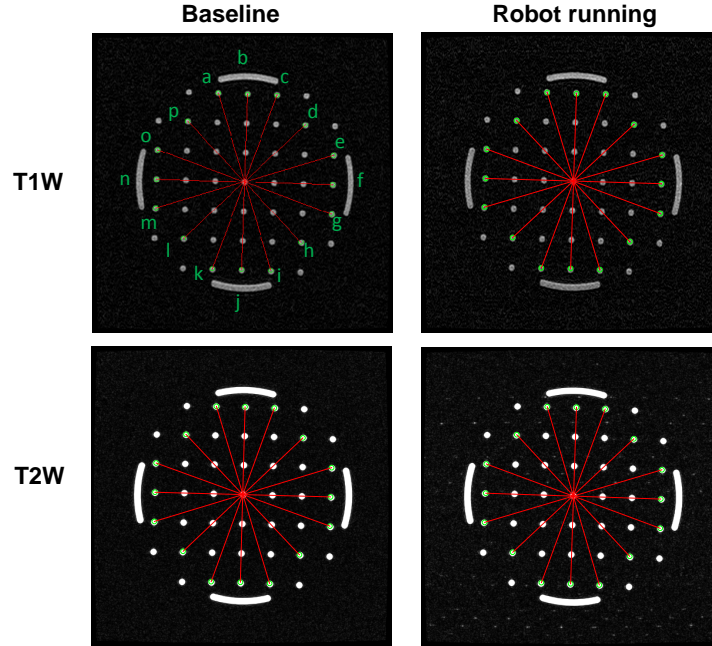
Figure 2.19: Geometric patterns of the non-homogeneous section of the phantom filled with pins and arches for the two extreme robot configurations and the same two imaging protocols. The overlaid red line segments indicates the measured distance for geometric distortion evaluation.

With the known geometry of the pins inside the phantom, the actual pin distance is readily available. The distance is measured on the image, and then are compared to the actual corresponding distances in the phantom as shown in Table. 2.3 for T1W-FFE protocol. The maximum difference between baseline image acquired with no robot and actual distance is less than 0.31% as shown in the third column of the table. The measured maximum distortion percentage for images acquired while the robot was running was 0.20%. This analysis demonstrates negligible geometric

distortion of the acquired images due to the robot running during imaging.

Table 2.3: Geometric Distortion Evaluations Under Scan Protocol T1W.

Line segment	Actual distance (mm)	Measured distance (difference %)	
		Baseline	Robot running
ai	158.11	158.46(0.22)	158.39(0.17)
bj	150.00	150.46(0.31)	150.24(0.16)
ck	158.11	158.48(0.23)	158.03(0.05)
dl	141.42	141.51(0.07)	141.14(0.20)
em	158.11	157.97(0.09)	157.85(0.17)
fn	150.00	149.92(0.05)	149.89(0.07)
go	158.11	158.16(0.03)	158.24(0.08)
hp	141.42	141.65(0.16)	141.65(0.16)

C. Qualitative Imaging Evaluation

In light of the quantitative SNR results of the robot system, the image quality is further evaluated qualitatively by comparing brain images acquired with three different configurations under the previously defined T2W imaging sequence. Fig. 2.20 shows the experimental configuration and the corresponding brain images of a volunteer placed inside scanner bore with the robot. There is no visible loss of image quality (noise, artifacts, or distortion) in the brain images when controller and robot manipulator are running.

The capability to use the scanner's real-time continuous imaging capabilities in conjunction with the robot to monitor needle insertion was further demonstrated. In one example qualitatively demonstrating this capability, a 21 Gauge Nitinol needle was inserted into a gelatin phantom under continuous updated images (700ms per frame). The scan parameters including the repetition rate can be adapted as required for the particular application to balance speed, field of view, and image quality. As

shown in Fig. 2.21, the needle is clearly visible and readily identifiable in the MR images acquired during needle insertion, and these images are available in real-time for visualization and control. The small blobs observed near the needle tip in these images are most likely due to the shape of the needle tip geometry.
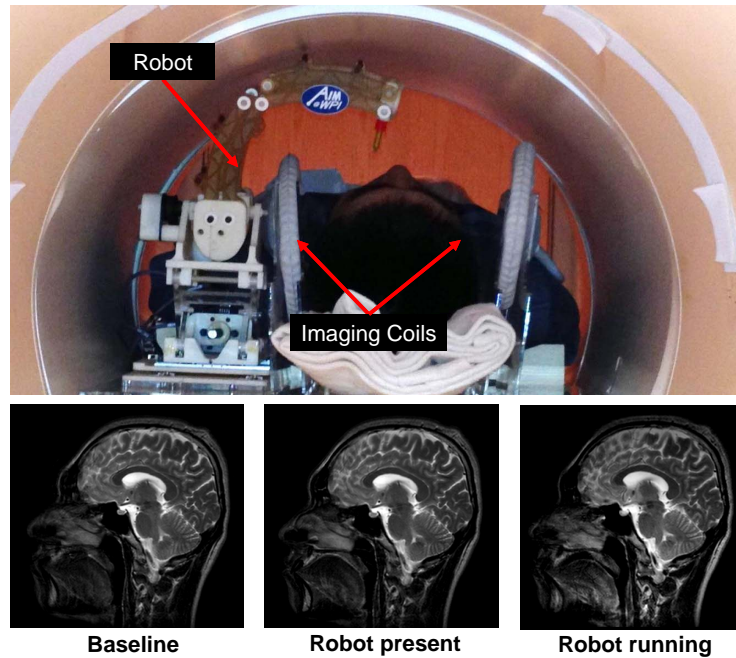
Figure 2.20: Qualitative analysis of image quality. Top: Patient is placed inside scanner bore with supine position and robot resides on the side of patient head. Bottom: T2 weighted sagittal images of brain taken with three configurations: no robot in the scanner (bottom-left), controller is powered but motor is not running (bottom-middle) and robot is running (bottom-right).

2.2.6.2 Robotic System Accuracy Evaluation

Assessing system accuracy was undertaken in two main phases: 1) benchtop free-space system accuracy and 2) MR image-guided system accuracy. Free-space accuracy experiment utilized an optical tracking system to calibrate and verify accuracy, while
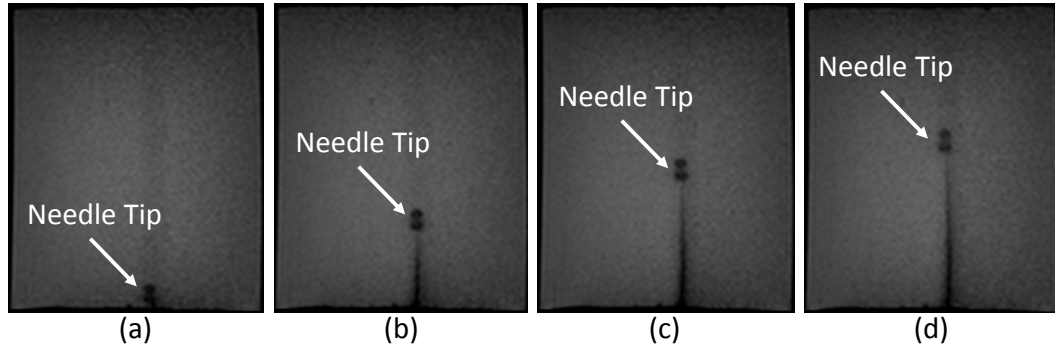
Figure 2.21: Example of real-time MR imaging capabilities at 1.4Hz during needle insertion. Shown at (a) Initial position, (b) 25mm depth, (c) 45mm depth, and (d) 55mm insertion depth into a phantom.

image-guided analysis utilized MR images. Three metrics are utilized for analyzing system error as summarized in Table 2.4 from both experiments, i.e. tip position, insertion angle and distance from RCM intersection point to needle axes. Tip position error is a measure of the distance between a selected target and the actual location of the tip of the inserted cannula. Insertion angle error is measured as an angular error between the desired insertion angle and the actual insertion angle. Distance from RCM intersection point to needle axes represents an analysis of the mechanism's performance as an RCM device. For these measurements a single RCM point is targeted from multiple angles, and the minimum average distance from a single point of all the insertion axes is determined via least squares analysis. The actual tip positions, as determined via the OTS system during the benchtop experiment and image analysis for the MRI guided experiments, are registered to desired targets with point cloud based registration to isolate the robot accuracy from registration-related errors in the experiments.

A. Robot Accuracy Evaluation with Optical Tracking System

A Polaris optical tracking system (Northern Digital Inc, Canada) is utilized, with a passive 6-DOF tracking frame attached to the robot base, and an active tracking tool mounted on the end-effector.

The experiment is a two step procedure, consisting of robot RCM mechanism calibration and robot end-effector positioning evaluation. The first procedure was performed by moving the mechanism through multiple orientations while keeping the Cartesian base fixed, and performing a pivot calibration to determine tool tip offset (RMS error of this indicates RCM accuracy). After successfully calibrating the RCM linkage, the robot is moved to six targets locations, with each target consisting of five different orientations. Three groups of data were recorded: desired needle tip transformation, reported needle transformation as calculated with kinematics based on optical encoders readings, and measured needle transformation from OTS. Analysis of experimental data indicates that the tip position error (1.09 ± 0.28 mm), orientation error ($2.06 \pm 0.76°$), and the error from RCM intersection point to needle axes (0.33 ± 0.05 mm) as can be seen in Table 2.4.

B. Robot Accuracy Evaluation under MR Image-Guidance

The experimental setup utilized to assess system level accuracy within the scanner is shown in Fig. 2.22. An 18-gauge ceramic needle (to limit paramagnetic artifacts) was inserted into a gelatin phantom and imaged with a high resolution $0.5mm^3$, T2-weighted turbo spin echo imaging protocol (T2W-TSE) to assess robot instrument

tip position. This experiment reflects the effectiveness with which the robotic system can target an object identified within MR images. The experimental procedure is as follows:

1. Initialize robot and image Z-frame localization fiducial;

2. Register robot base position with respect to RAS patient coordinates;

3. Remove fiducial frame and home robot;

4. Translate base to move RCM point to target location;

5. Rotate RCM axes to each of five insertion trajectories, insert ceramic needle, and image;

6. Retract needle and translate base axes to move RCM point to each of the new locations, and repeat;

The insertion pathway (tip location and axis) of each needle insertion was manually segmented and determined from the MR image volumes, as seen in Fig. 2.23 for one representative target point. The best fit intersection point of the five orientations for each target location was found, both to determine the effectiveness of the RCM linkage as well as to analyze the accuracy of the system as a whole. The results demonstrated an RMS tip position error of approximately 1.38 mm and an angular error of approximately 2.03° for the six targets, with an error among the varying trajectories from RCM intersection point to needle axes of 0.54 mm.
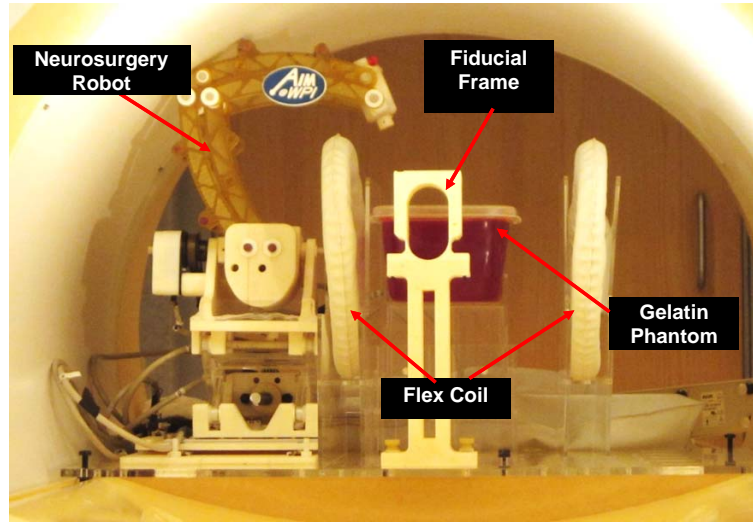
Figure 2.22: Configuration of the robotic device within scanner bore for the MR image-guided accuracy study.
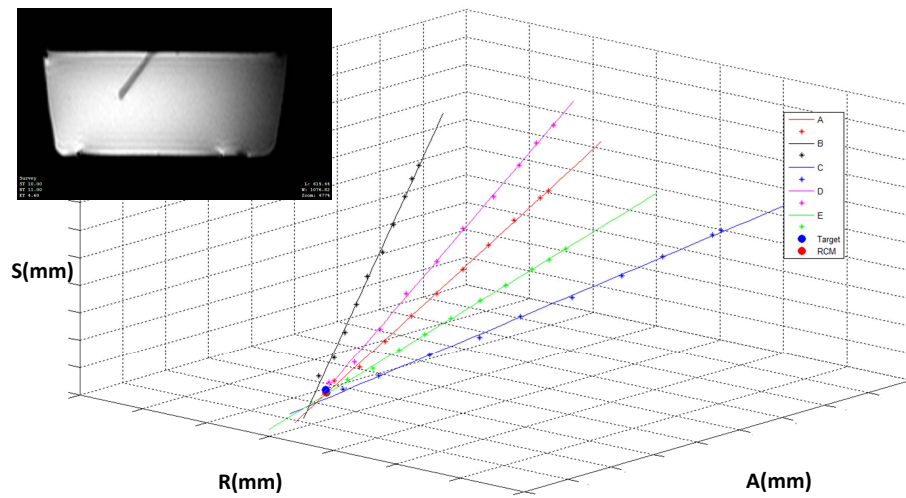
Figure 2.23: Plot of intersection of multiple insertion pathways at a given target location based on segmentation of the MRI data. Each axis is $40mm$ in length. Inset: MRI image of phantom with inserted ceramic cannula.

Table 2.4: Analysis of OTS and Image-Guided Accuracy Studies

		Tip Position (mm)	Distance from Needle Axes(mm)	Insertion Angle (Degree)
Optical Tracker	Maximum Error	1.56	0.44	3.07
	Minimum Error	0.48	0.22	0.90
	RMS Error	1.09	0.33	2.06
	Standard Deviation	0.28	0.05	0.76
MRI-Guided	Maximum Error	2.13	0.59	2.79
	Minimum	0.51	0.47	0.85
	RMS Error	1.38	0.54	2.03
	Standard Deviation	0.45	0.05	0.58

2.3 Precision Conformal Ablation of Brain Tumor

Based on the research endeavor of the previous system with manual insertion, an 8-DOF fully actuated robotic assistant is further developed for performing MRI-guided precision conformal ablation of brain tumors, to eliminate the needs of moving the patient in and out of the scanner during the procedures.

2.3.1 System Architecture

The system is configured with equivalent architecture as previous system includes five major modules: 1) navigation and treatment planning software, 2) robot control software, 3) robot controller, 4) ablation probe manipuator, and 5) MRI scanner, as shown in Fig. 2.24. FDA approved navigation software TheraVision^{TM} (Acoustic

MedSystems Inc., Savoy, IL) developed by our collaborators is utilized to visualize and define treatment region in the MR image volume, and generate treatment plan (e.g. radio frequency (RF) generator power, cooling flow rate, treatment time etc). The robot control software is designed to organize the dataflow and solve robot kinematics. MRI robot controller allows high-precision closed-loop position control of the robot manipulator to operate the ablation probe using the positioning encoder feedback. The desired targets are selected on TheraVision and sent to robot control software via OpenIGTLink communication protocol [46]. Therein, the targets position are resolved to motion commands of each joint based on robot kinematics and then transmitted to the controller to drive the motors and thus place the probe to desired targets. Data transmission betweeen robot control software (running on a laptop inside control console room) and robot controller (residing inside MRI scanner room) is established via fiber optic Ethernet, which runs through the shielded patch panel, to eliminate electric noise that may be introduced into imaging due to transmission of electrical signals. The actual probe position is fed back to TheraVision for visualization and verification.

2.3.2   Clinical Workflow

The workflow of system is proposed based on the conventional stereotactic neurosurgery with Lexsell frame (Elekta Inc., Atlanta, GA), to minimize clinical complications and streamline the design procedures. As shown in Fig. 2.25, the workflow is
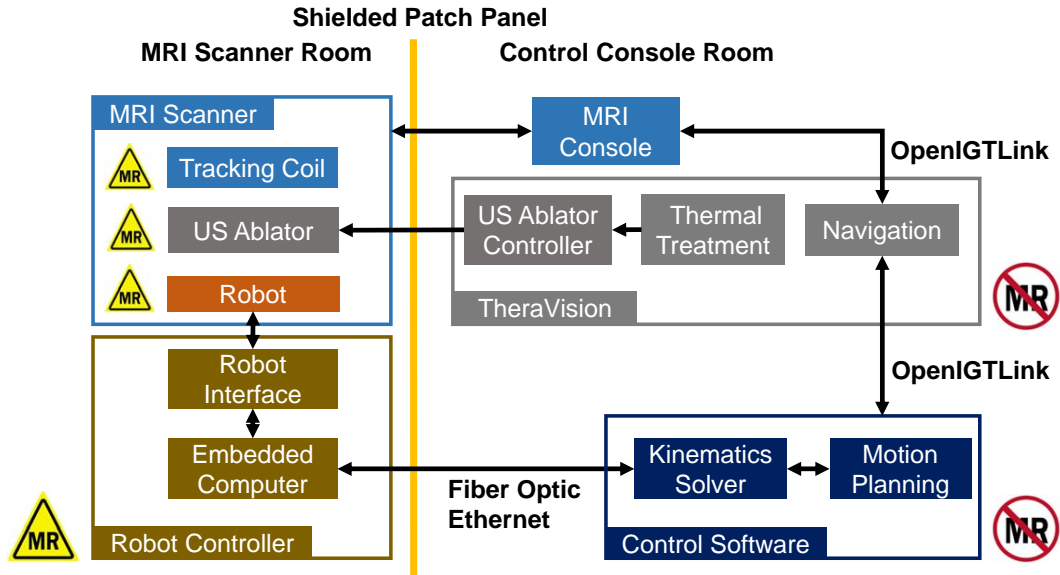
Figure 2.24: System architecture of robotic system for MRI-guided precision conformal ablation of brain tumor.

composed of seven major steps:

1. Patient positioning and system initialization: place the patient in the scanner with supine position and fix the head via point-set-screws. Initialize hardware and software of robot system. Create sterile environment for scanner, patient and robot manipulator.

2. Robot registration: register the robot to the MRI scanner coordinate systems with fiducial frame.

3. Entry point localization: localize skull entry points with robot alignment. Make incision and burr hole.

4. Cannula and probe placement: align the cannula and insert the ablation probe to the desired target through the entry point.

5. Trajectory confirmation: confirm the probe trajectory by imaging the fiducial maker that aligned with cannula axis.

6. Ablation treatment: perform thermal ablation via treatment plan software under real-time MR thermal imaging monitoring.

7. Finalization: retract the probe, remove patient and close incision.
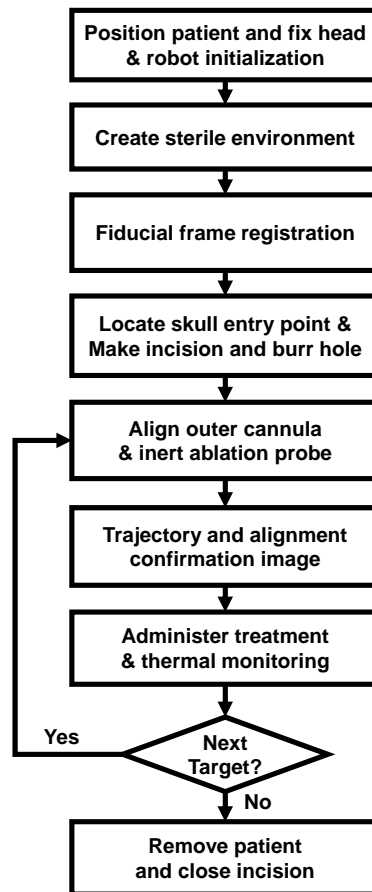
Figure 2.25: Clinical workflow of MRI-guided robot assisted thermal ablation therapy for brain tumor.

2.3.3 Interstitial High Intensity Focused Ultrasound Ablator

Localized heating of tissue with ultrasound interstitial high-intensity thermal therapy is caused by mechanical losses from the propagation of the acoustic waves through the tissue. The longitudinal pressure waves travel through the tissue and have a mechanical force on the molecules, producing oscillatory motion at the applied 5-15MHz. The frictional losses produce heating of the tissue. The nature of coagulation produced is consistent throughout the lesion, without charring or vaporization, as is commonly produced using other thermal techniques. Consistent heating/ablation allows the applicator to be easily removed from the tissue without causing tissue damage. Propagation is dependent on acoustic properties of the tissue, which vary less across tissues than electrical conductivity. The ACOUSTx ablator, an interstitial high intensity focused ultrasound (iHIFU) based applicator, is developed by Acoustic MedSystems Inc. [62–64]. The ACOUSTx ablator contains 2 to 4 tubular ultrasound transducers (5 to 11 mm length), and is designed to be inserted within plastic implant catheters, as shown in Fig. 2.26. Water flow is used to couple the ultrasound, improve thermal penetration and cool the transducers. The transducers are fabricated with sectored shape and separately electronically powered, to provide a specific angular acoustic region or directionally focused for placement at the periphery of a target region, selectively destroying target tissue while preserving critical tissue on the other

side. Use of sectored transducers would enable conformal directional ablation with greater control of the ablation zone shape, size, and volume. This would improve the treatment margin and limit the risk of damaging nearby normal tissue. A rigid cannula is usually inserted first into the brain tiusse to provide straight pathway for the flexible ablator and reduce the bending.
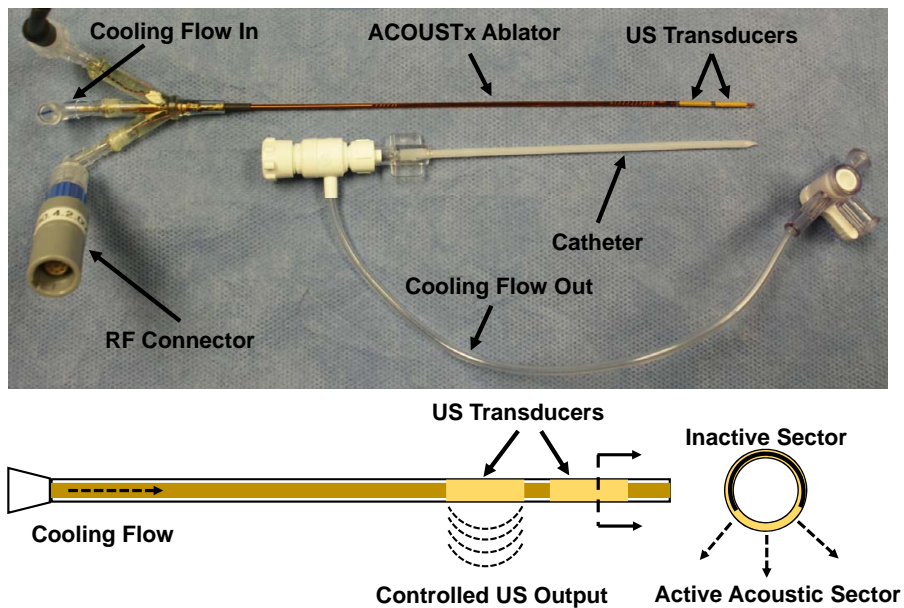
Figure 2.26: (Top) ACOUSTx US ablator with two separate transducer sections. (Bottom) Schematic diagram of the US ablator, showing the directional acoustic sector.

2.3.4 Mechanism Design

2.3.4.1 Design Requirements

The robot manipulator is designed to place the ablation probe via a fixed burr hole on the skull while patient is lying inside high-field closed-bore MRI scanner with

supine position. Since the patient setup is simliar as the aforementioned system for DBS, the mechanism in this application is designed with the same kinematic configuration as the previouse system. Instead of manual insertion of the surgical tools, a 3-DOF fully actuated albator is designed to stream line the workflow and eliminate the needs of moving the patient in and out of the scanner during the procedures.

The manipulator could provide 8-DOF motion to deliver the cannula and ablation probe into the target region through a burr hole, as shown in Fig. 2.27: 3-DOF Cartesian motion to align the probe to the target point, 2-DOF rotary motion to orient the probe around the target point, and 3-DOF manipulation of the cannula and ablation probe to locate and orient the directional transducers towards treatment foci. The 8-DOF motion of the robot enables fully actuated placement of the ultrasonic ablator, and configured kinematically equivalent to the commonly used Leksell frame. The joint space kinematic specifications are summarized in Table. 2.5.

In terms of materials, three main factors are considered: MRI compatibility, stiffness and sterilization. To be compatible with MRI environment, the linkages are machined with MR safe and high stiffness Ultem material. The major body of the robot is made of 3D-printed ABS plastics. In the aspects of sterilization, components that have direct contact with patient is made of sterilizable and bio-compatible material MED 605. The rest of the robot could be draped with sterilized plastic cover to create sterile environment.

From the aspects of actuation method, nonmagnetic piezoelectric actuators have
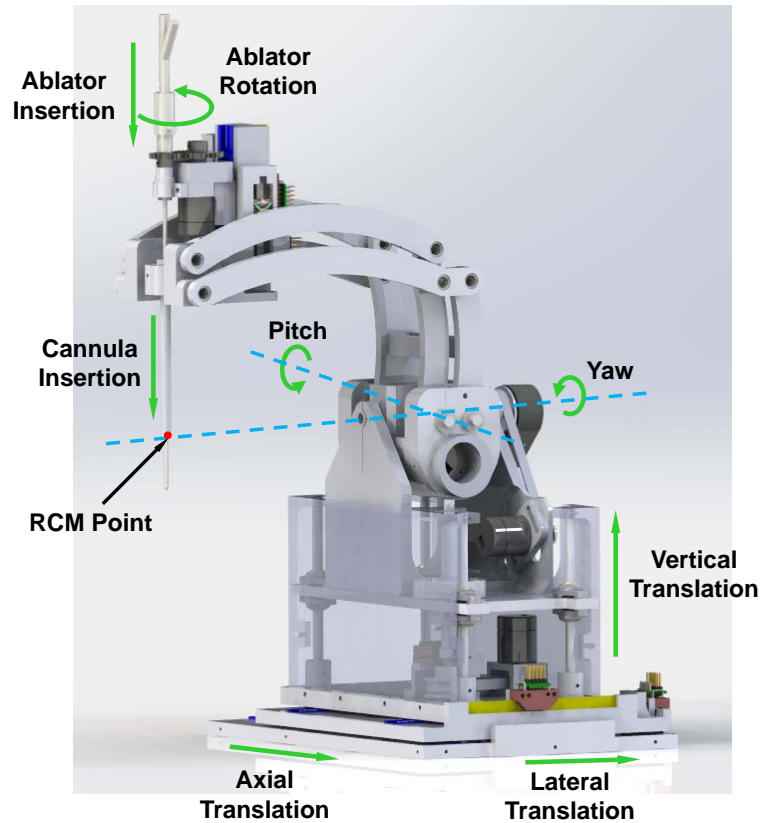
Figure 2.27: 3D CAD model of the thermal ablator manipulator, showing the configuration of degrees of freedoms.

been proved to be able to provide high precision positioning and introduce no visible imaging noise with our custom developed MRI compatible robot controller [41, 65, 66]. In this study, linear Piezomotor (PiezoLegs LL1011C, PiezoMotor AB, Sweden) and rotary Shinsei motor (USR60-S4N, Shinsei Corp., Tokyo, Japan) are utilized for providing linear and rotary actuation respectively.

2.3.4.2 Ablator Alignment Module

The motion of base stage in horizontal plane (DOF #1 and #2) are driven directly by linear Piezomotor via the linear sliders. The orientation arm rides on 4 linear guides and lifted via the lead screw-nut mechanism that is actuated by a rotary Shinsei motor through a timing belt, enabling the vertical translation (DOF #3).

Remote-center-of-motion (RCM) mechanism is commonly used by surgical robots to orient surgical tools inside patient body through a fix entry point. In this study, RCM mechanism is adopted and configured in the form of parallelogram linkage to implement the yaw (DOF #4) and pitch (DOF #5) motion of orientation arm. The rotation axes of yaw and pitch intersect with the probe insertion axis at a mechanically constrained single point, i.e. RCM point, making it kinematically similar to conventional stereotactic frame, wherein the first 3 DOFs place the center of rotation and the next 2 DOFs align the axis of the instrument.

2.3.4.3 Ablator Driver Module

The cannula is mannually attached to the cannula guide and inserted robotically by the linear piezomotor via linear guide (DOF #6). The ablator is inserted manually through the cannula and fixed to the driver through the probe clamp, and then inserted robotically (DOF #7) by the linear Piezomotor directly, and rotated (DOF #8) by a rotary Piezomotor through the gears, as shown in Fig. 2.28. The cannula guide is embedded with 4 MRI visible fiducial tubes to assist the alignment in the

MR images. During the clinical procedures, the ablator driver will be covered by the sterile plastic drape. The gears, probe clamp, and cannula guide, which have direct contact with the patient, will be sterilized and attached to the driver via thumb screws.
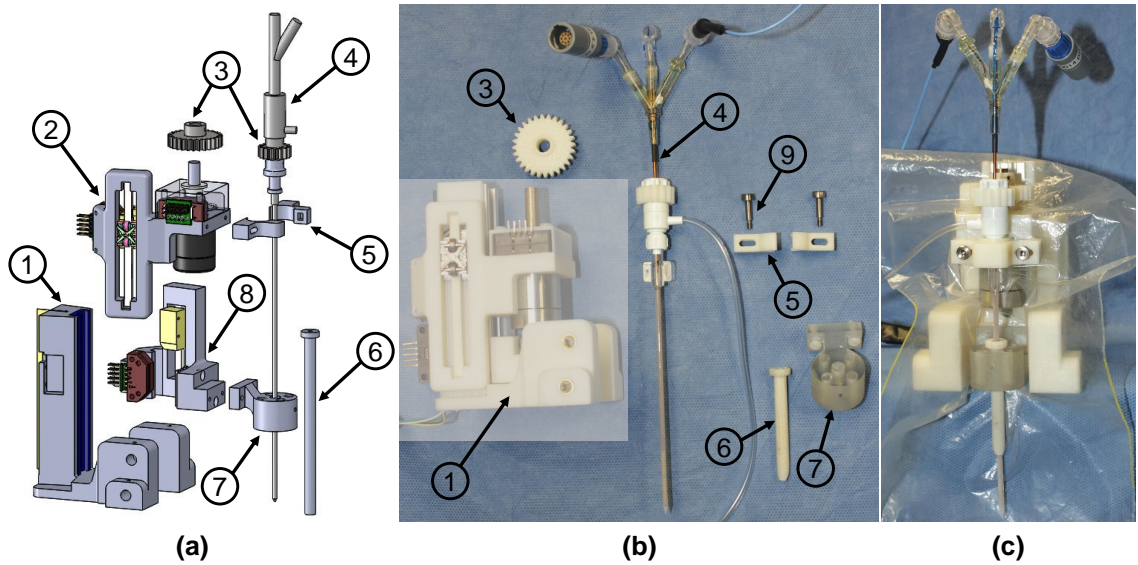
Figure 2.28: 3-DOF ablator driver module. (a) exploded view showing: 1) driver base 2) ablator translation stage 3) gears 4) ablator 5) ablator clamp 6) cannula 7) cannula guide 8) cannula translation stage 9) thumb screw, (b) the components that overlaid with semitransparent square could be covered with sterilized plastic drape and the remained parts are made of biocompatible and sterilizable materials, and (c) assembly of ablator driver covered with plastic drape.

2.3.4.4 Head Frame Adjustment Module

The head frame adjustment module is designed with a tilt DOF in the sagittal plane, to facilitate the insertion of ablator from varying entry points between forehead and occiput, as shown in Fig. 2.29. The angulation of the head is implemented by the scissor mechanism driven by the lead screw-nut mechanism, which transmits linear

motion to angulation. Off-the-shelf MRI compatible Stereotaxy frame (UCHRA, Integra LifeSciences Corporation, NJ) is mounted on the module and utilized to secure the skull via point-set-screws, preventing the head movement during the procedures.

A fiducial frame is firmly attached to the platform through thumb screw during the registration phase, as aforementioned in the clincial workflow Section 2.3.2. The fiducial frame is composed of nine tubes filled with MRI-visible, high contrast fluid (Beekley, Bristol, CT), and configured in a set of Z shapes in each of the three orthogonal planes. Based on imaging the fiducial frame, the 6-D position and orientation of the robot can be localized with respect to the RAS patient coordinates. The robot base is physically fixed in the platform with known offset from the fiducial frame. Hence, the registration is only performed once during the procedure. Once the robot is registered, the fiducial frame is removed from the platform, to reduce potential collision with the ablator manipulator. Fig. 2.30 shows the system setup inside the scanner as the fiducial frame is removed and the ablator manipulator is locked onto the platform.

2.3.5 Robot Kinematics and Registration

The robot kinematics is analyzed based on Denavit-Hartenberg (D-H) parameters. The D-H frame assignment is illustrated in Fig. 2.31, and the D-H parameters are summarized in Table. 2.5. The origin of robot frame F_{Rob} is defined at the robot platform with x-y-z axes aligned with scanner's RAS (Right, Anterior, Superior)
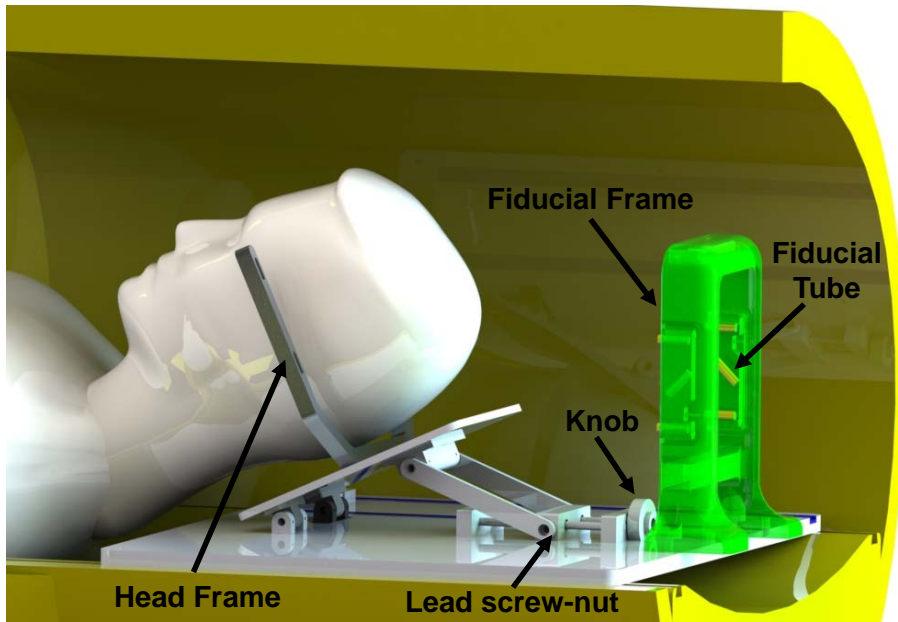
Figure 2.29: CAD model of the head frame adjustment module with patient placed in supine position and the fiducial frame attached on the platform.
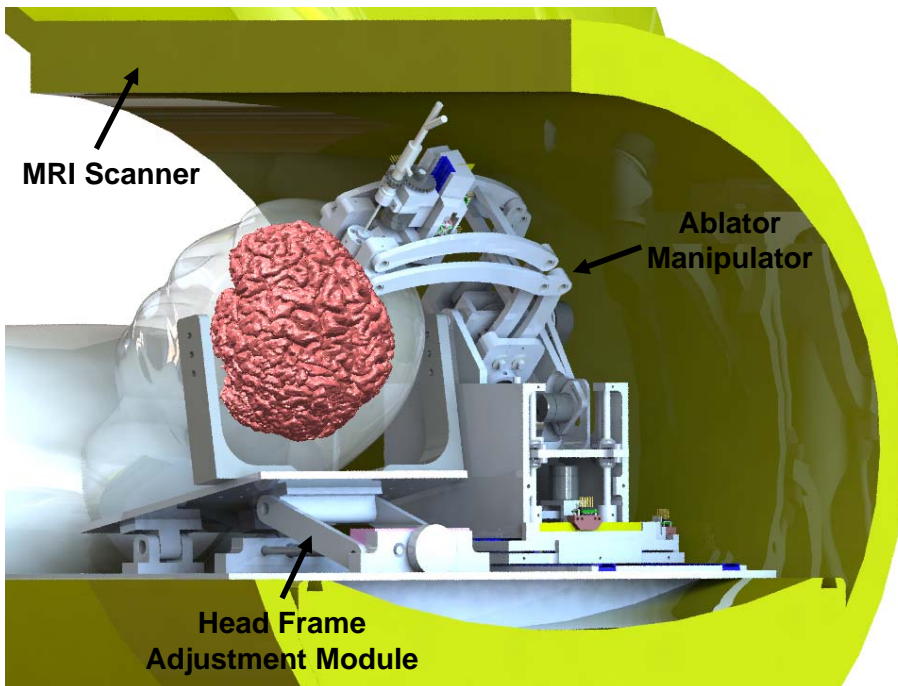
Figure 2.30: CAD model of system setup inside the scanner as the fiducial frame is removed and the ablator manipulator is locked onto the platform.

coordinate system. The base frame F_{Base} is defined as the RCM point at home position, with x-y-z axes aligned with robot frame F_{Rob}. The tip frame F_{Tip} is defined at the tip of ablator, with z-axis pointing along the ablator longitudinal axis, x-axis aligning with robot frame, and y-axis determined by the right hand rule. The forward kinematics of the manipulator can be calculated based on the homogeneous transformation chain, depicted as:

$$T_{Tip}^{Base} = T_1^0 T_2^1 T_3^2 T_4^2 T_5^4 T_6^5 T_7^6 T_8^7$$

$$= \begin{bmatrix} nx & sx & ax & px \\ ny & sy & ay & py \\ nz & sz & az & pz \\ 0 & 0 & 0 & 1 \end{bmatrix} \tag{2.2}$$

$$P = \begin{bmatrix} px \\ py \\ pz \end{bmatrix} = \begin{bmatrix} d_2 + d_6 cos\theta_5 + d_7 cos\theta_5 \\ d_3 + d_6 sin\theta_4 sin\theta_5 + d_7 sin\theta_4 sin\theta_5 \\ d_1 + d_6 cos\theta_4 sin\theta_5 + d_7 cos\theta_4 sin\theta_5 \end{bmatrix} \tag{2.3}$$

69

$$A = \begin{bmatrix} ax \\ ay \\ az \end{bmatrix} = \begin{bmatrix} cos\theta_5 \\ sin\theta_4 sin\theta_5 \\ cos\theta_4 sin\theta_5 \end{bmatrix} \tag{2.4}$$

Where T_{Tip}^{Base} is transformation from tip to robot base, P is the ablator tip position, and A is the vector along the ablator longitudinal axis.
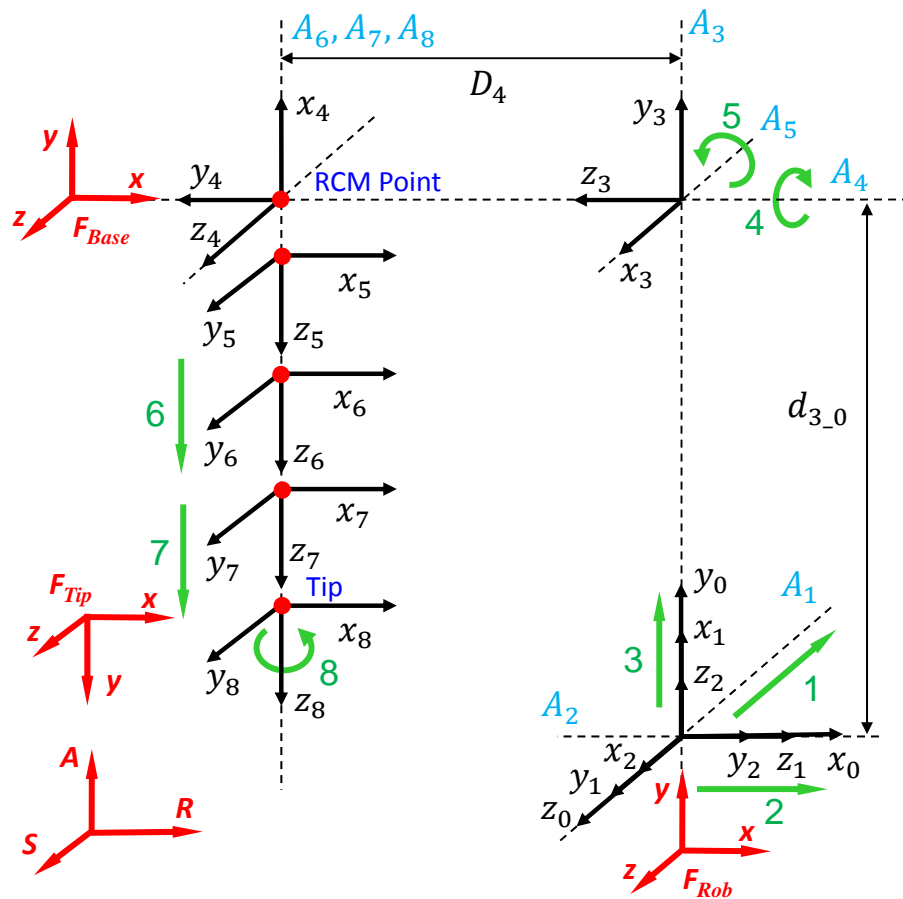
Figure 2.31: D-H frame assignment of the 8-DOF ablator manipulator.

The ablator tip is usually defined at the RCM point as the target position, and

Table 2.5: D-H Parameters of Robot Manipulator

Axis	Motion	l_i	α_i	d_i	θ_i	Range
1	Axial	0	90	d1	90	0~50mm
2	lateral	0	90	d2	90	0~40mm
3	vertical	0	90	d3	0	0~50mm
4	Yaw	0	90	D4	θ_4	0~90°
5	pitch	0	90	0	θ_5	-45~45°
6	Cannula insertion	0	0	d6	0	0~40mm
7	Probe insertion	0	0	d7	0	0~30mm
8	Probe rotation	0	0	0	θ_8	-180~180°

the cannula is inserted 30mm away from the ablator tip. Therefore, d_6, d_7 are constant value for certain ablator design, i.e. $d_6 = D_6, d_7 = D_7$ (D_6, D_7 are constant determined by the length of the ablator and cannula). However, additional flexibility in path planning may be afforded by using a variable d_6, d_7. Ablator and cannula with varying length could be adopted for different target foci. The rotation of the ablator θ_8 is an independent control input determined by the tumor geometry, which could be defined by optimizing the thermal treatment shape and not discussed in the kinematics of this study. By defining $d_6 = D_6, d_7 = D_7$, the inverse kinematics can be written as:

$$d_1 = pz - D_6 cos\theta_4 sin\theta_5 - D_7 cos\theta_4 sin\theta_5$$

$$d_2 = px - D_6 cos\theta_5 - D_7 cos\theta_5$$

$$d_3 = py - D_6 sin\theta_4 sin\theta_5 - D_7 sin\theta_4 sin\theta_5$$

$$\theta_4 = atan2(ay, az) \tag{2.5}$$

$$\theta_5 = acos(ax)$$

$$d_6 = D_6$$

$$d_7 = D_7$$

As aforementioned in Section 2.3.4.4, fiducial frame based registration is utilized to register the robot to the patient R-A-S coordinate system. Images of the fiducial frame are acquired to calculate the robot registration transform using line marker registration [67]. The calculated registration transform is sent over a network via OpenIGTLink to the robot control software, where it is used to calculate the 6-DOF ablator tip pose in patient coordinates through the transformation chain, written as:

$$T_{Tip}^{RAS} = T_Z^{RAS} T_{Base}^Z T_{Tip}^{Base} \tag{2.6}$$

Where T_{Tip}^{RAS} is ablator tip pose represented within the RAS coordinate system, T_Z^{RAS} is fiducial frame pose with respect to RAS coordinate system determined by the registration, T_{Base}^Z is the constant offset from the robot base to the fiducial frame,

and T_{Tip}^{Base} is the ablator tip position with respect to the robot base, as determined by the robot kinematics.

2.3.6 Experiments and Results

Three sets of experiments were performed to validate the feasibility of the system design and evaluate the positioning accuracy. The system accuracy was first assessed in free space with OptiTrack motion capture system, and further assessed with phantom studies inside a 3T MRI scanner. A preliminary study of thermal ablation was conducted with ex-vivo chicken breast tissue to evaluate the system workflow.

2.3.6.1 Free Space Positioning Accuracy Evaluation

The free space positioning accuracy was conducted with an OptiTrack motion capture system (NaturalPoint, OR). A 6-D reference marker frame is firmly attached on the robot platform, and a 6-D tracking frame is mounted on the needle driver, as shown in Fig. 2.32. The robot is moved to six target locations, and orientated to five different angulations at each target location, resulting in 30 needle poses in total. Three metrics are utilized for analyzing system error, i.e. tip position, insertion angle and distance from RCM intersection point to needle axes. Tip position error is a measure of the distance between a selected target and the actual location of the tip of the inserted cannula. Insertion angle error is measured as an angular error between the desired insertion angle and the actual insertion angle. Distance from RCM inter-

section point to needle axes represents an analysis of the mechanism's performance as a RCM device. The 6-D actual needle pose is measured by the OptiTrack system, and registered to the desired targets with point cloud based registration to eliminate registration-related errors. The experiment data analysis demonstrate that the root mean square (RMS) error of tip position is $1.11 \pm 0.43mm$, and the error from RCM intersection point to needle axes is $0.27\pm0.06mm$. The position and orientation error in each axis is illustrated in Fig. 2.33, indicating the RMS errors in X-axis (0.35mm), Y-axis(0.62mm), Z-axis(0.85mm), Yaw-axis(0.46°), and Pitch-axis(1.10°).
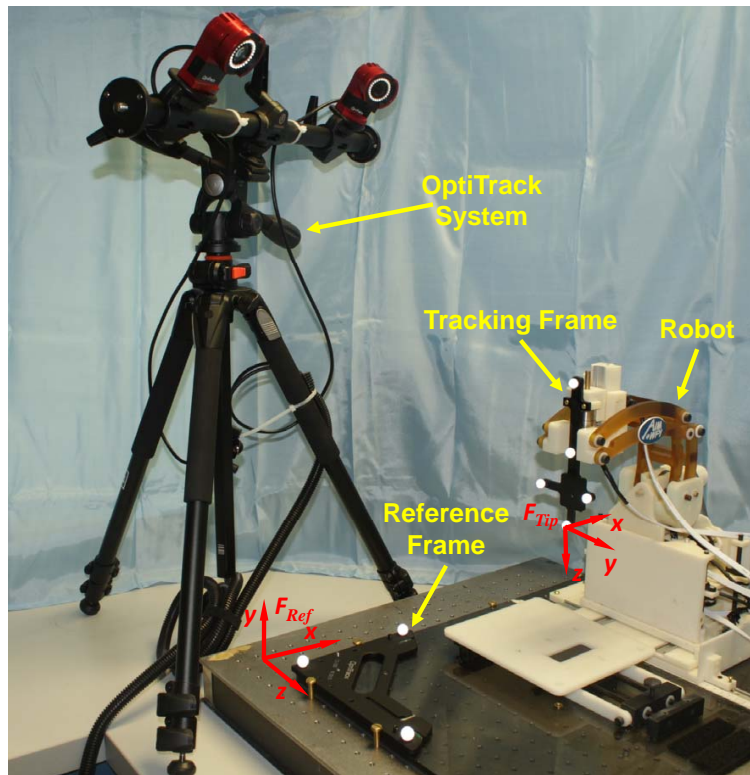
Figure 2.32: Experiment setup of the free space accuracy evaluation with OptiTrack motion capture system.
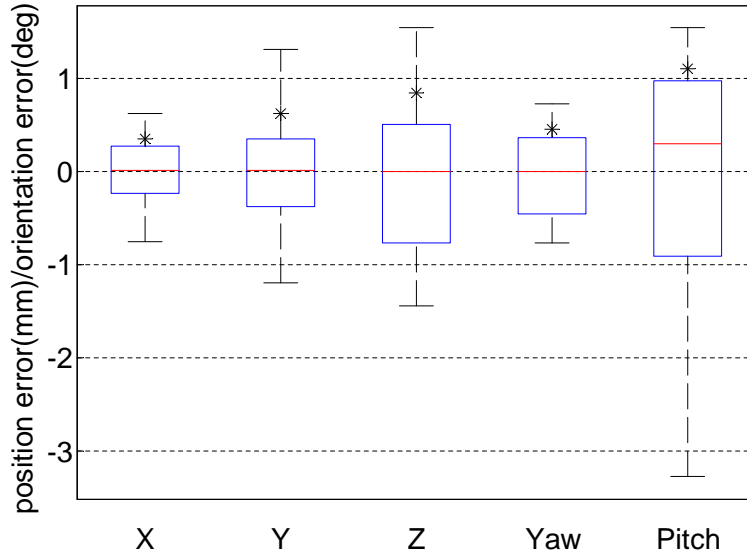
Figure 2.33: Box plot of the position and angle error in each axis. ∗ represents for the RMS error.

2.3.6.2 System Accuracy Evaluation with MRI Phantom Studies

The system level accuracy was assessed with phantom studies inside MRI scanner, as shown in Fig. 2.34. A 13-gauge brass needle with rounded flat tip was inserted into a gelatin phantom and imaged with T2-weighted turbo spin echo (T2W-TSE) imaging protocol (TE: 115ms, TR: 3030ms, flip angle: 90°, slice thickness: 3mm) to measure the actual needle trajectories. Three RCM locations were targeted from five different orientations for each single location, resulting in 15 needle insertions in total. The actual trajectory of each needle insertion was manually segmented and measured from MR images and compared to the desired targets to analyze the system accuracy. The experimental results demonstrated the RMS error of the tip position is $1.45 \pm 1.29mm$, orientation error is $1.53 \pm 1.36°$, the error from RCM intersection

point to needle axes is $0.75 \pm 0.67mm$. Fig. 2.35 illustrates one representative target location with five different orientations.
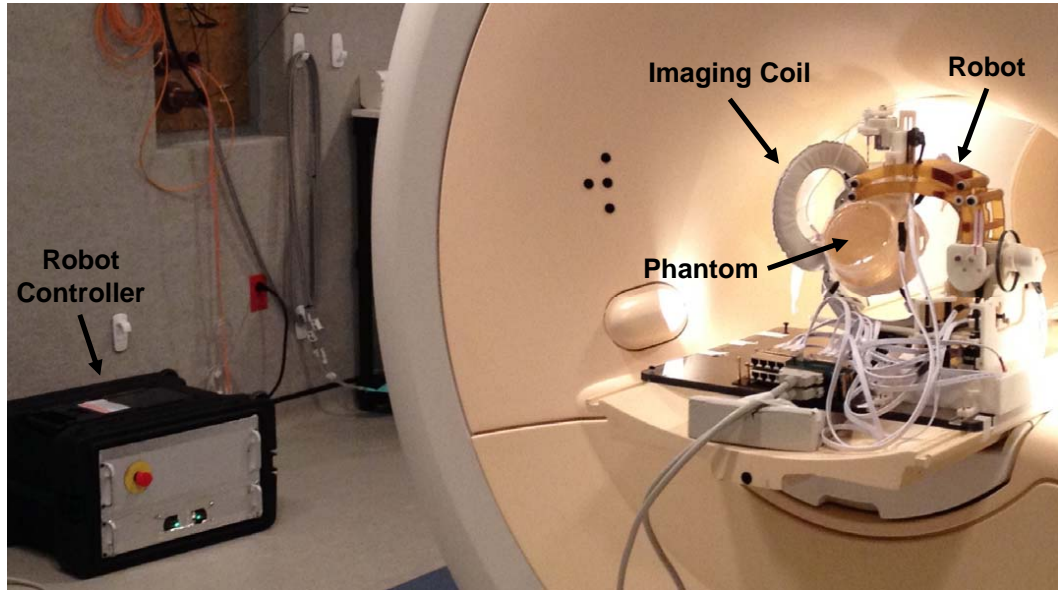
Figure 2.34: Experiment setup of the robotic device within scanner bore for the MRI phantom accuracy study.

2.3.6.3 Demonstration of Thermal Ablation Within Ex-Vivo Tissue

The viability of the system to perform thermal ablation treatment is validated through an initial ex-vivo tissue study. A fresh chicken breast tissue was modeled into gelatin phantom (to prevent tissue movement during insertion) and used as the specimen. An US ablator with 90° active sector was utilized to perform the ablation treatment. Two target locations were selected inside the ex-vivo tissue and treated with thermal ablation. The position and angulation errors for the two insertions are
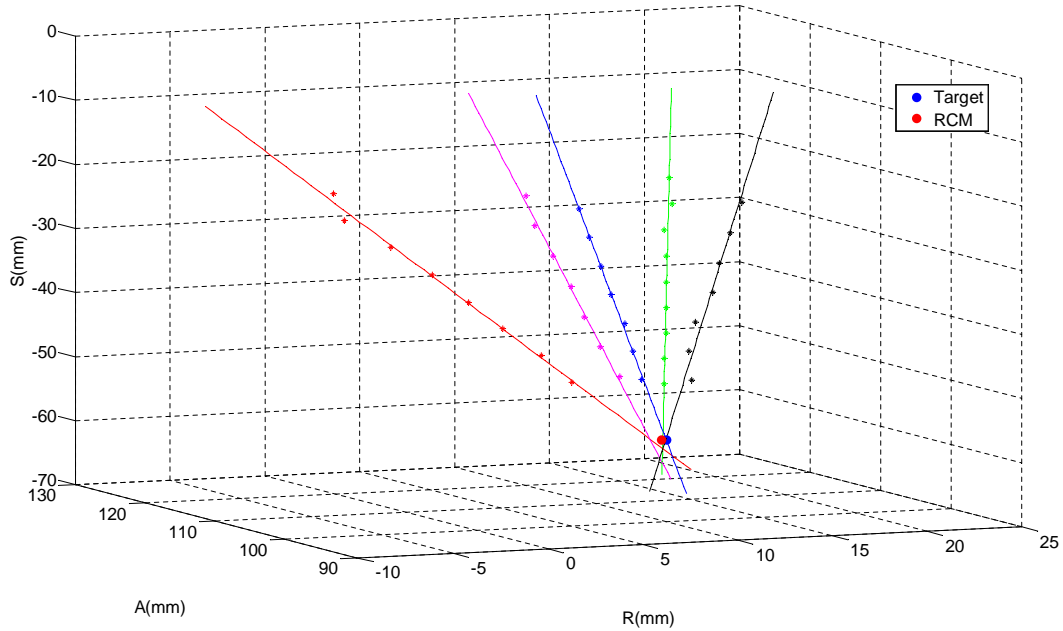
Figure 2.35: Plot of intersection of multiple insertion pathways at a given target location based on segmentation of the MRI data.

$3.5mm$, $3.9°$ and $4.3mm$, $4.3°$ respectively. Fig. 2.36 demonstrates a representative MR image of ablator track, and Fig. 2.37 shows the treated tissue with thermal ablation. The system workflow is further validated through an ex-vivo lamb brain ablation. A lamb head was fixed on the head frame and set to an appropriate angulation via the head frame adjustment module. An US ablator with $180°$ active sector was utilized to perform the ablation treatment. One target in the lamb brain was placed by the robot. The experiment setup is shown in Fig. 2.38, and the ablator track in the lamb brain is visualized on MR image as illustrated in Fig. 2.39. The position and angulation errors for the insertion are $0.5mm$ and $2.0°$ respectively.
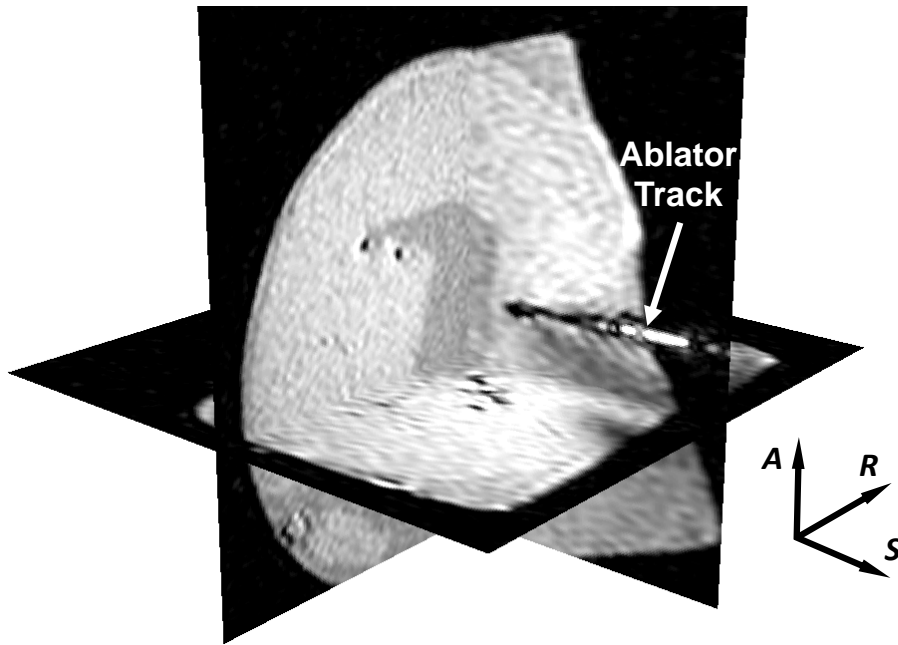
Figure 2.36: MR image showing a representative track of US ablator inserted inside an ex-vivo chicken breast tissue.
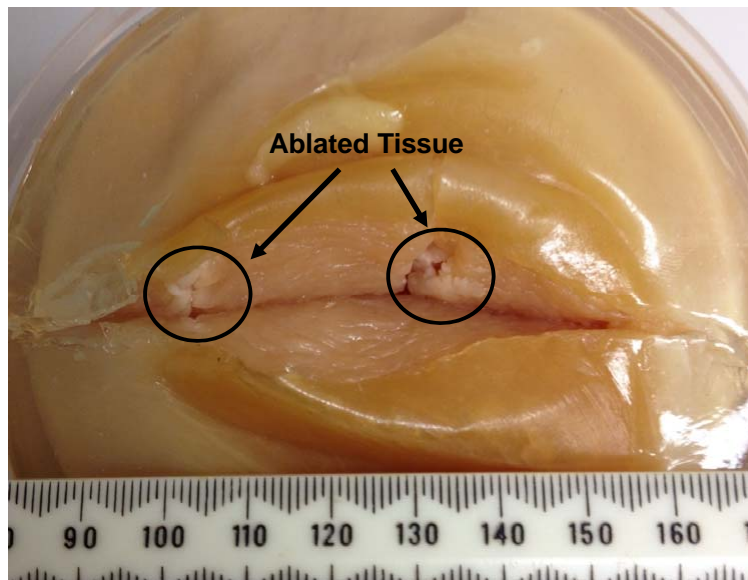
Figure 2.37: Ex-vivo chicken breast tissue with two thermal ablated foci.
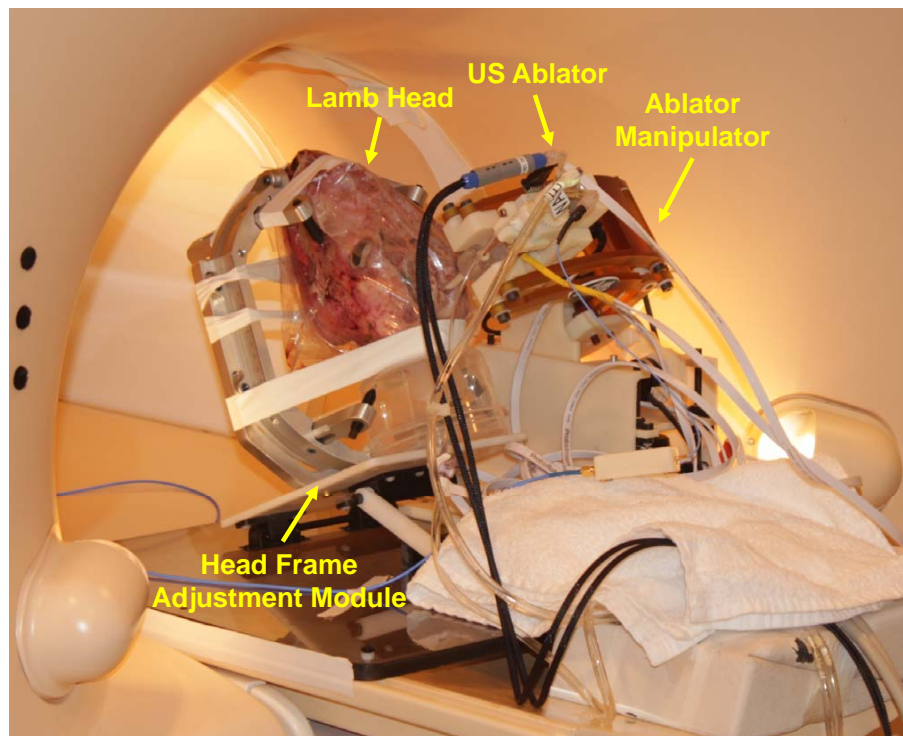
Figure 2.38: Experiment setup for thermal ablation on ex vivo lamb brain.
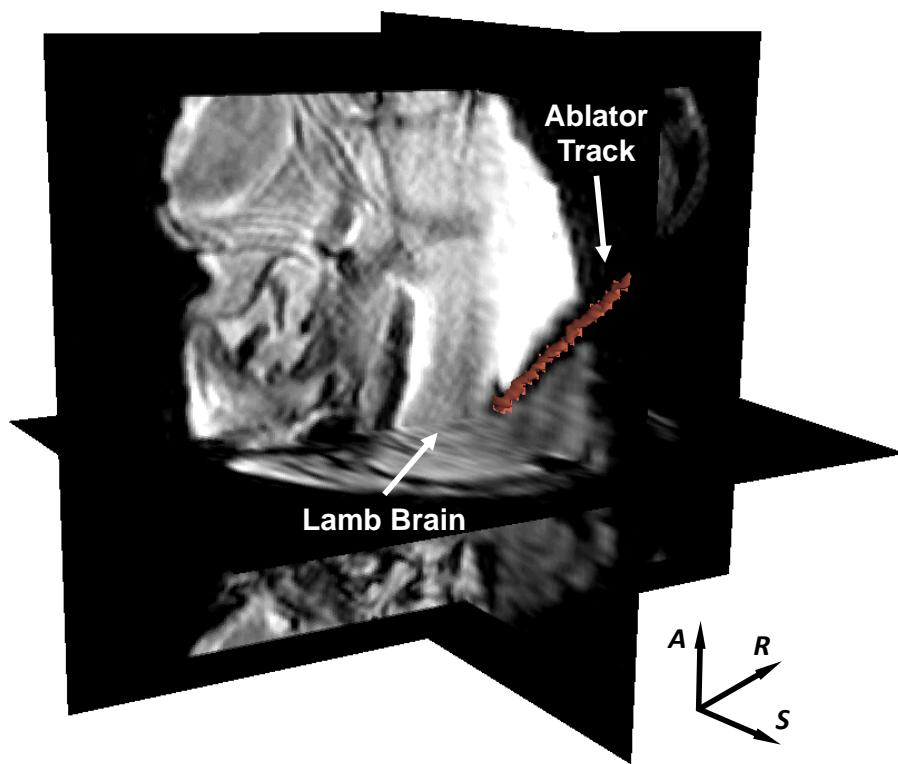
Figure 2.39: MR image showing a representative track of US ablator inserted inside an ex-vivo lamb brain.

2.4 Discussion and Conclusion

This chapter presents the development of two generations of MRI-guided stereotactic neurosurgery robot with piezoelectric actuation that enables simultaneous imaging and intervention without affecting the imaging functionality. The contributions of this chapter include: 1) novel mechanism design of a stereotactic neurosurgery robot, 2) piezoelectric motor control electronics that implements direct digital synthesis for smooth waveform generation to drive piezoelectric motors, 3) an integrated actuation, control, sensing and navigation system for MRI-guided piezoelectric robotic interventions, 4) image quality benchmark evaluation of the robotic system, and 5) targeting accuracy evaluation of the system in free space and under MR guidance.

Evaluation of the compatibility of the robot with the MRI environment in a typical diagnostic 3T MRI scanner demonstrates the capability of the system of introducing less than 15% SNR variation during simultaneous imaging and robot motion with no visually observable image artifact. This indicates the capability to visualize the tissue and target when the robot operates inside MRI scanner bore, and enables future fully-actuated system to control insertion depth and rotation while acquiring real-time images. Geometric distortion analysis demonstrated less than 0.20% image distortion which was no worse than that of baseline images without the robot present. There is no consensus on the design requirements for the SNR reduction and geometric distortion. The imaging quality achieved by this system is much better than other studies [14, 15], which reported 40% − 60% SNR reduction. Based on our studies, it

is sufficient to perform precise fiducial frame registration and target localization.

Targeting accuracy was evaluated in free space through benchtop studies and in a gelatin phantom under live MRI-guidance. The plastic material and manufacturing-induced errors result in the axes not being in perfect alignment relative to each other, and thus resulting in system error. 3D printed materials utilized in the construction of this device are very useful to rapidly create a mechanism for initial analysis, though upon disassembly, plastic deformation of the pivot locations for the parallelogram linkage were observed, and thought to have added to system inaccuracies; these parts would be machined from PEEK or Ultem in the clinical version of this system to improve stiffness and precision. In addition, large transmission distances on the two belt drive axes may be associated with angular inaccuracies. As indicated by the accuracy analysis in Table 2.4 and Fig. 2.35, the mechanism could be designed with relatively high precision of RCM intersection accuracy. But the positioning accuracy in each axis may be affected by the backlash and deformation of the transmission mechanism at each joint. As demonstrated in Fig. 2.33, the standard deviations of position accuracy for each axis are different. Isotropic gelatin phantom is utilized as a test medium for assessing the targeting accuracy in MRI, demonstrating the RMS error around 1mm. The accuracy may be decreased if the inhomogeneous soft tissue is targeted, as indicated in Section 2.3.6.3 where ex vivo soft tissue is utilized, due to the deflection of needle caused by the asymmetric needle tissue interaction force. To reduce the deflection, a rigid cannula is usually inserted first into the brain tiusse

30mm away from the target to provide straight pathway for the flexible ablator. MR image-based dynamic tracking of the surgical tools could also be used for correcting the placement errors.

This work aims to address three unmet clinical needs, namely efficiency, accuracy and safety. In terms of the efficiency, we compared the workflow of the current manual-frame approach and the MRI-guided robotic approach, revealing the potential to save 2-3 hours by avoiding an additional CT imaging session with associated CT-MRI fusion and the time-consuming localization method (i.e. microelectrode recording). In terms of the accuracy, MRI-guided needle placement accuracy experiment demonstrated 3-axis RMS error 1.38 ± 0.45 mm. The accuracy of traditional frame-based stereotaxy DBS with MRI guidance is 3.1 ± 1.41 mm for 76 stimulators implantation in human [43]. It is premature to corroborate the accuracy advantage of robotic approach due to the lack of clinical human trials. However, it shows the potential of the robotic approach to improve accuracy, by postulating that motorized solution is superior to the manual method. In terms of the safety, since the intraoperative brain anatomy, targets, and interventional tool are all visible with MR during the intervention, this enables compensation for brain shift and complete visualization of the interventional site during the procedure. Qualitatively, image-guidance is empowered with the obvious advantages over the indirect method (i.e. microelectrode recording) which is iterative, time-consuming, and unable to visualize any anatomy.

The currently intended application of the system is for DBS electrode placement and

brain tumor ablation. But as a generic MRI-compatible motion control system, this platform has the capability to be extended for other neurosurgical procedures with different interventional tools. Further experiments include validation of the procedure time and targeting errors with cadaver and animal studies, aiming to improve the patient outcome as the final goal.

Chapter 3

Robotic System for MRI-Guided Transperineal Prostate Interventions

This chapter presents the development, pre-clinical evaluation, and preliminary clinical study of a robotic system for transperineal prostate biopsy under direct magnetic resonance imaging (MRI) guidance. The clinically integrated robotic system is developed based on modular design approach, comprised of surgical navigation user interface, robot control software, MRI robot controller, and needle placement manipulator. The system enables the technologies for MRI-guided procedures, making it readily transported and setup for supporting clinical workflow of interventional procedures, as well as readily extensible and reconfigurable to other clinical applica-

tions. Preclinical evaluation of the system is performed with phantom studies in a 3 Tesla MRI scanner, rehearsing the proposed clinical workflow and demonstrating the in-plane targeting error of $1.5mm$. The robotic system has been approved by the institutional review board (IRB) for clinical trials. A preliminary patient study is conducted with the IRB approval and patient consent, demonstrating the targeting errors at two biopsy target sites of $4.0mm$ and $3.7mm$, which is sufficient to target a clinically significant tumor foci. First-in-man trials to evaluate the system's effectiveness and accuracy for MR image-guide prostate biopsy are underway.

Manual insertion is utilized in the clinical grade system for the sake of perceived safety and user acceptance. However, manual insertion is still time consuming and may lead to needle placement errors. A prototype version system with full actuation is further developed in this chapter to place the needle and perform automatic prostate biopsy and brachytherapy.

This work is performed in collaboration with Clare Tempany, Nobuhiko Hata and Junichi Tokuda at Brigham and Women's Hospital, Harvard Medical School; Iulian Iordachita and Sohrab Eslami at Johns Hopkins University; Clif Burdette and Tamas Heffter at Acoustic MedSystems Inc.

3.1 Introduction

Prostate cancer is the second most common cancer and the second leading cause of cancer death in American men. According to the American Cancer Society, about 1 man in 7 will be diagnosed with prostate cancer and 1 man in 39 will die of prostate cancer [68]. Transrectal ultrasound (TRUS) is the current standard imaging modality for guiding prostate biopsy and brachytherapy seed placement, but the relatively low image quality can only offer minimal specific information of the prostate tumor, which limits its ability to precisely localize suspicious focal lesions [69, 70]. Fig. 3.1 illustrates the US guided prostate biopsy and brachytherapy. MRI is an alternative and ideal modality for surgical guidance due to its ability to perform multi-parametric and high resolution soft tissue imaging without ionizing radiation [71]. To date, significant efforts have been investigated to develop robotic system that perform MRI-guided prostate interventions. These systems range from manually operated devices [72–75], pneumatically actuated robotic systems [3–5, 7, 9, 11], and piezoelectrically actuated robotic systems [13, 14]. Although several MRI-guided robotic systems have demonstrated feasibility of performing interventional procedures in phantom studies, only very few of them have been tested clinically including [12, 72, 76, 77]. Further development and thorough clinical certification are required to advance for clinical use, especially from the perspective of MRI compatibility, targeting accuracy, clinical workflow, safety mechanisms and sterilization.

The focus of this chapter is to develop a clinical-grade robotic system that enables
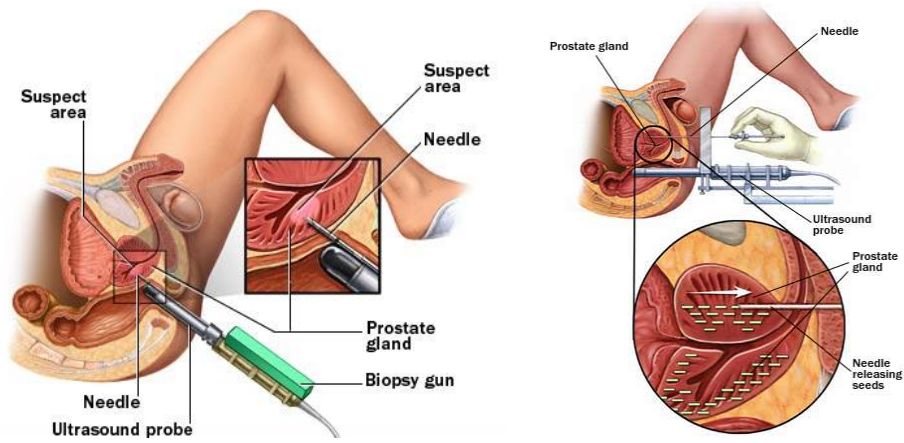
Figure 3.1: (Left)US-guided prostate biopsy, and (Right) prostate brachytherapy.(Credit: Mayo Foundation)

prostate interventions under direct intraoperative MRI-guidance. Iterative design process is involved with a prototype version and a clinical grade version, addressing the engineering topics of mechatronics and control system. The primary contributions of this study are: 1) development of a complete clinically integrated robotic system, which has been approved by IRB for clinical trials; 2) preclinical evaluation with MRI phantom studies, validating the system targeting accuracy and clinical workflow; 3) demonstration of clinical application with a preliminary patient study. 4) development and evaluation of a fully actuated robotic system for autonomous prostate biopsy and brachytherapy.

3.2 System Architecture

This system is developed to optimize a typical prostate biopsy procedure under MRI guidance by assisting the manual procedure using a robotic needle alignment device.

Though optimized for prostate biopsy procedures, it adopts a modular design approach making the architecture capable of supporting various needle-based interventional procedures. The system comprises four major modules: 1) surgical planning and navigation user interface, 2) robot control software, 3) MRI-compatible robot controller, and 4) needle placement manipulator. In the beginning of the procedure, 3D-Slicer [78] is used to prepare the surgical plan by registering the intraoperative images to the preoperative planning images based on the deformable registration method [79]. Targets now defined in the intraoperative images are transferred to the surgical navigation user interface RadVision^{TM}, a brachytherapy treatment planning system that has received FDA 510(k) clearance (Acoustic MedSystems Inc., IL, USA). RadVision visualizes the targets in image space, registers the robot's coordinate frame to the MR images, and forwards the registered targets to the robot control software via OpenIGTLink communication protocol [46].

The robot control software computes the robot kinematics and motion control plan, resolving the targets from task space (patient coordinates) to joint space (robot motions). The custom MRI robot controller is developed to provide high precision and position-based closed-loop control of the ultrasonic piezoelectric motors using encoder outputs. Fiber optic Ethernet, running through the patch panel of MRI scanner room, establishes the connection between the robot control software (running on a computer in the console room) and robot controller (residing beside the MRI scanner), to eliminate the transmission of any electrical signals into the scanner room that may

introduce noise during imaging. Fig. 3.2 illustrates the clinical system configuration, distinguishing the components inside the MRI scanner room and the control console room. Fig. 3.3 further depicts the system architecture and data flow between various modules of the system.
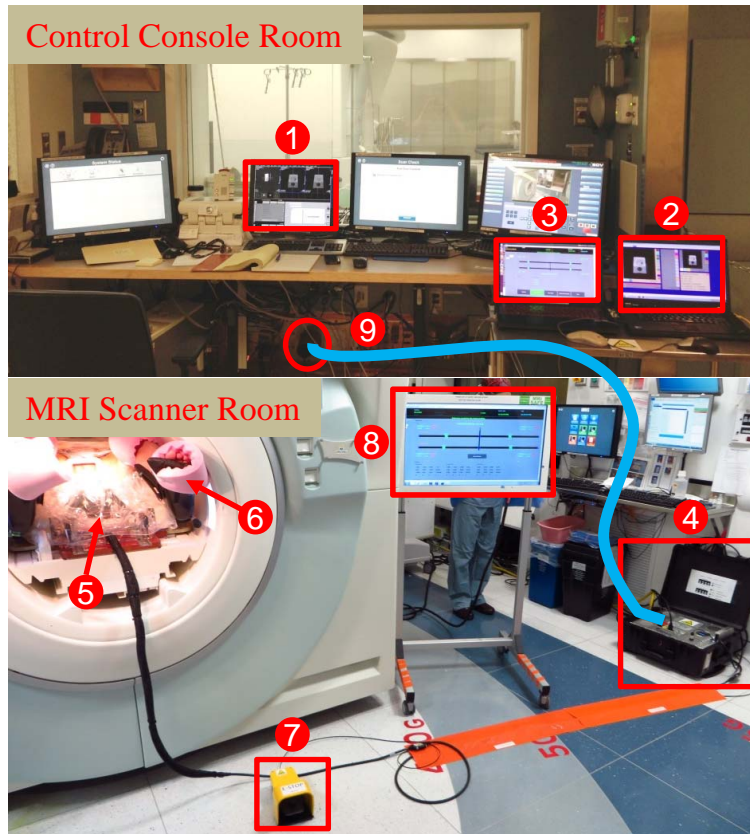
Figure 3.2: Clinical system configuration. In the control console room: (1) MRI control console, (2) surgical navigation user interface, and (3) robot control software. Inside the scanner room: (4) MRI compatible robot controller, (5) robotic manipulator inside the scanner bore covered with sterile drape, (6) patient lying inside the scanner bore in semi-lithotomy position, (7) foot-pedal, and (8) MRI-compatible display showing robot status to the clinician. Communication between the control room and scanner room is through (9) fiber optic cable.

Communication between all of the modules is through network-based media (except between robot controller and physical manipulator which is shielded cable with
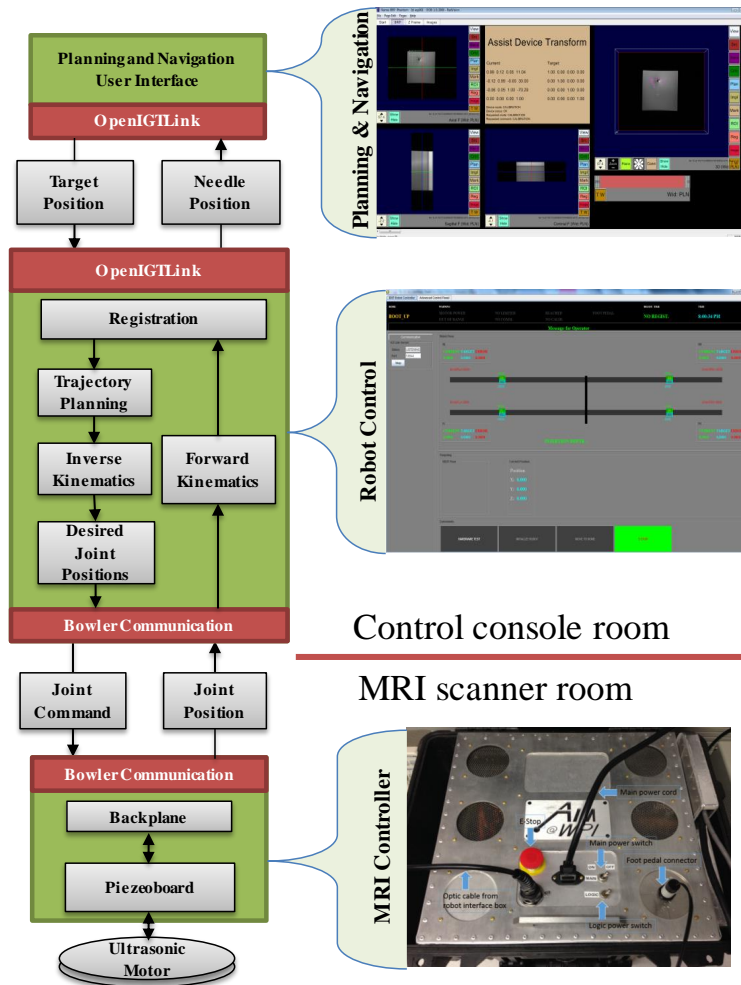
Figure 3.3: System architecture and data flow: Left) Primary system modules and data flow among them using OpenIGTLink and Bowler communication protocols, Right) Corresponding software and hardware components.

differential signaling). This implies that not only each module's operating platforms (e.g. Windows, Linux, and OS X), but also the programming languages (e.g. C++, C, Java) are independent. Moreover, each module of this system could be potentially replaced with other modules of equivalent functionality (e.g. the robot manipulator designed for prostate biopsy in this study could be replaced with another manipulator designed for stereotactic neurosurgery [41]) or a simulation at any level to aid in

development and validation.

3.3   Clinical Workflow

The clinical robot-assisted workflow is intended to mimic that of the traditional template-based prostate interventions [80], allowing similar location of surgical personnel and use of standard equipment. The primary workflow steps are as follows:

1. Place patient board inside MRI scanner bore, position patient on the board in semi-lithotomy position.

2. Image the fiducial frame (attached to patient board) and the prostate of patient.

3. Register the robot to image space (i.e. patient coordinates) based upon fiducial frame images.

4. Register intraoperative images to preoperative images and define/confirm the targets.

5. Initialize the robot outside the scanner bore.

6. Cover the robot with sterile drape and attach the sterile needle guide.

7. Slide the robot into the patient board and lock in place.

8. Set a target in image space using navigation user interface.

9. Align the robot automatically and insert the needle manually.

10. Take confirmation images to verify needle tip position.

11. Collect biopsy sample and retract the needle manually.

12. Repeat steps $8-11$ for each suspected lesion.

Patient preparation, including patient positioning, anesthesia, and configuring the sterile field, matches the conventional template-based procedures, helping ensure a level of comfort among the clinical team with the use of the robotic device. For aligning the robot manipulator and inserting the needle, the workflow is managed and enforced by the robot control software. Fig. 3.4 illustrates the robot control workflow and corresponding stages of the clinical procedure. The well-defined steps of the finite state machine are ensured in both the user interface and robot control software, guiding the user. The system ensures that the workflow are secure and maintained, allowing only validated state transitions to pass through. Invalid transitions (e.g. sending target without a valid registration) are abandoned and reported to the user. Once the robot manipulator is aligned (with motion only occurring while a footpedal is asserted), the actuators are locked to prevent any unintentional motion during the needle insertion stage.
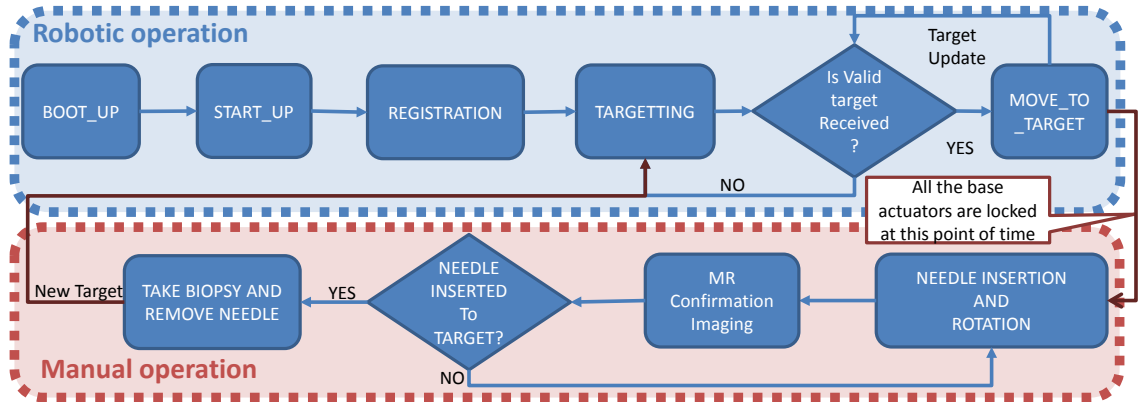
Figure 3.4: Flowchart of the robot control workflow and robot operation modes, showing only valid transitions from one state to another.

3.4 Electromechanical System Design

3.4.1 Needle Placement Parallel Manipulator

The robot manipulator is designed by our collaborator Dr. Iordachita and Dr. Eslami at Johns Hopkins University to perform in-bore prostate transperineal interventions with the patient lying in the supine position and legs in the semi-lithotomy configuration [65]. To cover the entire volume of prostate and accommodate patient variability, the manipulator is designed to provide 4-DOF actuated motion (2-DOF translation and 2-DOF angulation) for aligning the needle with two trapezoid stages, as shown in Fig. 3.5. Each trapezoid stage is constructed of a U-shape frame supported by two parallelogram linkage mechanisms on linear sliders. The sliders are actuated by a lead-screw mechanism driven by an ultrasonic piezoelectric motor (USR60-S4N, Shinsei Corp., Tokyo, Japan) via a pulley-belt mechanism. The two trapezoid stages

are connected through two rigid bars with ball-socket joints at the front and spherical bearing at the rear to allow angulation. A needle guide is attached on top of the trapezoid stages via spherical joints on the rigid bars for guiding the needle insertion trajectory. Two guide holes are incorporated into the needle guide with a vertical spacing of $35mm$ to enhance the reachable workspace and account for patient anatomy and placement variability. The robot manipulator platform slides into the patient board on two linear rails and is repeatably locked in place with locking screws. The sterile fiducial frame comprises nine embedded MRI-visible fluid tubes (MR-Spots, Beekley Corp., Bristol, CT) is repeatable fixed on the centerline of the patient board. The fiducial tubes are configured in three sets of "Z" shapes in three orthogonal planes. The fiducial frame is also used to help constrain the skin of the patient's perineum and maintain the robot's workspace between the patient's legs.

In terms of the materials, three main factors are considered: MRI compatibility, stiffness, and sterilizability. The manipulator is made of non-ferrous materials to be compatible with MRI environment. The body of the robot, including the trapezoid stages, is machined with high strength Polycarbonate filled with 20% fiberglass to maintain high stiffness of the mechanism. The needle guide and fiducial frame, which have direct contact with patient, are 3D printed with biocompatible Ultem (Polyetherimide) and Polycarbonate, respectively. The sterile components have been certified by Nelson Labs (Salt Lake City, UT) for sterilization using Sterrad 100S system (Advanced Sterilization Products, Irvine, CA). All the other components of

the manipulator are covered with a disposable, pre-sterilized clinical plastic drape to create the sterile environment. Detailed descriptions of mechanism design, robot kinematics, and workspace analysis were presented in our previous work [65, 81].
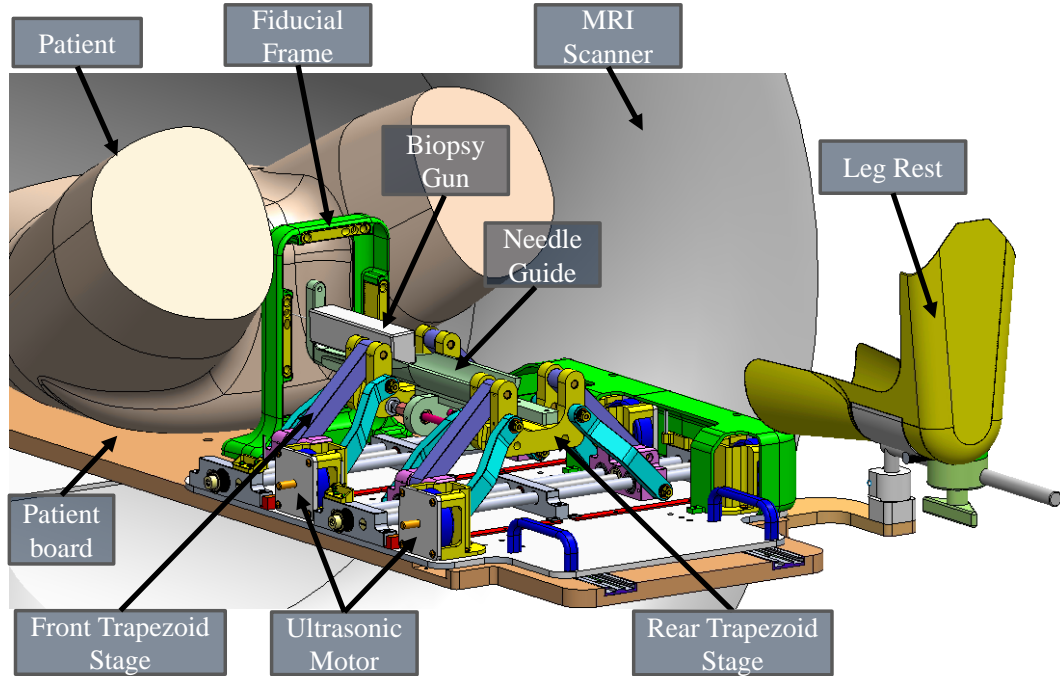
Figure 3.5: Annotated CAD model of the parallel manipulator for transperineal prostate intervention inside the MRI scanner bore. The patient lies in the supine position, the robotic manipulator is placed between the legs, and a biopsy gun targets the prostate through the perineum. Note that the leg rest and motor covers are hidden on the left side to visualize the internal structure of the manipulator.

3.4.2 Ultrasonic Piezoelectric Actuators

Piezoelectric actuators are driven by the controlled oscillation of ceramic crystals based on the piezoelectric effect. Magnetism utilized by typical electromagnetic motors and clearly contraindicated for use with MRI is therefore not required, making piezoelectric actuators a popular class of actuators in the MRI environment. In

terms of driving signal, piezoelectric actuators can be classified into two main categories: harmonic and non-harmonic. Harmonic actuators, such as Shinsei, Nanomotion (Nanomotion Ltd., Yokneam, Israel), and DTI (Discovery Technology International, Inc., Sarasota, FL) are driven by sinusoidal waveform on two channels at high frequency (typically $20kHz - 200kHz$). Non-harmonic actuators, such as PiezoLegs (PiezoMotor, Uppsala, Sweden), are generally driven by more complex shaped waveform on four channels at lower frequency ($750Hz - 3kHz$). The Shinsei harmonic ultrasonic actuator is adopted in this robotic system, due to its unique characteristics of high torque output, self-retention, and compactness.

The Shinsei actuator is comprised of a rotor and a stator. The stator is made of elastic body and piezoelectric ceramic unit. Two sinusoidal high frequency waveforms with $90°$ phase shift are applied to the piezoelectric ceramic unit to generate two standing waves on the elastic body, combining to generate a traveling wave that provides ultrasonic vibration to move the rotor and thus drive the motor. The two sinusoidal driving waveforms are generated by the corresponding Shinsei D6060 motor driver, which requires two channel input signals to control the driver output. A previously developed custom MRI robot controller [66] was adapted for this robotic system with appropriated modifications and improvements to interface with Shinsei motor drivers and control the robot.

3.4.3 MRI Robot Controller

The robot controller is developed as a team effort by the lab based on the previous system for neurosugery as desribed in Section 2.2.4. Significant efforts and design considerations have been made to improve the controller in the aspects of reliability and safety mechanism. The controller consists of two primary components within a shielded enclosure: 1) The backplane which includes an embedded controller that coordinates the motion control information from the planning level with the device level and 2) piezoelectric driver cards which generate control signals and perform closed loop motion control of the ultrasonic motors. The block diagram of the controller system is depicted in Fig. 3.6. The backplane exchanges control data with high level control PC via fiber optic Ethernet, and then forwards the data to each driver card via the serial peripheral interface (SPI) bus. The drivers process a proportional-integral-derivative (PID) control loop with data acquired from high level motion information and low level positioning encoder feedback to generate control commands through a direct digital synthesizer (DDS), based on a microcontroller (PIC32MX460F512L, Microchip Technology Inc., Chandler, AZ, USA) and field-programmable gate array (FPGA) (Cyclone EP2C8Q208C8, Altera Corp., San Jose, CA, USA). The output digital command is converted to analog signal through high-speed digital-to-analog converters (DACs) (DAC2904, Texas Instruments Inc., Dallas, TX, USA) and passes from linear amplifier out to the Shinsei motor driver through π filters. Optical encoders with differential drivers (EM1-1-1250-I and PC4, US Digital, Vancouver, WA,

USA) are used for position feedback, which has been proved to be compatible with MRI environment. The incorporation of precise DDS, high performance DACs, linear amplifiers, and π filters enables precise waveform shape control while precluding electrical noise. A further technique to reduce the electrical noise is enclosing all electronics including power regulation in an electromagnetic interference (EMI) shielded aluminum enclosure acting as a Faraday cage.

Safety and reliability are crucial design considerations for a robotic system used in a clinical environment. To this end, several safety mechanisms are introduced into the controller design. A non-metallic foot pedal that equipped with a fiberoptic photoelectric sensor is utilized by the clinician as an interlock for enabling motion only when engaged. Custom optical limit switches are installed on both ends of the four sliders to prevent the robot from reaching hard stops at the edge of the mechanism and damaging the robot. Stall detection based on the encoder feedback is used to monitor the robot motion status. In case of malfunction detected (i.e. encoder reading lost, jumped, or updated incorrectly), the stall detection mechanism automatically triggers a solid state relay that disconnects motor power and thus stops the robot motion. An emergency-stop switch installed in the power chain between the $24V$ regulator and the motor driver can directly shut down the motor power manually by the users, independent of any software components, in case of any urgent robot failure. LED indicators mounted on the upper surface of the controller box indicate the status of each piezoelectric driver board with varying color codes for the clinician.
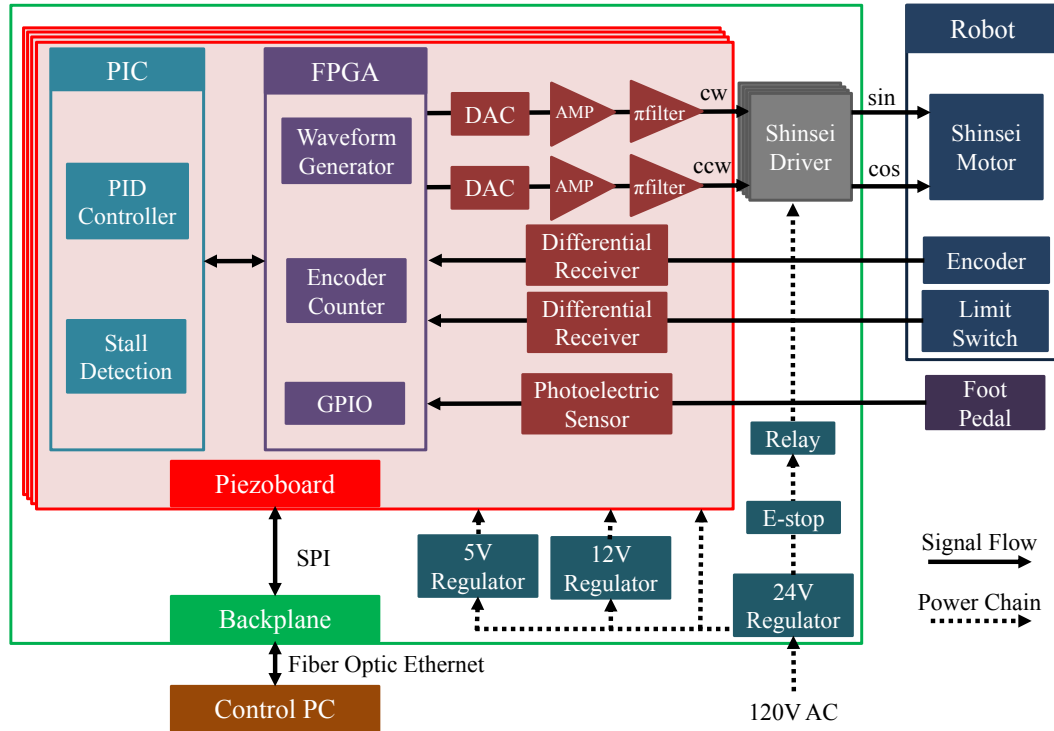
Figure 3.6: Block diagram depicting major components of the controller system. The controller is powered by the isolated, grounded $120V$ AC supply in the MR scanner room. All the power, control, and driver electronics are encased in an EMI shielded enclosure while communicating with the control PC through fiber optic Ethernet.

3.5 Navigation and Robot Control Software

3.5.1 Robot Registration and Surgical Navigation

3D Slicer and RadVision are used for surgical planning and navigation. The surgical plan is prepared using multi-parametric images, based on which targets are defined in suspected lesions on preoperative digital imaging and communications in

medicine (DICOM) format images which are pushed to the 3D Slicer workstation. In the beginning of the procedure, intraoperative images are acquired and deformable registration is performed using 3D Slicer to relate the surgical plan from preoperative images to intraoperative images. The registered surgical plan (i.e. targets in patient coordinates) are transferred to the navigation software RadVision over a network via OpenIGTLink and shown to the clinician for the visual confirmation.

Fiducial frame based registration is performed to register the robot to the patient coordinate system (i.e. MRI image space in right-anterior-superior (RAS) coordinates). Images of the fiducial frame are acquired and the DICOM images are pushed to RadVision, which then calculates the robot registration transform using line marker registration which has reported registration accuracy of $1.00 \pm 0.73mm$ and $1.41 \pm 1.06°$ [67]. The calculated registration transform is sent over a network via OpenIGTLink to the robot control application, where it is used to calculate the 6-DOF needle tip pose in patient coordinates through the transformation chain as shown in Fig. 3.7.

The patient anatomy may be visualized in RadVision in the perspective of axial, sagittal, coronal as well as combined 3D view for monitoring the needle track and confirming actual target positions. During the procedure, targets defined in patient coordinates at the time of surgical planning are selected in RadVision, and then sent to the robot control software described in Section 3.5.2 using the OpenIGTLink protocol. On receiving the desired target transform, the robot control application calculates

desired joint positions using robot registration transform and inverse kinematics. Desired joint positions are sent to the robot controller via the Bowler communication protocol [82] and the robot awaits foot pedal engagement by the clinician to initiate motion.
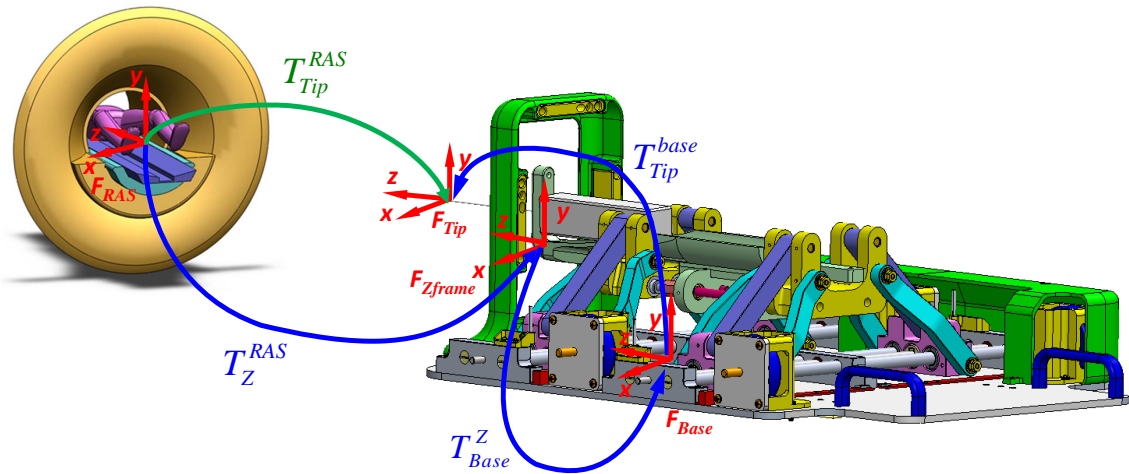
Figure 3.7: Kinematic transformation chain for registering the robotic system to the MR scanner coordinate system (RAS coordinates) based on imaging of the fiducial frame (Z-frame).

3.5.2 Robot Control Software

The robot control software is developed as a team effort by the lab with the capability to: define robot description using extensible markup language (XML), compute forward and inverse kinematics, generate coordinated motion commands, communicate via OpenIGTLink, and provide user interfaces for clinicians and system operating engineers. The robot control application ensures the clinical workflow by coordinated communication with robot controller and the navigation software. Two user inter-
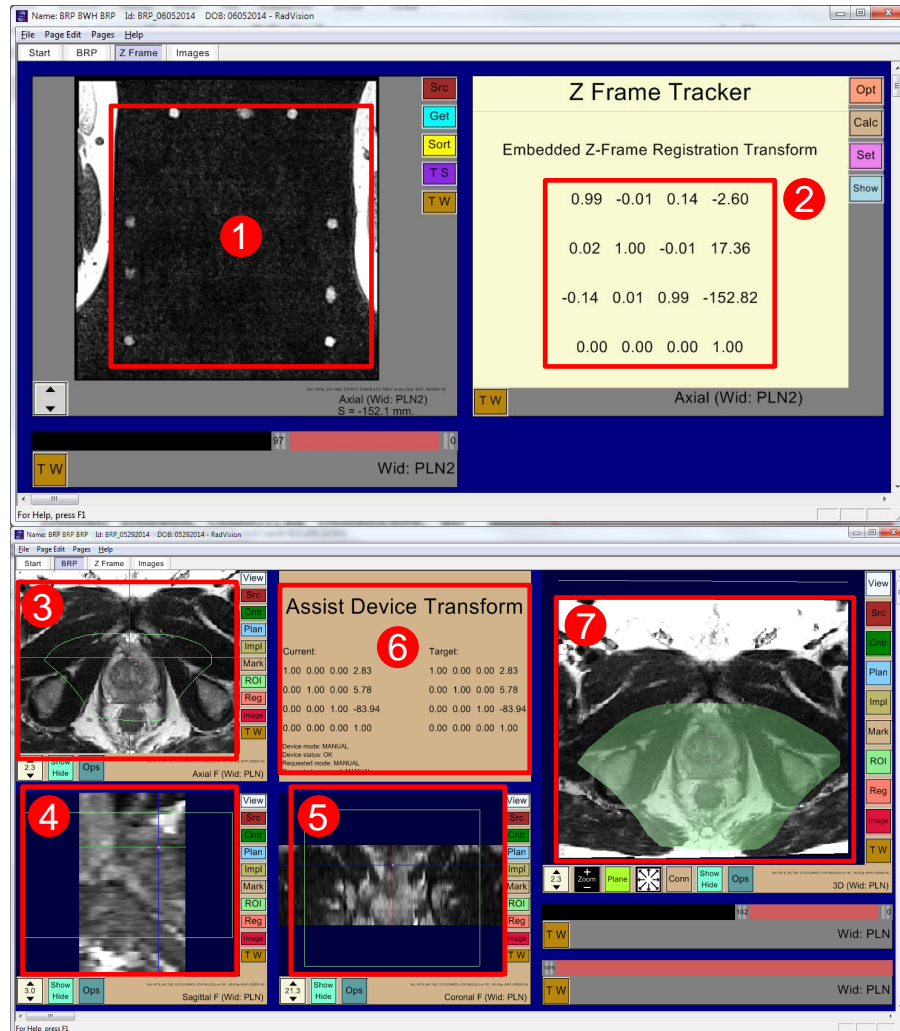
Figure 3.8: RadVision user interface showing (1) acquired MR images of fiducial frame, (2) calculated robot registration transform, (3) axial view, (4) sagittal view, (5) coronal view, (6) robot status, current robot pose, and desired target pose, and (7) 3D view with overlaid reachable robot workspace shown in light green. Also in all image views (3, 4, 5) light green boundary indicates reachable robot workspace.

faces, (1) CUI (clinician user interface): minimalistic interface for clinicians and (2) CMUI (control and maintenance user interface): restricted access low level interface for engineers to troubleshoot and maintain the robot controller are part of the robot control application as shown in Fig. 3.9 and Fig. 3.10, respectively.

Figure 3.9: Clinical robot control application (CUI) showing: (1) robot status information, (2) OpenIGTLink connection status with the navigation application, (3) current and target robot joint positions, (4) robot pose, registration transform and target transform and (5) control buttons for robot hardware test and initialization.

The CUI panel is displayed during the intervention as identified by #8 in Fig. 3.2 illustrates, and is composed of five modules: 1) The controller status module indicates the control mode, target range warning, hardware errors, and target status. 2) Communication status shows the server port number and connection status. 3) Robot pose reports the current and target position as well as the error for each slider in joint space. Needle insertion depth shows the required depth to be inserted manually to reach the target. Green and cyan blocks demonstrate the current and target position of each slider of mechanism in a graphical fashion to facilitate reporting the slider positions and checking the motion range. 4) Targeting panel reports the 6-DOF robot registration, current and target robot positions in RAS coordinate system. 5)
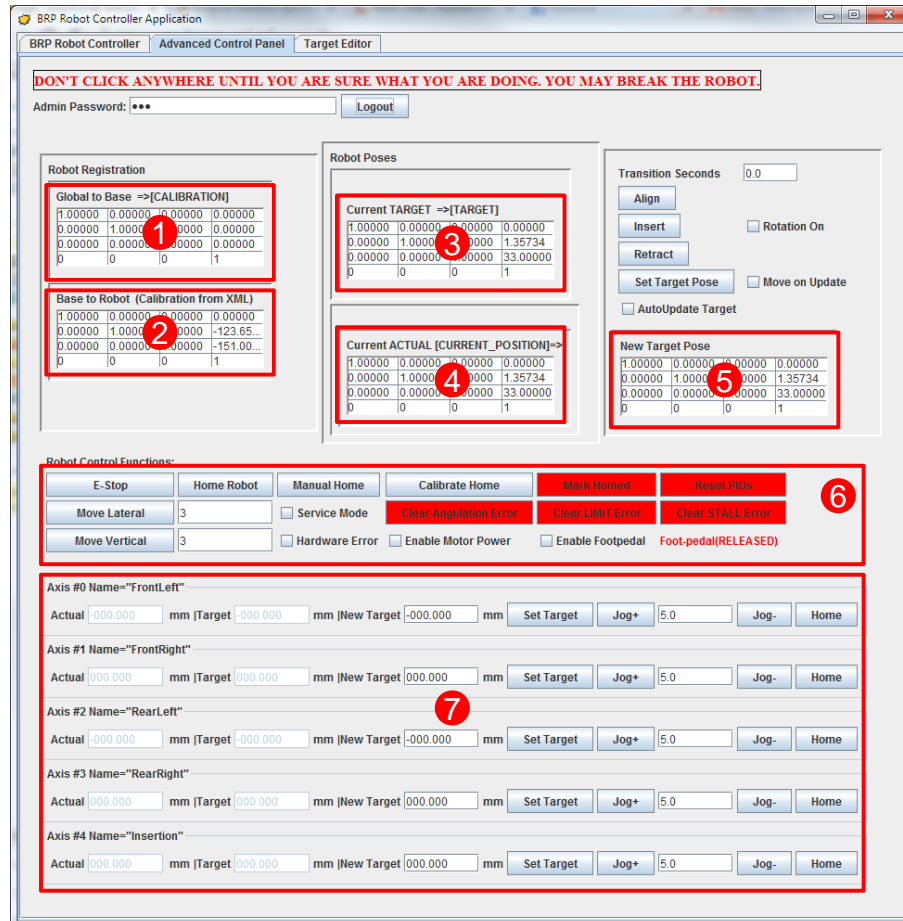
Figure 3.10: Restricted control and maintenance user interface (CMUI) showing: (1) robot registration transform, (2) fiducial frame to robot origin transform, (3) desired target pose, (4) current robot pose, (5) interface for manually entering target pose, (6) control buttons for robot maintenance, and (7) individual axis control interfaces.

The control command module is operable to send commands to robot controller to initialize, home, and stop the robot.

The primary functionality of the CMUI is to edit control command parameters that are used for system debugging purpose and are transparent to clinicians. The CMUI includes five primary modules: 1) Robot registration module shows the fiducial frame registration matrix and robot base offset matrix with respect to fiducial frame.

The registration matrices could be sent from RadVision via OpenIGTLink or typed manually. 2) Robot poses module reports the 6-DOF current target and current actual robot position in the image space. 3) Target operation module represents new target pose that could be set in RadVision via OpenIGTLink or typed manually. Additional buttons are intended for control of needle insertion in a future automatic version. 4) Robot control commands are editable to set and indicate robot status as well as initialize the robot to home position. 5) Joint control module is used to set control command for individual axis in joint space. The values could be generated automatically from homogenous transformation of the target matrix based on inverse kinematics or entered manually for each axis individually.

Both control panels are configurable for any desired robot mechanism. The robot is configured through the XML files containing axis names, PID controller parameters, motion range, scale factors from raw encoder ticks to engineering units and driving frequency ranges. Each node, i.e. joint axis, is editable, addable and removable according to specific robot mechanism. It is extensible and flexible to be applied to varying robotic systems with different mechanism configurations and control parameters.

3.6 Experiments and Results

In this study, we focus on the preclinical evaluation of the system with validation in phantom studies under MRI guidance and a clinical feasibility with a preliminary patient study.

3.6.1 Preclinical Evaluation: Phantom Studies under MRI Guidance

Phantom studies were performed under live MRI guidance to evaluate the targeting accuracy of the system inside a 3T MAGNETOM Verio scanner (Siemens AG, Erlangen, Germany), as shown in Fig. 3.11. The phantom used in this study is a mixture of gelatin and water with 22% concentration. An 18-gauge MRI-compatible biopsy needle was manually inserted into the phantom and imaged with diagnostic T2-weighted turbo spin echo (T2W-TSE) imaging protocol (imaging parameters are listed in Table 3.2: Needle Confirmation). The experiment was conducted in five independent sessions. For each session, new registration of the fiducial frame and initialization of the robot were performed, and five targets were randomly selected in RadVision covering typical focal region of prostate biopsy. Hence, 25 targets in total were collected to assess the system accuracy. The experimental setup was designed as a mockup of typical clinical procedures, which commonly include $1-5$ targets and require only one registration for each patient. The experiment was conducted with

the clinical team and strictly followed the proposed clinical workflow.
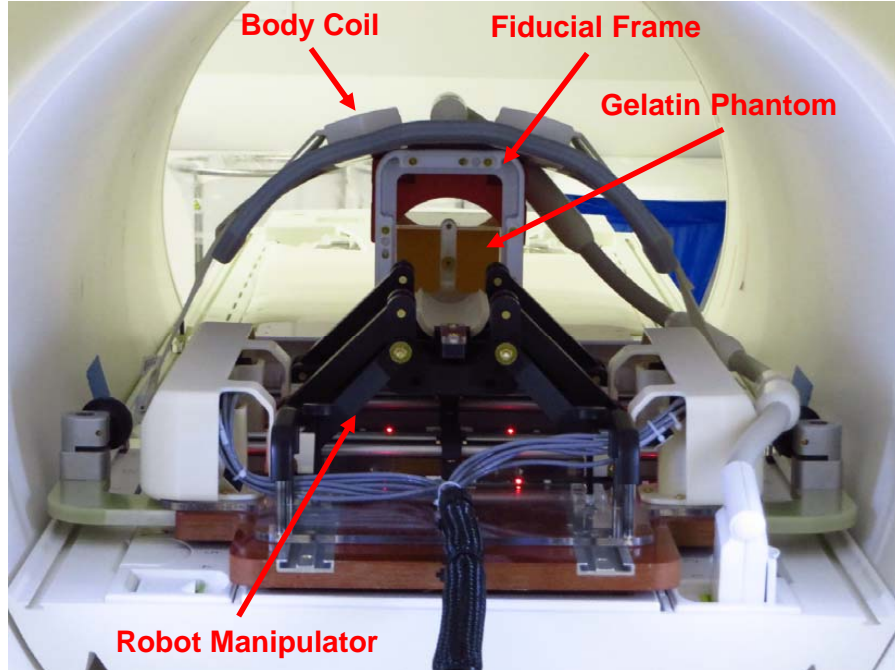
Figure 3.11: Experiment setup of preclincial evaluation with MRI phantom studies.

The desired target positions defined in RadVision were compared with actual needle tip positions (manually segmented from MRI volume images) to assess targeting accuracy. For the clinical procedures, the in-plane (RA-plane) error plays more significant role than the error along needle insertion axis (S-axis), since the insertion depth along S-axis is adjusted manually by the clinician to the desired depth via interactively updated imaging. Therefore, in-plane error is the metric assessed in this study, with results depicted in Fig. 3.12. The experiments results are summarized for each of the five session in Table 3.1, with RMS error in the R-axis (signed lateral), A-axis (signed vertical), and RA-plane (total magnitude) of $1.1mm$, $1.0mm$, and $1.5mm$, respectively.
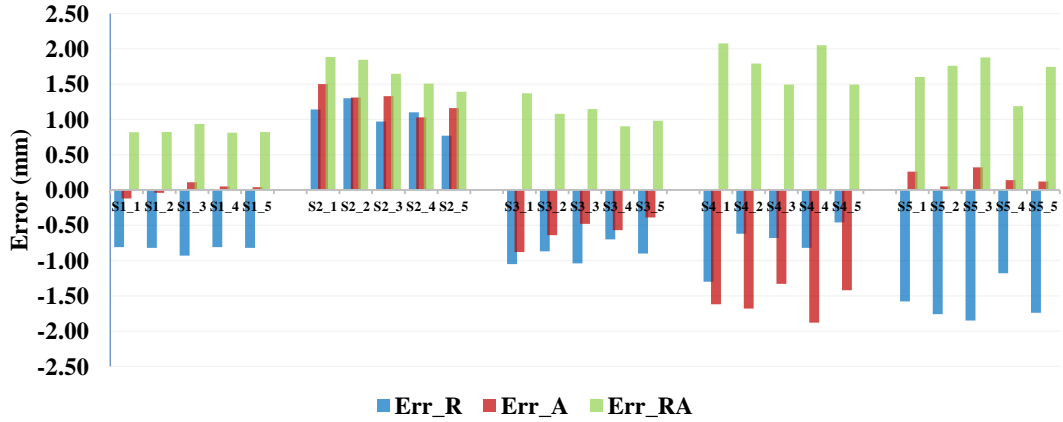
Figure 3.12: Plot of measured needle placement accuracy in each of the five trials in each of the five sessions. Data is shown with errors in the lateral R-L direction (*Err_R*), vertical A-P direction (*Err_A*), and total in-plane error magnitude (*Err_RA*).

Table 3.1: Experimental Results of MRI Phantom Study

Session	Error_R(mm)			Error_A(mm)			Error_RA(mm)		
#	Max	Min	RMS	Max	Min	RMS	Max	Min	RMS
1	-0.9	-0.8	0.8	-0.1	0.1	0.1	0.9	0.8	0.8
2	1.3	0.8	1.1	1.5	1.0	1.3	1.9	1.4	1.7
3	-1.1	-0.7	0.9	-0.9	-0.4	0.6	1.4	0.9	1.1
4	-1.3	-0.5	0.8	-1.9	-1.3	1.6	2.1	1.5	1.8
5	-1.9	-1.2	1.6	0.3	0.1	0.2	1.9	1.2	1.7
Total			1.1			1.0			1.5

3.6.2   Preliminary Clinical Patient Study

A clinical dry run was first performed with the clinical team on a volunteer to validate the proposed workflow and train the clinical team for using the robotic system. The key steps of patient setup are shown in Fig. 3.13

The viability of the approach is studied through an initial clinical procedure of prostate biopsy performed on a 60 year old male patient inside a 3T MAGNETOM Verio scanner with IRB approval and patient consent, abiding by the aforementioned
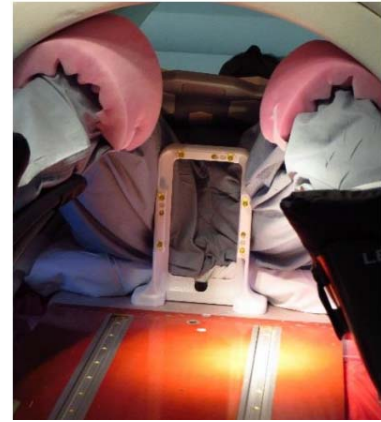
Figure 3.13: Clinical dry run setup showing: (a) positioning the patient in the scanner, (b) attaching the fiducial frame on the patient board, (c) covering the robot with sterile plastic drape and attaching the sterilized needle guide, (d) sliding the robot inside scanner and locking into place.

clinical workflow. Under IV conscious sedation, the patient was placed on the patient board in the semi-lithotomy position with legs rested on the support. Fig. 3.14 illustrates the system configuration for this patient study, and the imaging protocols used in this study are listed in Table 3.2. After patient positioning, the sterilized fiducial frame was attached on the patient board and registration was performed by acquiring MRI images with the *Localizer* protocol. After registration of the fiducial

frame, a new set of images of the prostate region were acquired using the *Intraoperative* protocol with Body Matrix and Spine Matrix coils (Siemens AG, Erlangen, Germany), and then registered to the preoperative planning images. Based on the registered images, two suspicious sites were selected in RadVision and sent to the controller for aligning the robot manipulator. Once the robot was aligned in place, the radiologist manually inserted an 18-gauge MRI-compatible core biopsy needle (Fully Automatic Biopsy Gun, InVivo Corporation) into the prostate gland through the robotically aligned needle guide. A confirmation image was used to validate the actual needle tip location with *Needle Confirmation* protocol. If the needle was not within the target lesion, adjustments (reinsertion and reorientation) can be performed manually by the clinician. Once the needle is confirmed to be in the target, a biopsy sample is manually procured from each of the two target sites. Fig. 3.15 shows the segmented actual needle trajectories overlaid on a 3D view showing an MRI image of the prostate gland and defined targets.

Table 3.2: Imaging Protocols for Patient Study

Imaging Protocol	Sequence	Flip Angle (deg)	TR (ms)	TE (ms)	Slice Thickness (mm)	Pixel Spacing (mm x mm)
Localizer	T2W-TSE	120	3000	111	2	0.70 x 0.70
Intraoperative	T2W-TSE	150	4800	100	3	0.50 x 0.50
Needle Confirmation	T2W-TSE	120	3000	106	3	0.75 x 0.75

Targeting accuracy of the biopsy was evaluated by computing the shortest distance from the desired target to the actual needle trajectory, and summarized in Table 3.3.

111

The accuracy of first insertion attempt was obtained solely by the needle guide, no adjustment was performed. The accuracy of the best insertion attempt was achieved by adjustment techniques. The clinician manually reinserts and reorients the biopsy gun until it was within the acceptable region to collect sample tissue, which represents a realistic accuracy for actual tissue sampling. The accuracy of the best insertion attempt for the two biopsies are $4.0mm$ and $3.7mm$, respectively. This preliminary measure of targeting accuracy is comparable to our previous study on template-based manual ($6.05mm$) and robotic ($5.42mm$) transperineal approach [77]. The total procedure time is $80min$, which is significantly reduced compared to our previous study on manual ($151.29 \pm 37.88min$) and robotic needle-guidance template ($141.67 \pm 19.47min$) [77].

Table 3.3: Experiment Results of Patient Study

Target	Target Position (mm)			First Attempt Error (mm)				Best Attempt Error (mm)			
	R	A	S	R	A	S	Total	R	A	S	Total
LCGApex	-13.2	8.5	15.6	-5.8	7.7	-1.1	9.7	-0.4	4.0	0.1	4.0
RPZMid	8.8	0.0	33.6	0.0	6.3	0.0	6.3	3.1	2.0	-0.3	3.7
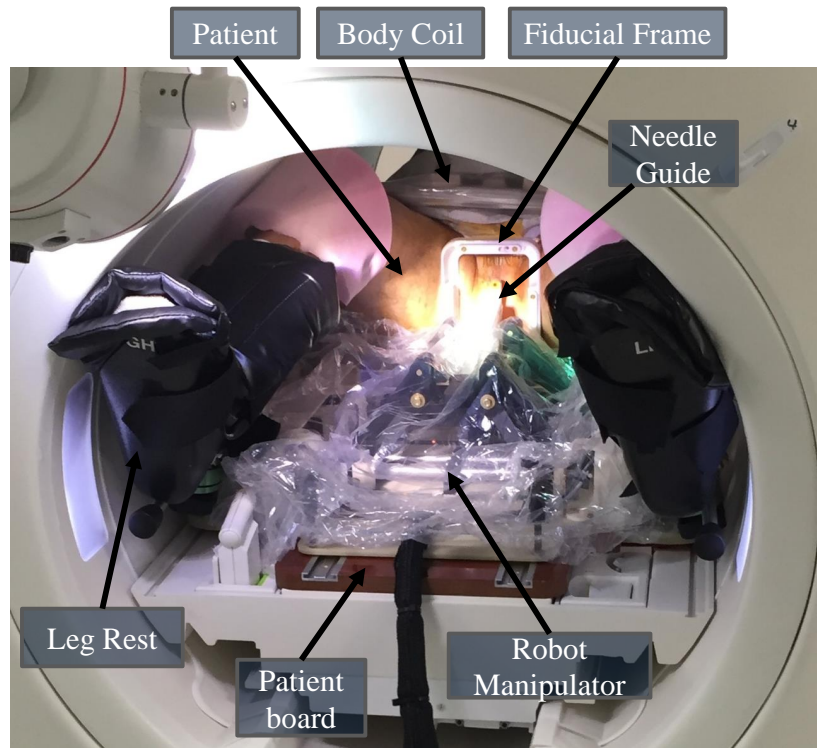
Figure 3.14: System configuration for the patient study. The patient lies in the supine position with legs supported by the leg rest on the patient board. The sterilized fiduical frame is fixed to the patient board between the patient's legs. The robot manipulator is covered by the sterile plastic drape, positioned on the patient board, and locked into place.

3.7 Autonomous Prostate Biopsy and Brachytherapy

Manual insertion is adopted in the clinical grade system for the sake of perceived safety and user acceptance. However, manual insertion is still time consuming and may lead to needle placement errors. A prototype system with full actuation is also developed in this study to perform autonomous prostate biopsy and brachytherapy.
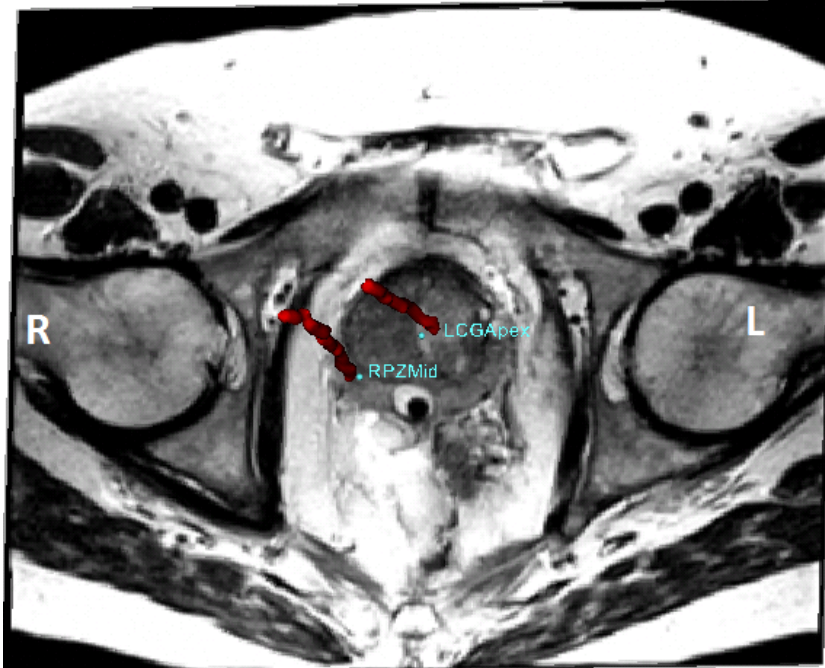
Figure 3.15: 3D view with an MR image of prostate gland showing desired targets (cyan dots) and actual needle trajectories (red lines, segmented from MRI volume images).

3.7.1 Fully Actuated Prostate Intervention Robot

The robot mechanism that was designed in our previous research efforts [66] is adopted in this study with modification and improvement on the needle driver to perform robot-assisted biopsy and brachytherapy with actuated insertion directly under the clinician's control. The 6-DOF robot consists of a 3-DOF Cartesian stage and a 3-DOF needle driver module, as shown in Fig. 3.16. The needle driver offers 1-DOF cannula translation, 1-DOF stylet translation, and 1-DOF cannula rotation that can be used to potentially reduce the needle insertion force and needle deflection. Coordinated motion can be implemented between the cannula translation and stylet translation under high precision motion control, to perform fully actuated biopsy

sampling and brachytherapy seed placement smoothly and precisely. The universal needle clamping mechanism is developed to fasten varying sizes of standard needles, from 25 Gauge (0.5144 mm) to 16 Gauge (1.651 mm), by using the corresponding collet. The design allows a variety of needles to be mounted on the needle driver by choosing specific needle adaptors, including those for various biopsy needles, brachytherapy needles and other needles and cannulas.

To register the robot to the RAS (Right, Anterior, Superior) patient coordinate system in the image space, a fiducial frame is firmly attached to the base of the robot as shown in Fig. 3.16. The fiducial frame is composed of seven tubes filled with MR-visible, high contrast fluid (Beekley, Bristol, CT), and configured in a set of "Z" shapes in each of the three orthogonal planes [57]. Based on imaging the fiducial frame, the 6-DOF position and orientation of the robot can be localized with respect to the RAS patient coordinates.
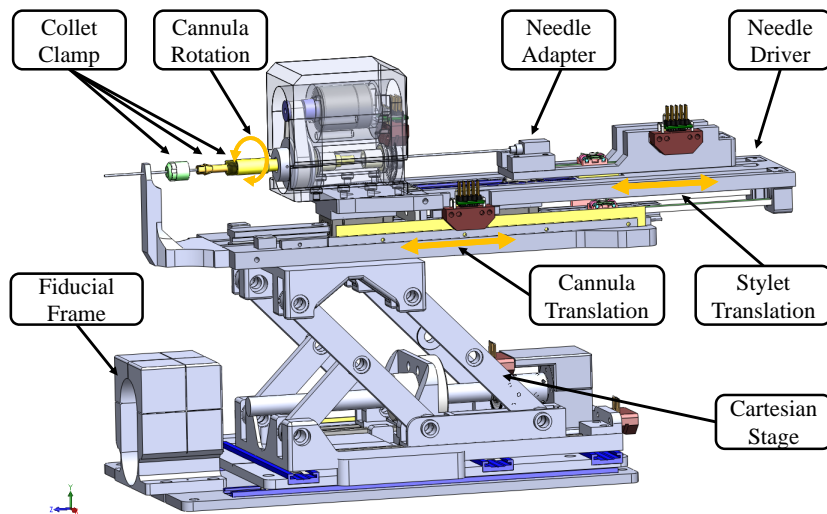
Figure 3.16: 3D CAD model of the prostate interventional robot showing Cartesian stage, needle driver, and fiducial frame.

3.7.2 Workflow

The workflow of the system mimics that of traditional template-based transperineal prostate interventions guided by transrectal ultrasound (TRUS), as shown in Fig. 3.17. By utilizing a modular robot design, the system could implement biopsy, brachytherapy and most other standard needle-based prostate interventions with only minor modifications of the workflow. The unified workflow consists of five major steps:

1. Initialization: Initialize the hardware and software of system. Initialize all the robot joints and move the robot to the defined home position.

2. Registration: Capture a small MR image volume of the fiducial frame. Perform fiducial frame registration, using multi-image registration method.

3. Planning: Capture MR images of the prostate and define targets in the MR images via navigation software. Transmit the targets to robot control software over OpenIGTLink for processing inverse kinematics and solving joint space commands.

4. Targeting: Move the robot to the desired target position and perform corresponding clinical procedure under live image guidance. The targeting procedure could be modified to implement various interventions according to specific clinical procedures, including image-guided biopsy, brachytherapy, and others requiring straight needle insertion.

5. Verification: Visualize the reported actual needle position and interactively updated images in the navigation software for verification.
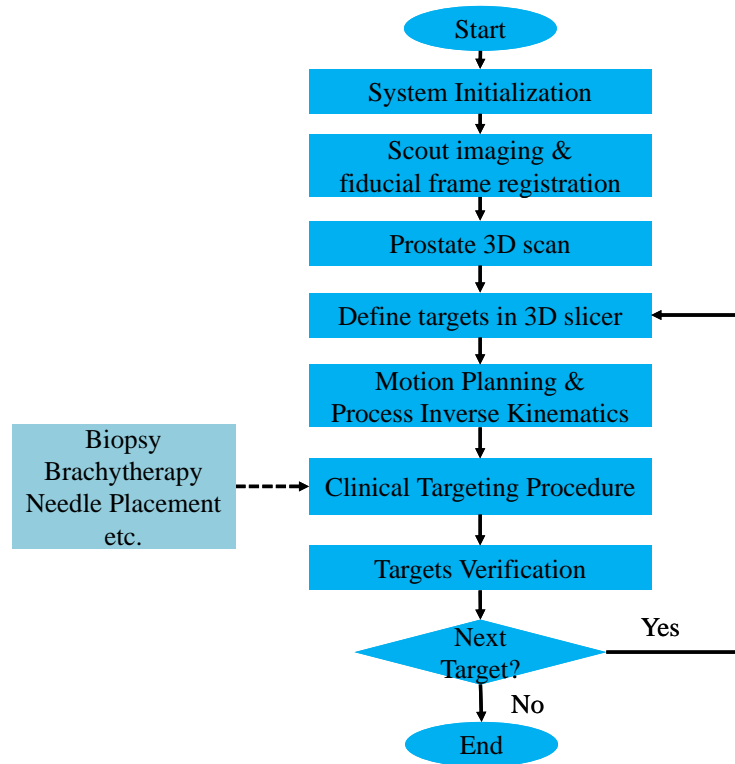
Figure 3.17: Unified workflow of MRI-guided robot-assisted prostate interventions.

3.7.3 Experiments and Results

To evaluate the feasibility of the system workflow and the flexibility of the modular design approach, phantom experiments of automated prostate biopsy and brachytherapy were performed under MRI-guidance. The experimental setup utilized in a 3T MRI scanner is shown in Fig. 3.18. Gelatin phantoms used in these tests are firmer than the regular tissue to avoid the gelatin to deflect during needle insertion.
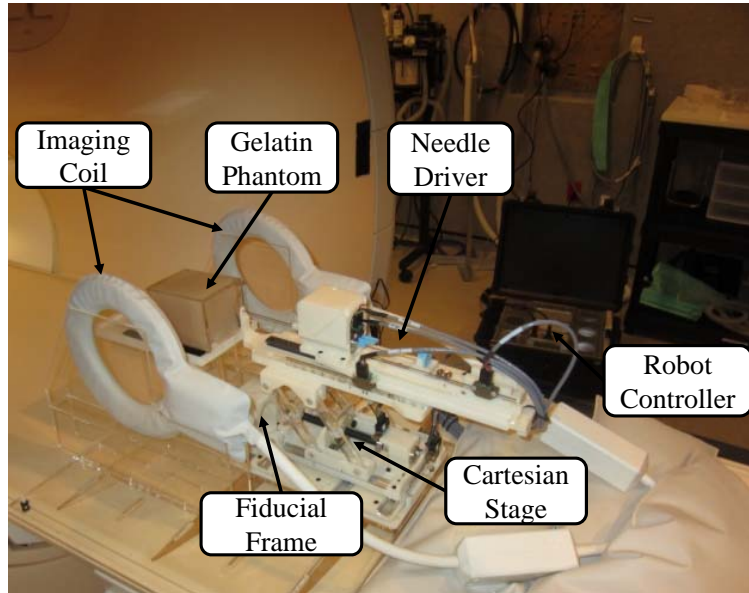
Figure 3.18: The prostate interventional robot at the entrance of the bore to a 3T MRI scanner showing the phantom experimental setup.

3.7.3.1 Autonomous Biopsy

To perform autonomous biopsy, a precise coordinated motion between the outer cannula and inner stylet is implemented in our motion control system. The motion sequence for executing a biopsy is shown in Fig. 3.19, and the needle driver with robotic biopsy gun is shown in Fig. 3.20. According to this procedure, we can specify the clinical targeting procedure in the unified workflow as depicted in Section 3.7.2:

1. Align the robot to the plane of the entry point.

2. Insert the cannula to the depth of L before the target position, guaranteeing the sample at the center of notch. (L equals to the distance from the tip of stylet to the notch center.)

3. Sample biopsy under automatic procedure. Insert stylet distance of 2L, making

the notch center at target sample position. Perform coordinated motion to insert cannula and retract stylet with the same length 2L and under the same speed to capture the sample inside the needle.

4. Retract needle containing the biopsy core to home position.
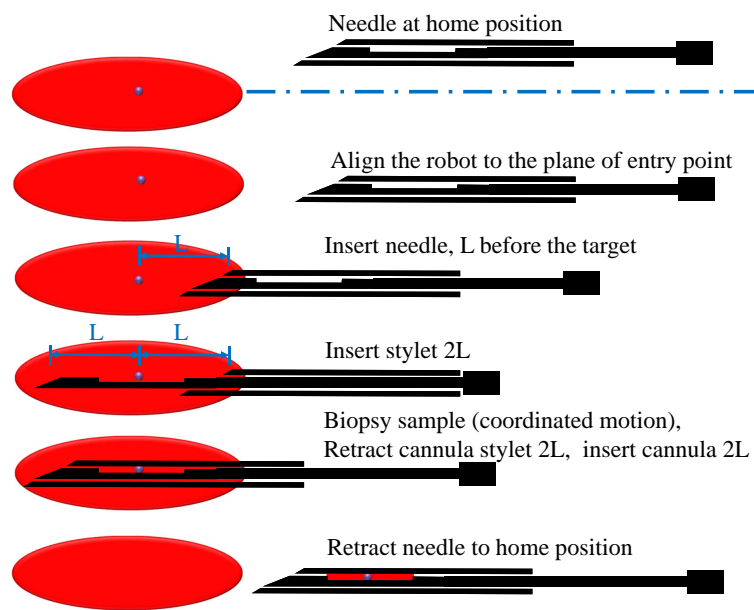
Figure 3.19: The clinical procedure for executing automated biopsy.

The feasibility of autonomous biopsy is demonstrated with a phantom study. Beans with an approximate diameter of 9 mm, which is similar to the size of a tumor to be targeted, were embedded in a gelatin phantom to serve as biopsy targets. An 18G MRI biopsy needle is placed in the gelatin phantom by the robot and imaged with real-time imaging protocol during the intervention.
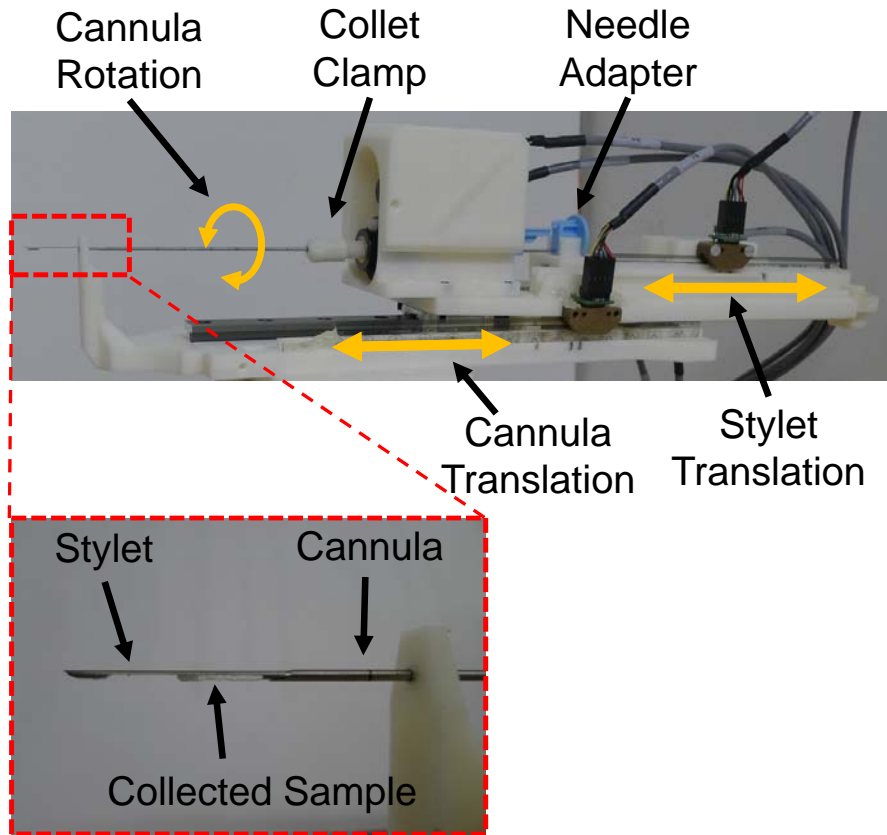
Figure 3.20: The needle driver loaded with robotic biopsy gun. Inset, close-up view of the outer cannula and inner stylet with collected sample.

3.7.3.2 Autonomous Brachytherapy

With equivalent approach as autonomous biopsy, a motion system is designed to implement the coordinated motion sequence for autonomous brachytherapy. The procedure for executing brachytherapy is shown in Fig. 3.22 and can be specified the in the unified workflow:

1. Retract stylet joint to depth L, and load the seeds and spacers to the brachytherapy needle according to the treatment plan. (L equals to the sum of the length of the seeds and the spacers). Alternatively, pre-loaded needles may be loaded
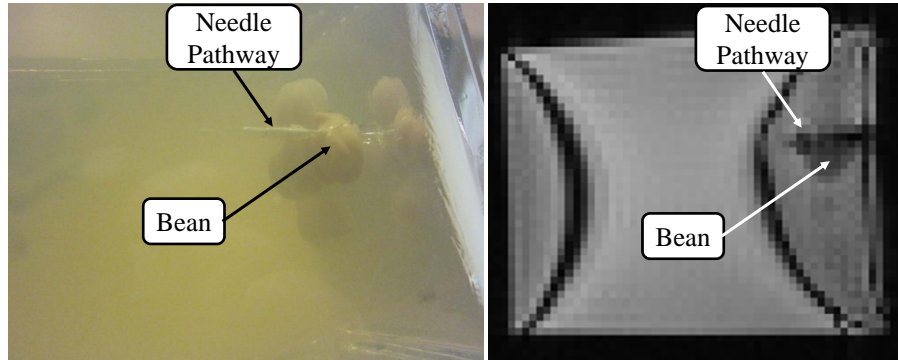
Figure 3.21: (Left) Gelatin phantom with biopsy targets and (right) real-time MRI image of the target in the gelatin phantom showing the needle in the bean.

into the needle driver.

2. Align the robot such that the needle axis is in line with the planned entry point.

3. Insert the cannula along the needle axis to the target position.

4. Deliver seeds under automatically coordinated motion, retracting cannula and inserting stylet with the same length L and under the same speed.

5. Retract needle to home position.

To evaluate capabilities for brachytherapy, a 3×3 pattern of needles with three seeds per needles was applied with the robot. Custom made brass seeds and plastic spacers are employed to mimic the radioactive seeds, with length of 5mm for both seed and spacer. The seeds and spacers could be distinguished under MRI images with their different imaging properties, i.e. introducing different artifacts. An 18G MRI brachytherapy needle is placed in the gelatin phantom and imaged with T2-weighted fast spin echo imaging protocol (T2W TSE).
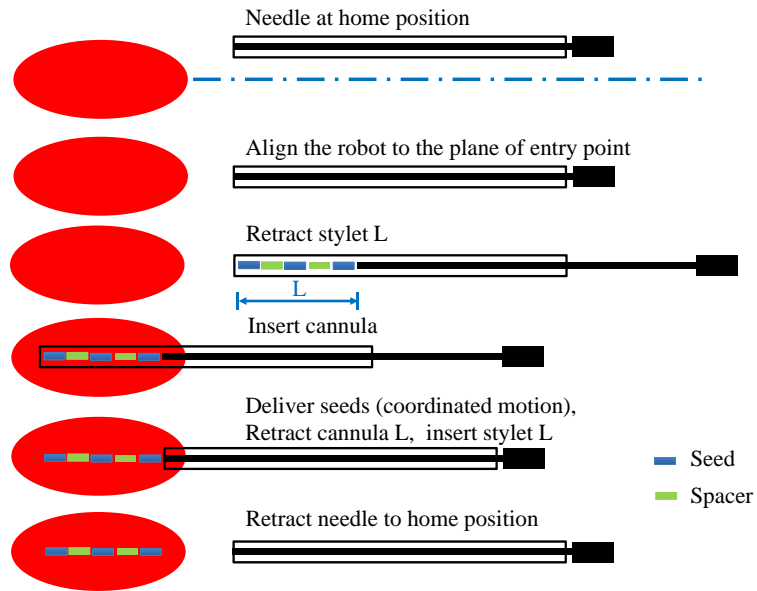
Figure 3.22: The clinical procedure for executing automated brachytherapy seed delivery.

Both MRI and CT images were utilized to analyze the experimental results. MRI image was used to demonstrate feasibility and qualitatively to illustrate the pattern of the seeds and spacers, as shown in Fig. 3.23. Due to its very high resolution, CT images were used for quantitative analysis of the seed placement distribution. The proposed seeds distribution pattern was compared with the actual pattern (as measured using the segmented high resolution CT scan of the phantom with implanted seeds, as shown in Fig. 3.23). A point cloud registration between the plan and the segmented CT was used to determine the accuracy of the seeds placement pattern; absolute location with respect to the scanner was not assessed. The experimental results demonstrate submillimeter accuracy of the seed distribution, with an RMS error of approximately 0.98mm and a standard deviation of approximately 0.37mm. The error in seed placement may be due to needle deflection, considering the bevel
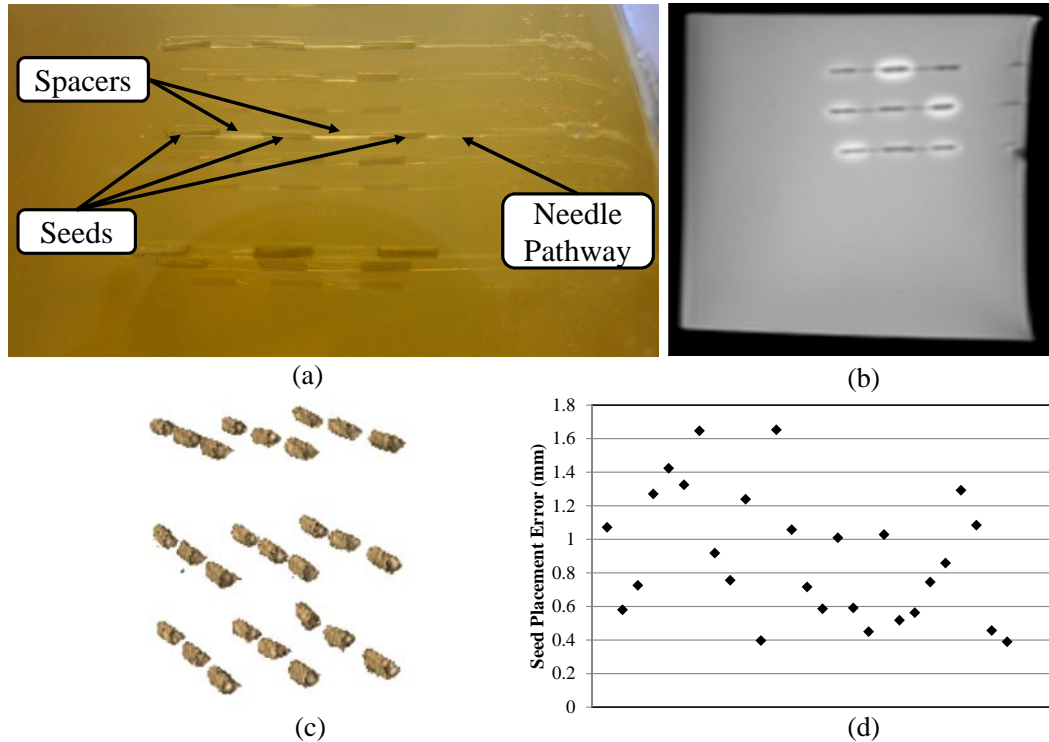
Figure 3.23: (a) Gelatin phantom showing the 3 x 3 x 3 robotically placed brachyther-apy seeds, (b) a representative MRI showing one plane of seeds, and (c) segmented 3D CT image of the target gelatin phantom used for accuracy assessment. (d) plot of the seeds placement error.

tip of the brachytherapy needle, which could be reduced by rotating the cannula to reduce the insertion force. The custom made seeds and spacers are not exactly the same length, that could also introduce some errors.

3.8   Discussion and Conclusion

In this chapter, we report the development of a fully integrated robotic system for MRI-guided transperineal prostate biopsy, which has been approved by IRB for clinical trials. The clinically oriented robotic system described herein is developed

based on a modular approach, with the modules connected through a network. A major merit of network based modular design approach is that each module can be developed and tested individually, making it readily configured for supporting a specific clinical workflow and extensible to various clinical applications. Safety is a crucial requirement for a clinical system; therefore, even in the case of robot failure, safety mechanisms are considered during the design phases, including motion range limit switches, user controlled foot pedal interlock, independent emergency stop power switch, as well as controller status monitoring with hardware and software. Sterility is a unique and critical requirement for clinical devices; for this reason the robot manipulator is designed with non-sterilizable and sterilizable components. Non-sterilizable components are covered by a standard disposable pre-sterilized drape and sterilizable components are prepared in a kit and sterilized prior to the procedure.

In our previous study on the mechanism design [65], the system targeting repeatability and accuracy were assessed in free space, demonstrating the errors are less than $1mm$. Moreover, compatibility with the MRI environment was evaluated in a 3T MRI scanner with varying robot configurations, showing SNR reduction of less than 16% when controller is powered on. In this work, preclinical phantom studies were performed to evaluate the system targeting accuracy and to rehearse the clinical workflow. The in-plane errors were assessed, demonstrating a RMS error of $1.5mm$ and maximum error of $2.1mm$. The placement accuracy achieved herein is comparable to other preclinical studies of MRI-guided robotic systems; Stoianovici et al.

reported an MRI-safe robot for endorectal prostate biopsy with in-vitro targeting accuracy of $2.1mm$ [7] and Krieger et al. presented in-plane target accuracy of $2.4mm$ was achieved by an actuated transrectal prostate robot [14]. The targeting accuracy of the proposed system reflects the overall accuracy of the system, which could be classified as registration error (fiducial frame registration and alignment), robot manipulator error (robot mechanism backlash, motion control precision), imager error (imaging resolution), and un-modeled error (needle deflection as inserting into the phantom). Based on the systematic error depicted in Fig. 3.12 for each session, the errors in R-axis (Err_R) and A-axis (Err_A) are both in same direction. It appears that the dominant error source is most likely registration error. To separate robot accuracy from registration accuracy, the mean error is subtracted for each session, resulting in the in-plane RMS error of $0.2mm$.

A preliminary clinical study was described to demonstrate the viability of clinical use of this robotic system. The patient study was performed following the IRB approved clinical workflow. The clinical procedure was performed successfully in about $80min$, which is a significant reduction in procedure time as compared to our previous study on manual and robotic needle-guidance template [77]. Two suspicious sites were targeted and one biopsy tissue core was procured from each target site. The maximum targeting error was $4.0mm$, which is acceptable to target a clinically significant tumor foci with a sphere of $5mm$ radius [83, 84]. More extensive clinical cases are currently ongoing at BWH, and further thorough accuracy analysis in the

aspects of organ motion and needle deflection will be considered in future studies. Until the date of defense, 18 clinical patient studies have been performed successfully.

Manual needle insertion and tissue biopsy sampling along a robotically aligned axis was adopted in the clinical version of the robotic system as an initial goal primarily due to safety and clinical acceptability considerations. However, manual operation inside the tightly constrained scanner bore is still ergonomically awkward and time consuming. A prototype version of fully actuated approach is further developed. Phantom experiments validate the capability and flexibility of the system to execute automated prostate biopsy and brachytherapy with only minor modification of the typical clinical workflow. The preliminary results are satisfactory with an RMS seeds placement accuracy of approximately 0.98mm. Homogeneous gelatin phantom is used as a test medium for this assessment. Deflection of the needle may present and result in needle placement errors in the inhomogenouse tissue, as observed in the clinical trials. Needle steering techniques combined with image-based position feedback could potentially compensate the placement errors by correcting the needle path, as discussed in Section 4. The proposed architecture overcomes many of the limitations of manual insertion (fully manual or robot-assisted alignment) by allowing the clinician to control the robot from beside the patient but outside the tightly constrained bore. The MRI-guided automated needle placement robotic system provides some significant advantages over manual approaches, including 1) improved work flow: the work flow is more straight forward and coherent, with the robot assistance and high

126

resolution image guidance, 2) increased position accuracy, the individual robot joint accuracy could be as high as $30\mu m$ [85], and 3) reduced time consumption, especially for multiple needle insertions: biopsy and brachytherapy procedures are executed automatically, under coordinated motion.

Chapter 4

MRI-Guided Steerable Needle Interventions

This chapter discusses the modeling and control of two methods of steerable needle intervention, namely asymmetric tip steerable needle and concentric-tube continuum cannula. Firstly, this chapter proposes a novel asymmetric tip needle steering method based on the nonholonomic kinematic model, named Gaussian-based ContinUous Rotation and Variable-curvature (CURV) steering model, which enables variable curvature of the needle trajectory with independent control of needle rotation and insertion. As it is inserted into the tissue, the needle rotates continuously with Gaussian-based angle-dependent velocity motion profile. Continuous rotation with smooth transition could attenuate the static frictional effects, and variable curvature improves the steering capability. Decoupling control of insertion motion from the curvature con-

trol readily enables active control of the needle path for particular tasks that precise coordination of insertion and rotation is hard to achieve, such as shared autonomy (autonomously controlled rotation with manual insertion). Image-guided closed-loop control of the CURV steering model is presented using continuously acquired intra-operative MR images as position feedback, which could compensate modeling error and increase the positioning accuracy. Experimental validation of the CURV steering model is performed with phantom studies in 2D with camera images and in 3D with CT images, demonstrating root mean square (RMS) error of the trajectory accuracy better than 1.5 mm. Closed-loop control of the steering model is assessed with MRI phantom study, indicating 0.75 mm RMS error.

In the second part of the chapter, it presents the design, modeling and experimental evaluation of a magnetic resonance imaging (MRI)-compatible concentric tube contin-uum robotic system. This system enables MRI-guided deployment of a precurved and steerable concentric tube continuum mechanism, and is suitable for clinical applica-tions where a curved trajectory is needed. This compact 6 degree-of-freedom (DOF) robotic system is piezoelectrically-actuated, and allows simultaneous robot motion and imaging with no visually observable image artifact. The targeting accuracy is evaluated with optical tracking system and gelatin phantom under live MRI-guidance with Root Mean Square (RMS) errors of 1.94 mm and 2.17 mm respectively. Further-more, we demonstrate that the robot has kinematic redundancy to reach the same target through different paths. This was evaluated in both free space and MRI-guided

gelatin phantom trails, with RMS errors of 0.48 mm and 0.59 mm respectively. As the first of its kind, MRI-guided targeted concentric tube needle placements with ex vivo porcine liver are demonstrated with 4.64 mm RMS error through closed-loop control of the piezoelectrically-actuated robot.

The first part of this work is performed in collaboration with Sarthak Misra, Pedro Moreira, and Tim van Katwijk at University of Twente. The second part of this work is performed in collaboration with Robert J. Webster III and D. Caleb Rucker at Vanderbilt University.

4.1 Introduction

Asymmetric Tip Steerable Needle

The kinematics of bevel-tip needle steering can be modeled as a nonholonomic system with motion similar to that of a unicycle or bicycle with two control inputs (i.e. needle rotation and insertion) [26], and has been widely investigated in the control of steerable needle [86]. There are two primary approaches based on this nonholonomic model that have been reported for active needle steering. One steering algorithm is based on alternating between discrete maximum curvatures (i.e. sequential curve-left and curve-right motion) [16, 87]. The other approach attempts to steer with intermediate curvatures. To achieve the variable curvature, a method that incorporating duty-cycled spinning during needle insertion is proposed [17, 88], and utilized for s-

teering the flexible needle [89–91]. A variant of duty-cycled method with bidirectional rotation is proposed to prevent cable wind-up issue for use of special instrumentation like force sensors [92]. Fig. 4.1 illustrates the concept of a bevel tip needle steering approach using duty-cycle spinning.
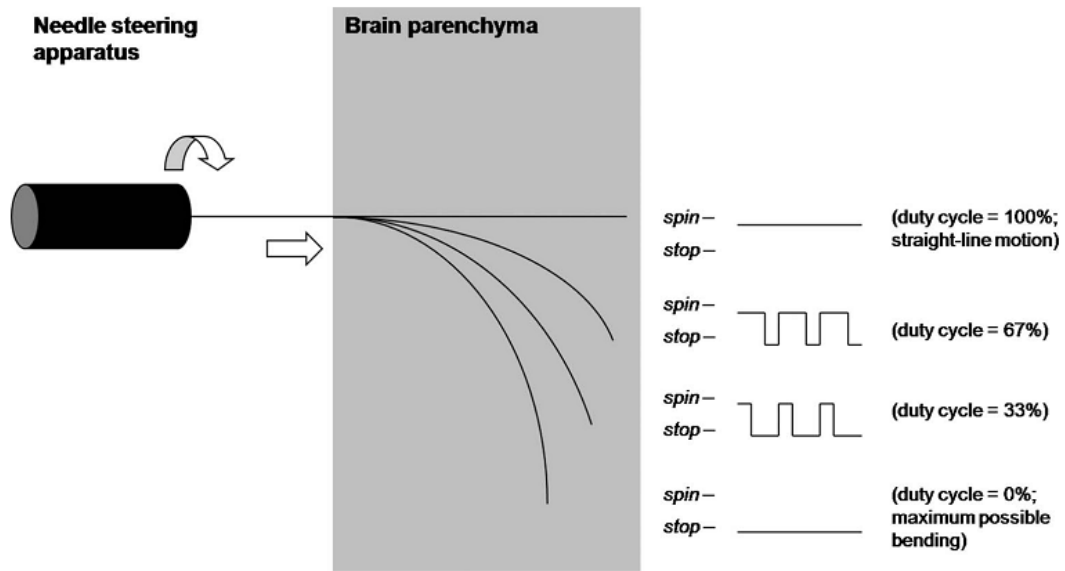
Figure 4.1: A conceptual drawing of a bevel-tipped needle being inserted into tissue using duty-cycled spinning [17]. ©2010 by the Congress of Neurological Surgeons.

Among the existing needle steering methods, controlling variable curvatures (e.g. duty-cycled approach) provides more benefits over discrete maximum curvatures in terms of controllability, since the possible curvatures are not limited to the maximum values. However, duty-cycled approach is frustrated with sharp step transition which may cause severe strain on the actuation system, and introduce electro-magnetic noise during imaging procedures such as MRI. At the rotation-off phase, i.e. pure insertion, static friction that presents between the needle and tissue could lead to needle placement errors. Moreover, duty-cycled approach requires the needle rotation to be

131

highly coupled with insertion and a relatively large duty-cycling window. Although highly coupled motion of rotation and insertion is often feasible for fully automatic insertions, it is not an optimal solution for control of the needle path in practice when variable insertion speed are applied, such as manual or teleoperated insertion, which are commonly used in current clinical procedures for the sake of safety.

Concentric Tube Continuum Cannula

Concentric tube continuum cannula, also known as active cannula, are consisted of telescoping concentric pre-curved elastic tubes and actuated at the base by the axial translation and rotation of each component tube, as shown in Fig. 4.2. The mechanics model of concentric tube continuum cannula is proposed by Webster et. al. [93]. The bending actuation is derived from elastic tube interaction in the backbone itself, and not from tendon wires or other external mechanism, allowing high dexterity and compact dimension design. Concentric tube continuum cannula is able to transverse narrow and winding environments and suitable for medical procedures where narrow opening to access air-filled cavities are required. In this study, we design and evaluate a robotic system that integrates our developed framework for MR-conditional piezoelectric actuation with concentric tube continuum mechanism, enabling the MRI-guided concentric tube continuum deployment as a steerable needle.

The primary contributions of this chapter are: 1) theoretical modeling of a novel Gaussian-based CURV steering approach, enabling effective variable curvature control with continuous smooth rotation and independent insertion control; 2) closed-loop
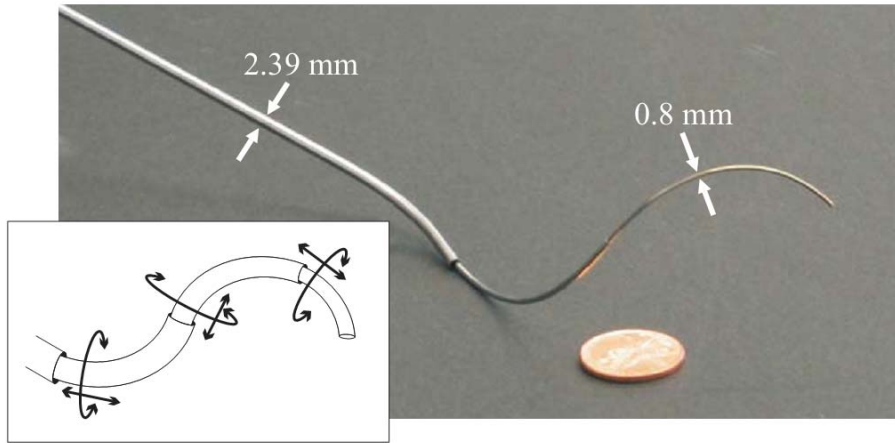
Figure 4.2: A prototype active cannula made of superelastic Nitinol tubes. The inset line drawing indicates the active cannula's degrees of freedom [94]. ©Robert J. Webster, III 2007.

control of CURV steering under continuous intraoperative MRI-guidance, correcting the modeling error on-line and improving position accuracy; 3) experimental verification and validation of CURV steering model, and closed-loop control approach with phantom studies; 4) design and evaluation of an MRI-guided concentric tube continuum robotic system, combining MR-conditional piezoelectric actuation with a concentric tube robot deployed as a steerable needle.

4.2 Asymmetric Tip Steerable Needle

4.2.1 Nonholonomic Kinematic Model

The asymmetric-tip needle is able to provide 6-D positioning with only 2-DOF control inputs (needle insertion and rotation), and therefore can be modeled as a

nonholonomic system. A variant of the standard bicycle model with fixed front wheel angle has been proved to be controllable in [95], and is utilized to establish the kinematic model for the asymmetric-tip needle steering [26]. The bicycle model is configured with fixed front wheel angle ϕ, constant wheel base length l_1 and needle tip location l_2 along the bicycle, which together specify the curvature κ of the needle path. Insertion speed u_1 and rotation speed u_2 are two control inputs provided by the control system. The configuration of bicycle model is shown in Fig. 4.3.
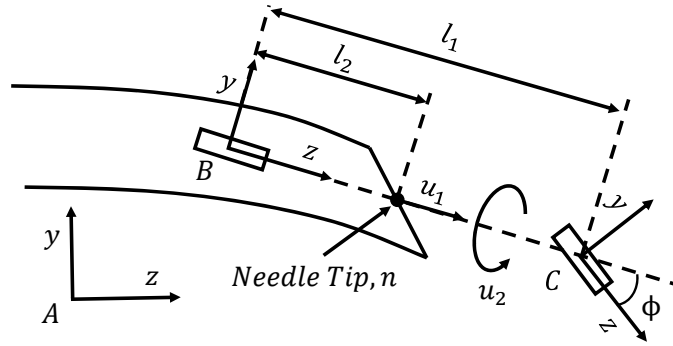
Figure 4.3: Configuration of nonholonomic bicycle model of a bevel-tip needle during steering, showing the world frame A, the back and front wheels at frames B and C respectively (Redrawn based on [26]).

As presented in [26], the discretized bicycle model can be depicted as:

$$g_{ab}(k+1) = g_{ab}(k)e^{(u_1(k)\widehat{V_1}+u_2(k)\widehat{V_2})T}$$

$$n(k) = R_{ab}(k)l_2e_3 + p_{ab}(k)$$

(4.1)

where, g_{ab} is the transformation between the world frame A and the rear frame B, n is the needle tip frame, $\widehat{V_1}$ corresponds to pure needle insertion, and $\widehat{V_2}$ corresponds

to pure needle shaft rotation. In this study, the rotation angle is defined in the way that needle tip pointing down along y-axis is $0°$, and rotates counter-clockwise about z-axis. The kinematic model is limited to following a fixed curvature given a 1-DOF insertion.

4.2.2 Gaussian-based Continuous Rotation and Variable Curvature Steering Model
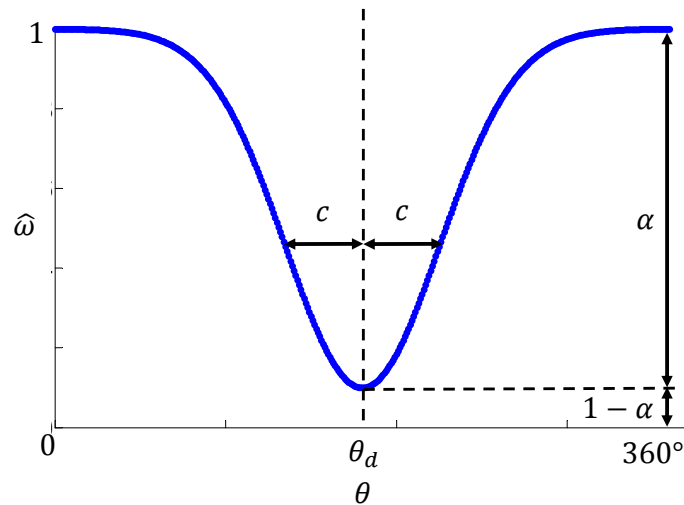
Figure 4.4: Normalized needle rotation velocity profile with respect to rotation angle for the CURV steering model. Shown for a representative single rotation of the needle, where the minimum rotation speed is at the desired rotation angle θ_d corresponding to the steering direction.

Based on the kinematic model, the desired needle tip position can be achieved with the constant needle insertion and rotation; however, the needle curvature is fixed. In this study, a novel model that enables variable curvature control with two control inputs is proposed. The needle insertion speed u_1 is an independent control input

135

which could be performed in a manual, teleoperated or automatic fashion. The needle rotates continuously about its primary axis and the rotation speed is determined as a function of the current rotation angle θ and desired rotation angle θ_d (an angle corresponding to the desired motion direction). In the proposed implementation, the Gaussian distribution, a common continunous distribution, is utilized to define the normalized rotation velocity $\hat{\omega}$ as

$$\hat{\omega}(\theta, \theta_d) = 1 - \alpha e^{-\frac{(\theta - \theta_d)^2}{2c^2}} \tag{4.2}$$

where, α is the steering effort which determines the minimum speed value of the motion profile, c is the Gaussian width which determines the range of the low speed region in the motion profile. As shown in Fig. 4.4, the rotation speed decreases from the maximum value to the minimum value as the needle rotation approaches the desired rotation angle θ_d. During the region of slower rotation the needle tends to bend more in the direction of θ_d, while during the faster rotation regions the needle tends to follow a straighter trajectory. The rotation motion profile is adjustable with steering effort α and Gaussian width c. The instantaneous rotation speed u_2 can be calculated via multiplying the normalized speed by the maximum desired rotation speed of the needle ω_{max}, which may be limited by the mechanical or electronic control system, and thus can be written as:

$$\dot{\theta}(\theta) = u_2 = \omega_{max}\hat{\omega} \tag{4.3}$$

This CURV steering model can be implemented on a control system with constant period T in discrete form. The insertion depth along the primary axis of needle and rotation angle can then be expressed as:

$$l(t + 1) = l(t) + \Delta l(t) \tag{4.4}$$

$$\theta(t + 1) = \theta(t) + \omega_{max}\hat{\omega}T \tag{4.5}$$

where, $l(t)$ is the insertion depth and $\theta(t)$ is the rotation angle at time step t. $\Delta l(t)$ is the increment of the insertion depth at time step t, which could be variable speed, in the case of constant speed $\Delta l(t) = u_1 T$. Note that rotation angle θ of Eq. (4.5) has no dependence on insertion depth l of Eq. (4.4), and thus its control is uncoupled with insertion. Substituting the discrete control inputs in Eqs. (4.4) and (4.5) into the bicycle model in Eq. (4.1), would obtain the needle tip position. Fig. 4.5 shows representative set points of needle rotation angle and speed, and corresponding needle tip trajectory for this simulation. In this study, torsional friction acting between the needle and tissue during insertions is ignored.
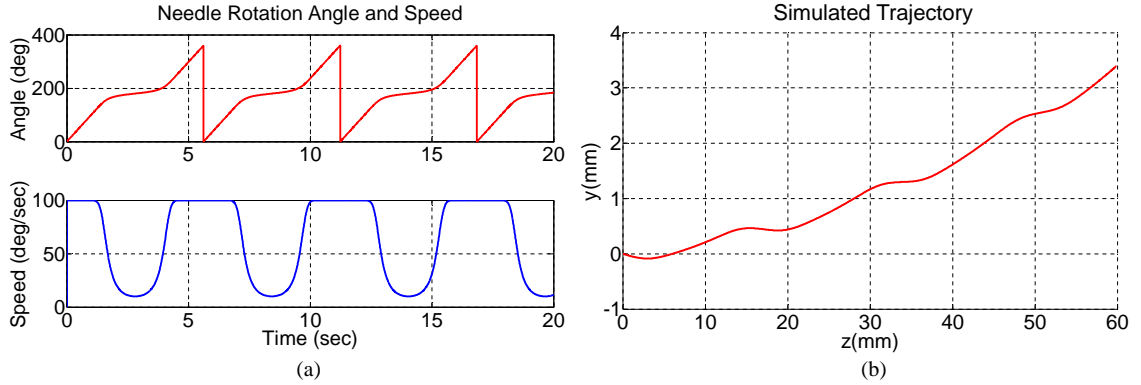
Figure 4.5: Representative plot of needle trajectory during a controlled insertion with CURV model parameters $\alpha = 0.9$, $\theta_d = 180°$, $c = 20$ (a) Needle angle and angular velocity as a function of time. (b) Corresponding needle tip trajectory. Note that the tip follows a helical profile as the needle rotates during insertion; the size of the helix could be minimized by tuning the speed ratio of rotation to insertion, as discussed in Section III. D. This helical profile was intentionally exaggerated to show the motion profile, and in practice it would follow substantially a smooth curve.

4.2.3 CURV Model Parameters Identification

Parameters of the kinematic model (l_1, l_2, κ, ϕ) could be calibrated experimentally to fit the needle trajectory and used as constants in the model. Variable curvatures of the needle trajectory could be achieved by actively adjusting parameters of the CURV steering model (α, θ_d) while inserting inside soft tissue. To identify the effects of model parameters on the needle trajectory and validate the feasibility of needle steering model, numerical simulation is performed with MATLAB (Mathworks, Natick, MA).

4.2.3.1 Steering Effort

The model described in [26] has a fixed front wheel angle ϕ, essentially generating a fixed curvature in the plane. By adjusting the steering effort α, the proposed CURV

138

approach effectively enables variable control of the front wheel angle ϕ and thus the curvature κ. As α changes from 0 to 1, the minimum value of the rotation speed decreases and the curvature of needle path increases from straight to the maximum curve that a needle can achieve, as shown in Fig. 4.6.

For a certain fixed steering effort, the needle will follow a path with constant curvature when all the other parameters are constant. By adjusting the steering effort α during the insertion procedure, complex trajectories with combined constant curvatures could be achieved, as shown in Fig. 4.7. The relationship between the steering effort and curvature depends on the properties of the needle and tissue, and could be calibrated experimentally as presented in Section 4.2.6.1.
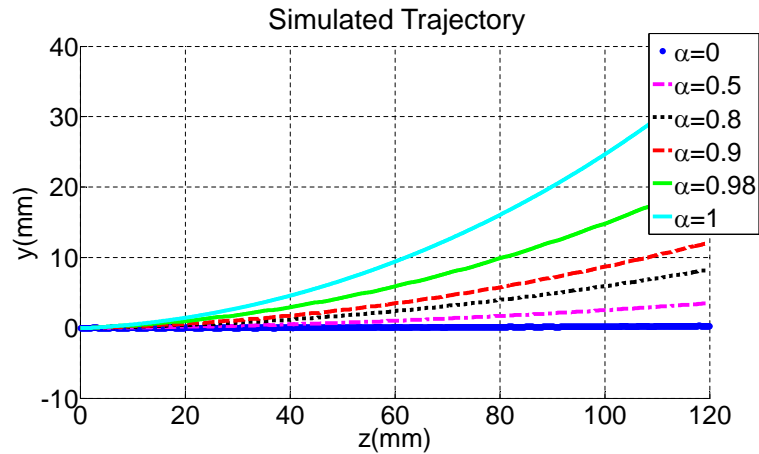
Figure 4.6: Representation of the relationship between needle curvature κ and the steering effort α. Note that $\alpha = 1$ corresponds to a track with maximum curvature and $\alpha = 0$ corresponds to a straight track.

4.2.3.2 Desired Rotation Angle

The desired rotation angle θ_d determines the direction of the needle path. Based on the rotation motion profile shown in Fig. 4.4, the needle rotates at relatively lower speed at desired rotation angle θ_d within the Gaussian width c, and wherein it is inclined to bend towards θ_d due to the asymmetric interaction force with tissue. Out of the Gaussian width c, the needle rotates at relatively higher speed and tends to follow a straighter path, similar to the drilling motion. As θ_d changes from $0°$ to $360°$, the plane that contains the needle path rotates accordingly towards θ_d, and thus reorients the needle path to the desired direction, as shown in Fig. 4.8. Complex needle paths with varying rotation directions could be achieved via tuning the desired rotation angle θ_d when inserting the needle, as shown in Fig. 4.9.
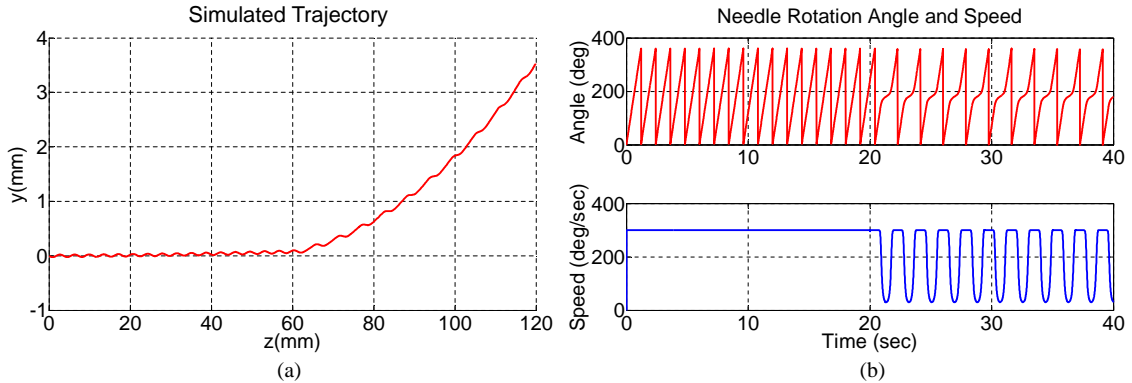
Figure 4.7: (a) A representative plot of needle insertion path during a controlled insertion where needle is inserted straightly ($\alpha = 0$, $\theta_d = 180°$, $c = 20$) and then changes to a constant curvature at 60 mm/20 sec ($\alpha = 0.9$, $\theta_d = 180°$, $c = 20$). (b) Corresponding plot showing needle angle and angular velocity with respect to time.
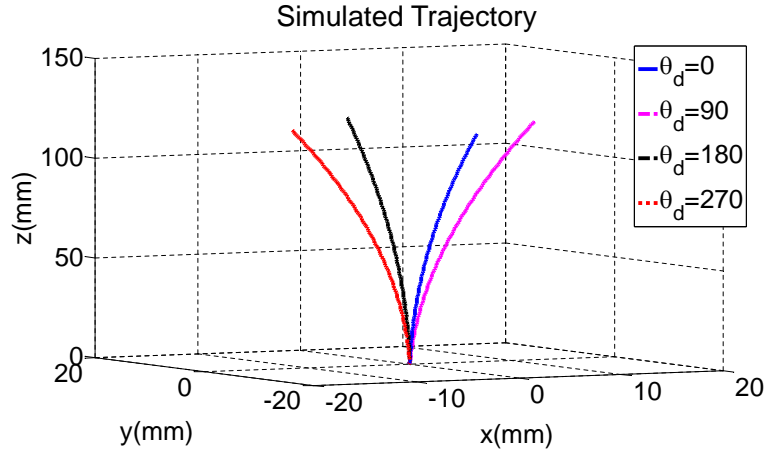
Figure 4.8: Representation of the relationship between needle path direction and the desired rotation angle θ_d.

(a)   (b)
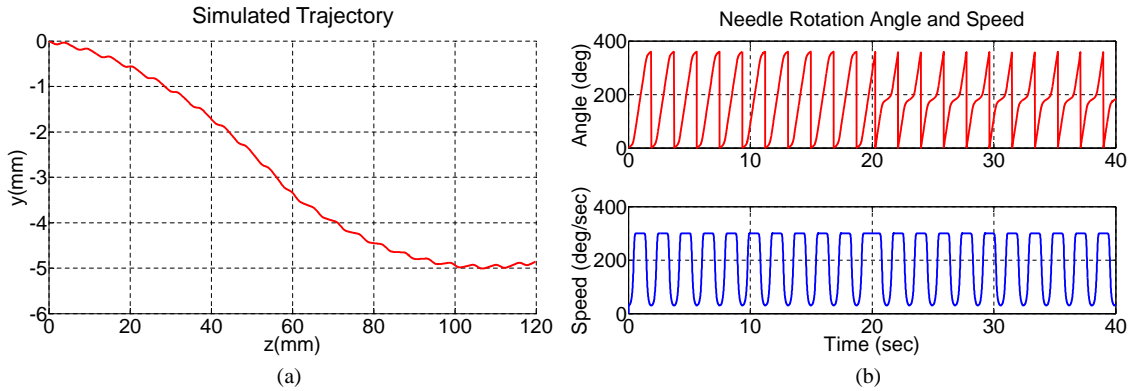
Figure 4.9: (a) A representative plot of an S-curve with double bend that has a point of inflection at 60 mm/20 sec. In this example, the needle inserts with a constant curvature in one direction ($\alpha = 0.9$, $\theta_d = 0°$, $c = 20$), and then changes to an opposite direction with the same constant curvature ($\alpha = 0.9$, $\theta_d = 180°$, $c = 20$). (b) Corresponding plot showing needle angle and angular velocity with respect to time.

4.2.3.3   Gaussian Width

According to the motion profile, as shown in Fig. 4.4, the Gaussian width c determines the range of the low speed region, and therefore affects the curvature of the needle trajectories. Fig. 4.10 shows varying curvatures obtained from different

Gaussian width c. As c changes from $0°$ to $60°$, the difference of width between the high speed and low speed region increases; While as c changes from $60°$ to $180°$, the difference decreases; As c equals to $60°$, the difference reaches the maximum value, where the needle trajectory achieves the maximum curvature, as shown in Fig. 4.10. (According to the properties of Gaussian distribution, 99.7% of the profile are within the $6c$ range. The rotation range is $360°$, and thus when c equals to $60°$, the whole motion profile forms a normal distribution, where the difference reaches the maximum value.) In practice, to simplify the control system, Gaussian width is set as a constant. Thus, the curvature is adjusted only by the steering effort during the steering.
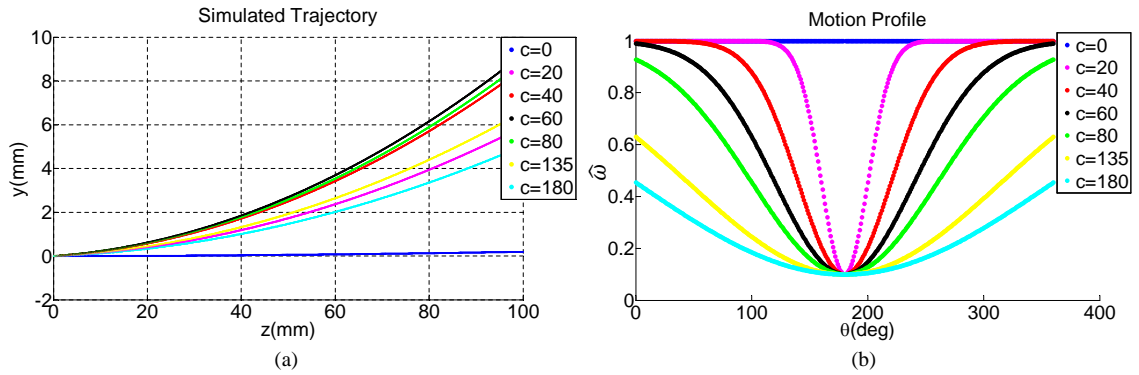
Figure 4.10: (a) Representative needle trajectories with varying Gaussian width c ($\alpha = 0.8$, $\theta_d = 180°$) and (b) corresponding motion profiles. Note that, at $c = 60°$ the curvature of trajectory reaches the maximum value.

4.2.3.4　Speed Ratio of Rotation to Insertion

In this proposed CURV steering model, the needle rotates about its primary axis continuously during insertion, and the needle tip position follows a helical profile. The size of the helix is related with the speed ratio of rotation to insertion. As shown in Fig. 4.11, higher speed ratio of rotation to insertion could form a smaller helix, and vice versa. But the overall profiles of needle path are the same for both cases. In general, the system operates with rotation speed much greater than insertion speed to reduce the helix size.
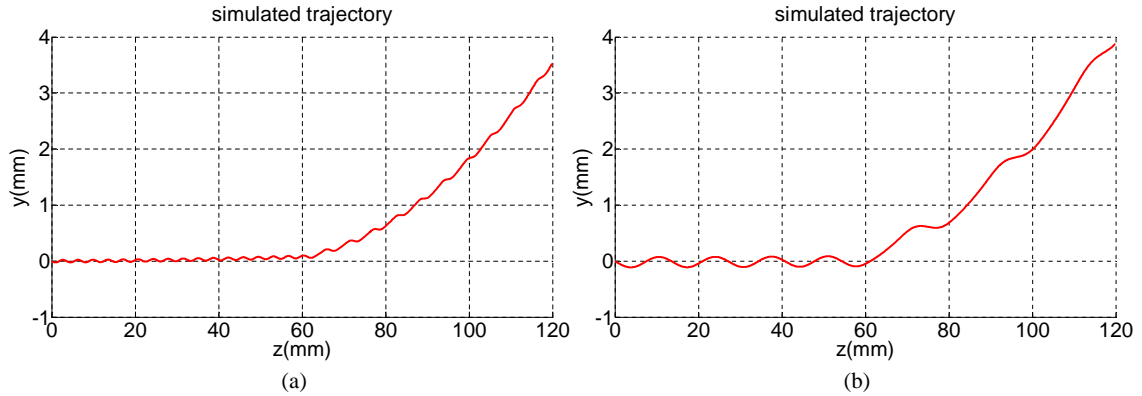
Figure 4.11: Demonstration of needle insertions with different speed ratios of rotation to insertion where needle goes straight for 60 mm and then with constant curvature for 60 mm. (a) A smaller helix of tip position is formed when the speed ratio is higher. ($\omega_{max} = 300$ deg/sec, $u_1 = 3$ mm/sec) (b) A larger helix is formed in the case that the speed ratio is lower. ($\omega_{max} = 80$ deg/sec, $u_1 = 3$ mm/sec)

4.2.4　Closed-loop Control of CURV Steering

The CURV steering model predicts the needle trajectory with known steering effort α, desired rotation angle θ_d and insertion depth l, i.e. describing the forward kine-

matics of needle steering. With a given target, a image-based controller is designed to calculate corresponding steering effort α, desired rotation angle θ_d and insertion depth l needed to steer the needle towards the target.

4.2.4.1 Autonomous Needle Tracking with Continuous MR Images

The needle tip location could be acquired by a image-based position feedback system (e.g. camera, CT, MRI images, etc.). In this study, an autonomous needle tracking application, which was developed by our team [96], is utilized to provide position feedback. It is able to continuously acquire live MR images and autonomously segment the 3D needle tip coordinates at a frequency of $1.3fps$. The tracking application communicates with the MRI scanner console (3T Achieva scanner, Philips) via the external control interface (XTC Corba Data Dumper, Philips) to acquire MR images and control the imaging scan geometry (i.e. imaging position and orientation). One sagittal and one coronal image is acquired continuously one after the other to obtain two normal projection images of the needle, as shown in Fig. 4.12 (a). A fast image acquisition sequence, Spoiled Gradient Echo sequence T1-FFE (Fast Field Echo), is utilized to acquire the MR image in every 750 ms for either sagittal or coronal plane. In order to keep the needle tip visible in both images during the insertion, the scan geometry is continuously updated based on the latest needle tip position. As shown in Fig. 4.12 (a), sagittal image is translated along R-axis, while coronal image is moved

along A-axis, maintaining the tip localized at the cross section. Detailed description of needle tracking application is presented in our previous study [96].

Utilizing the two projection images, the 3D needle tip tracking task is reduced into 2D image plane. The 2D MR images provide cross-sectional view of the needle tip in sagittal and coronal plane, which has a shape of two blob due to the artifact introduced by the nitinol material and sharp bevel tip. The centroid of the two blob is defined as the needle tip. A series of image processing techniques over the region of interest are performed to segment and extract the needle tip, including median blurring, thresholding and contour detection, as illustrated in Fig. 4.12 (b)-(e). The 3D needle tip coordinates in MRI image space are determined by taking 'R' coordinate from coronal image, 'A' and 'S' coordinates from sagittal image, assuming that 'S' coordinate is identical in both images.

4.2.4.2   Needle Pose Estimation

Fig. 4.13 illustrates the coordinate frame of the target and needle tip in global frame. The target position T_{tar} is considered to be a 3D static location, and manually defined by the user on the image. The 6D needle tip pose T_{tip} can be calculated with the information acquired by the needle tracking application, which is defined by a 3×3 rotation matrix R_{tip} and a 3×1 position matrix P_{tip}, as
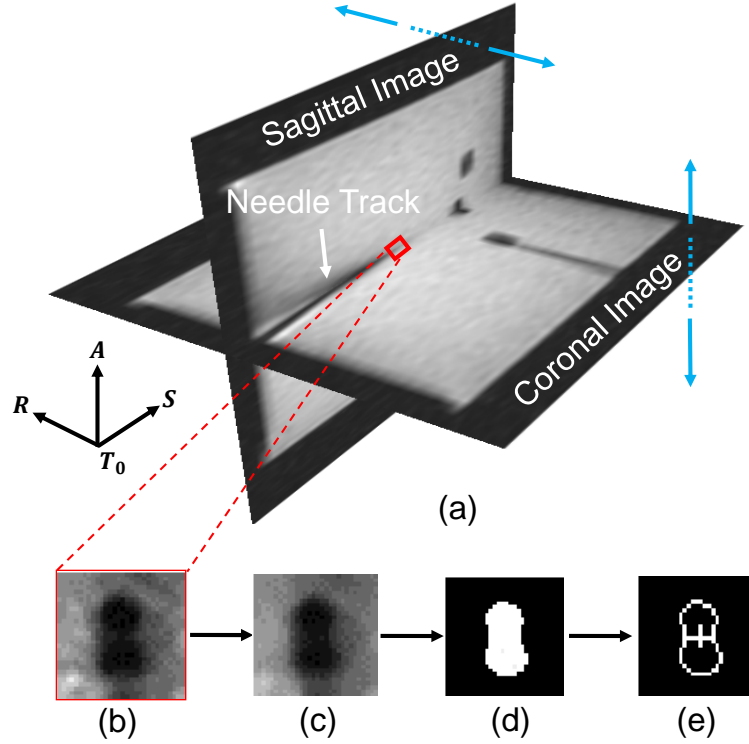
Figure 4.12: Autonomous needle tracking with continuously updated MR images in image space (RAS coordinate frame, Right-Anterior-Superior). (a) MRI scan geometry control of sagittal and coronal image plane: sagittal image plane is moved along R-axis, while coronal image plane is moved along A-axis. (b) A cropped portion of the original image on both sagittal and coronal image plane. (c) A median blur filter is used to reduce speckle in the MR image. (d) Thresholding is applied to achieve a binary image of the needle tip. (e) Contour detection and center of contour bounding box is utilized to obtain the centroid of needle tip.

$$T_{tip} = \begin{bmatrix} R_{tip} & P_{tip} \\ 0 & 1 \end{bmatrix} \tag{4.6}$$

The position vector P_{tip} is defined as the latest needle tip position acquired by the needle tracking application. The rotation matrix R_{tip} is determined by the tip positions acquired within the last N mm insertion depth. The rotation angles around X-axis and Y-axis are obtained by least-square line fitting of the needle trajectory

146

within last N mm insertion in YZ and XZ plane respectively. The rotation around Z-axis is the desired rotation angle $\theta_{d(t-1)}$ in previous step. Therefore the rotation matrix R_{tip} can be obtained as

$$Z = aY + b \Rightarrow \theta_X = arctan(a)$$

$$Z = cX + d \Rightarrow \theta_Y = arctan(c) \tag{4.7}$$

$$\theta_Z = \theta_{d(t-1)}$$

$$R_{tip} = R_Z(\theta_Z) \cdot R_Y(\theta_Y) \cdot R_X(\theta_X) \tag{4.8}$$
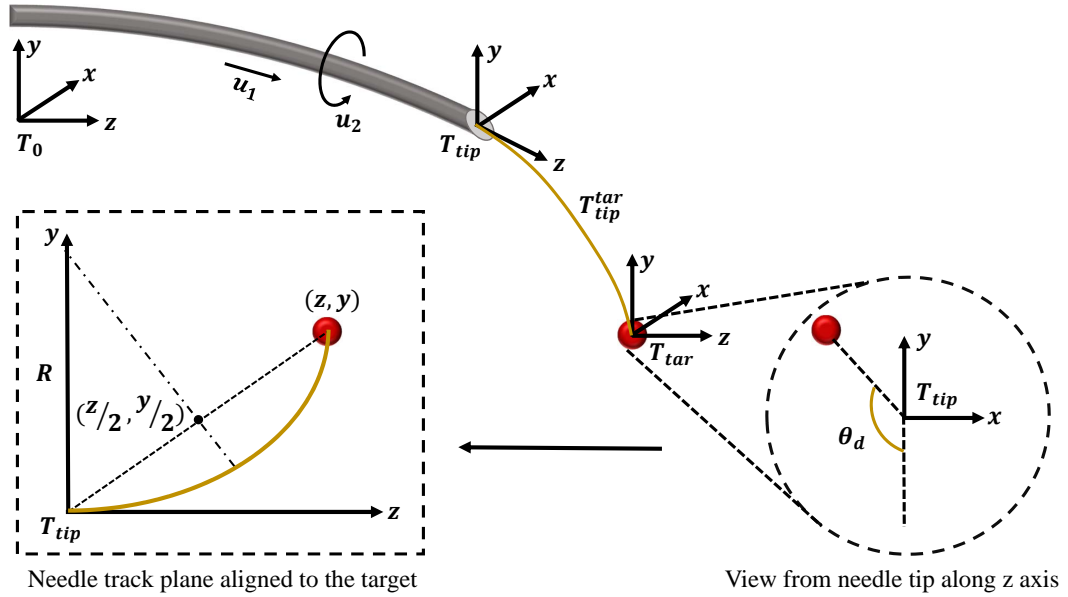
Figure 4.13: Needle steering parameter calculations, where θ_d is the desired rotation angle, T_{tip} is the needle tip frame and T_0 is the global reference frame.

4.2.4.3 Image-guided Controller

The homogeneous transformation from the target to the tip can be calculated as:

$$T_{tip}^{tar} = T_{tip}^{-1} \cdot T_{tar} \tag{4.9}$$

In the needle tip frame, the desired rotation angle θ_d is the relative rotation angle around Z-axis from current tip to target, and thus can be determined as

$$\theta_d = arctan(x, y) + \frac{\pi}{2} \tag{4.10}$$

where x, y are the coordinates of the target in the needle tip frame (T_{tip}^{tar}). The addition of $\frac{\pi}{2}$ is due to the definition of the used axis system where $0°$ is aligned with the negative Y-axis. After aligning the needle pose to the target, the needle track from current tip to target is reduced to 2D plane and the curvature of the needle track can be expressed as

$$\kappa = \frac{1}{R} = \frac{1}{\frac{y}{2} + \frac{z^2}{2y}} \tag{4.11}$$

The calculated curvature κ is compared to the calibrated relation of steering effort and curvature in Fig. 4.18, to determine corresponding steering effort α. The obtained steering effort α and desired rotation angle θ_d are sent to robot controller to generate rotation motion profile with the CURV steering model. The insertion depth

is determined based on the position difference along Z-axis between the target and current needle tip position, which is updated in each control cycle. The needle steering algorithm for calculating the parameters of CURV model is outlined in Algorithm 1. Fig. 4.14 illustrates the flow chart of image-guided closed-loop control of CURV steering. By taking advantage of image-based position feedback, the modeling error could be compensated and corrected via the closed-loop control.

Algorithm 1 $[l, \alpha, \theta_d] \leftarrow$ needle_steering $(\boldsymbol{T_{tip}}, \boldsymbol{T_{tar}}, \Delta, \Delta l)$

1:   $\boldsymbol{T_{tip}^{tar}} \leftarrow \boldsymbol{T_{tip}^{-1}} \cdot \boldsymbol{T_{tar}}$

2:   **while** $(\mathrm{abs}(\boldsymbol{P_{tar}} - \boldsymbol{P_{tip}}) > \Delta)$ **do**

3:      $\theta_d \leftarrow \arctan(x, y) + {}^{\pi}\!/_2$

4:      $\kappa \leftarrow 1/({}^{y}\!/_2 + {}^{z^2}\!/_{2y})$

5:      **if** $(\kappa > \kappa_{max})$ **then**

6:        $\kappa = \kappa_{max}$

7:      **end if**

8:      $\alpha \leftarrow$ lookup_table(κ)

9:      $l \leftarrow l + \Delta l$

10: **end while**

11: **return** $[l, \alpha, \theta_d]$

4.2.5   Teleoperated Needle Steering

As aforementioned in Section 4.2.2, the needle insertion speed u_1 is an independent control input which could be performed in a teleoperated fashion, while the rotation
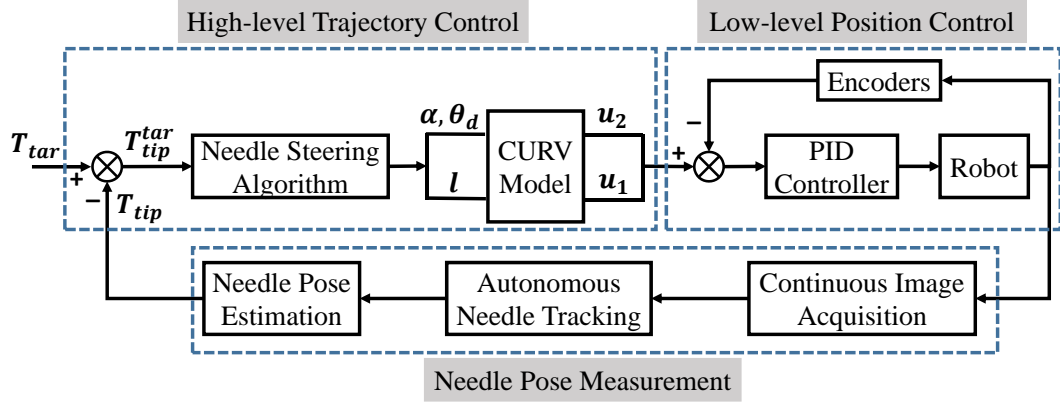
Figure 4.14: Flow chart of image-guided closed-loop control of CURV needle steering with position feedback.

is generated by the CURV steering model. An MRI-compatible teleoperated robotic system developed by the lab [97] is utilized as the validation platform. The position of master and slave robot are recorded by the MRI compatible optical linear encoder (EM1-0-500-I linear 0.0127 mm/count, US Digital, Vancouver, WA), which are fed into robot controller to generate motion command. The slave robot follows the master device with a position based control loop as:

$$\Delta P_{slave} = K_p \Delta P_{master} + C \qquad (4.12)$$

Where ΔP_{master} is position difference of master device. K_p is the scale factor (in this study it is defined as 1). C is the constant position offset of master device(in this study it is defined as 0). The position tracking accuracy is proven to be 0.318mm [97]. ΔP_{slave} is the relative position increment of slave robot, i.e. the command motion value for insertion per control cycle.

Fig. 4.15 illustrates the system setup of the teleoperated needle steering under continuous MRI-guidance. The slave robot manipulator is placed closed to the isocenter of MRI scanner bore, placing the needle in 6-D position. The user operates the master device outside the scanner bore to teleoperate the needle interventions with visual feedback.
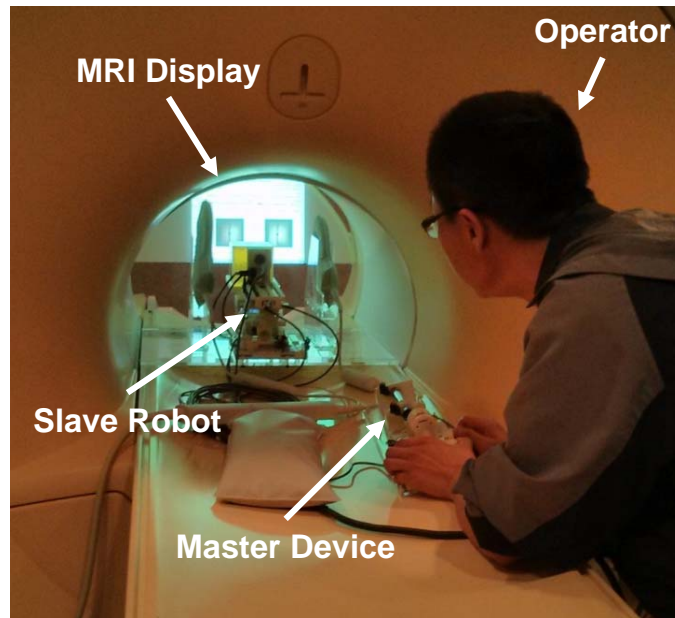
Figure 4.15: System setup for teleoperated CURV needle steering. The user operates the master device outside the scanner bore to teleoperate the needle interventions while observing the updated needle track under MRI-guidance.

4.2.6 Experiments and Results

The CURV steering model is first verified and validated in open-loop with camera-based phantom studies in 2D, and then further evaluated in 3D with high resolution CT images. The targeting accuracy of the closed-loop control of CURV needle steering is assessed with phantom study under continuous live MRI-guidance. A $21G$ (0.8

mm diameter) flexible nitinol needle with 30° bevel-tip angle is inserted into a gelatin phantom made with 13% concentration (13% gelatin mixed with 87% water by weight) for this series of experiments. A 6-DOF piezoelectrically actuated robotic system that originally developed for MRI-guided prostate interventions is utilized as the testbed to control both insertion and rotation of the bevel-tip needle, as presented in Section 3.7.1. The needle insertion is implemented with linear guide mechanism driven by two linear piezomotors, and the rotation is driven by one rotary piezomotor through pulley-belt mechanism. The detailed description of the robotic system is presented in [98] [66]. Two high definition web cameras with resolution of 1280×720 pixels (LifeCam HD-3000, Microsoft) are firmly mounted on the top and lateral side of the platform to capture the needle track. A reference marker frame is attached on the robot close to the needle guide to calibrate the pixel size of the camera image (the pixel size is 0.2 mm $\times$ 0.2 mm). The experimental setup with cameras is shown in Fig. 4.16.

4.2.6.1   2D Validation of CURV Model with Camera

The 2D validation of CURV model includes 2 steps, 1) calibrating model parameters and assessing simple curve track with constant parameters (i.e. steering effort α and desired rotation angle θ_d are constant during each single insertion), and 2) assessing complex curve track with changing parameters (i.e. steering effort α or desired rotation angle θ_d are actively adjusted during each single insertion).
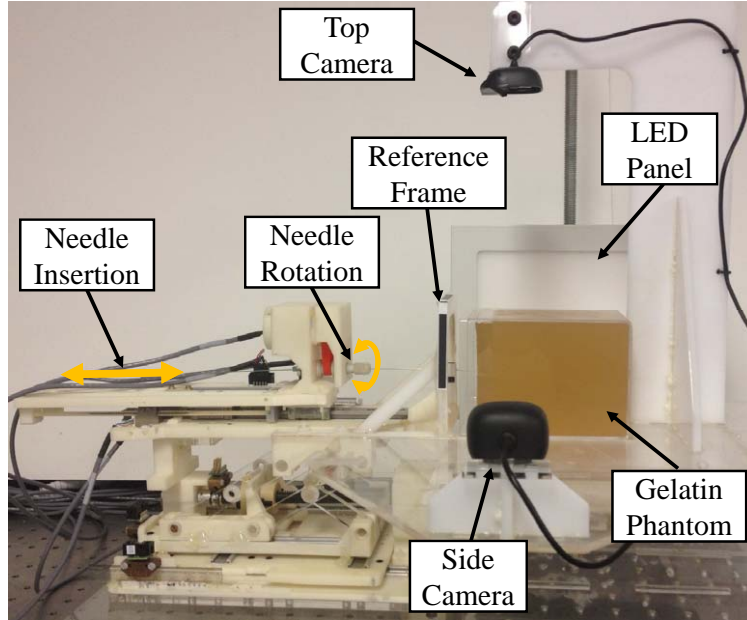
Figure 4.16: Experimental setup for phantom studies of CURV steering model validation in 2D with cameras.

For the first assessment, the needle is inserted into the phantom with 7 different values of steering effort α and repeated 3 times for each α, the insertion depth is 90 mm and desired rotation angle is $0°$ for all the 21 insertions, as shown in Fig. 4.17. 20 points with an interval of about 4.5 mm along the actual needle track captured by the camera are collected and compared with the predicted model to evaluate the trajectory accuracy. RMS error and standard deviation (SD) of the 20 data points are used as a metric and summarized in Table. 4.1. In this study, curvature κ and needle tip location l_2 are experimentally calibrated, by fitting the theoretical model to the actual needle trajectories. The front wheel angle ϕ is calculated based on the function $1/\kappa = \sqrt{(l_2)^2 + (l_1 \cot(\phi))^2}$, as presented in [26], by choosing base length $l_1 = 250$ mm as a constant parameter. The results demonstrate that the commanded steering

effort α effectively affects the curvature κ, and the RMS errors of trajectory fitting are less than 0.50 mm, which is comparable to the duty-cycled spinning approach 0.34 mm [88]. The relation between the steering effort α and curvature κ is illustrated in Fig. 4.18. Pleas note that this is one example calibration for the needle and phantom used in this study, and the calibration may be different for other needle configurations (stiffness, tip shape, and diameter) and phantom/tissue properties. The nonlinear relation could be fitted with linear interpolation among the sample data points to calculate corresponding curvature of the steering effort.

Table 4.1: 2D CURV Model Validation

Steering Effort	κ (mm^{-1})	ϕ (deg)	l_2 (mm)	Trial 1 (mm)		Trial 2 (mm)		Trial 3 (mm)	
				RMS	SD	RMS	SD	RMS	SD
0	0.0000	0	0	0.13	0.09	0.18	0.10	0.10	0.08
0.5	0.0007	10.03	210	0.24	0.16	0.30	0.17	0.32	0.22
0.8	0.0010	14.10	95	0.46	0.33	0.30	0.22	0.34	0.17
0.9	0.0016	21.96	78	0.47	0.22	0.44	0.21	0.34	0.18
0.95	0.0022	28.93	45	0.40	0.24	0.36	0.17	0.47	0.25
0.98	0.0024	31.04	32	0.30	0.16	0.20	0.09	0.38	0.16
1	0.0041	45.75	14	0.16	0.07	0.10	0.06	0.25	0.17

For the second assessment, the needle is firstly inserted with a single-curve track: inserted 40 mm with steering effort 0 and then inserted 60 mm with steering effort 0.95, the desired rotation angle is 180° for the whole insertion. Secondly, it is inserted with a double-curve track: inserted 50 mm with desired rotation angle 180° and then inserted 50 mm with desired rotation angle 0°, the steering effort is 0.95 for the whole insertion. Both trials are repeated 5 times. 22 points with an interval of about 4.5
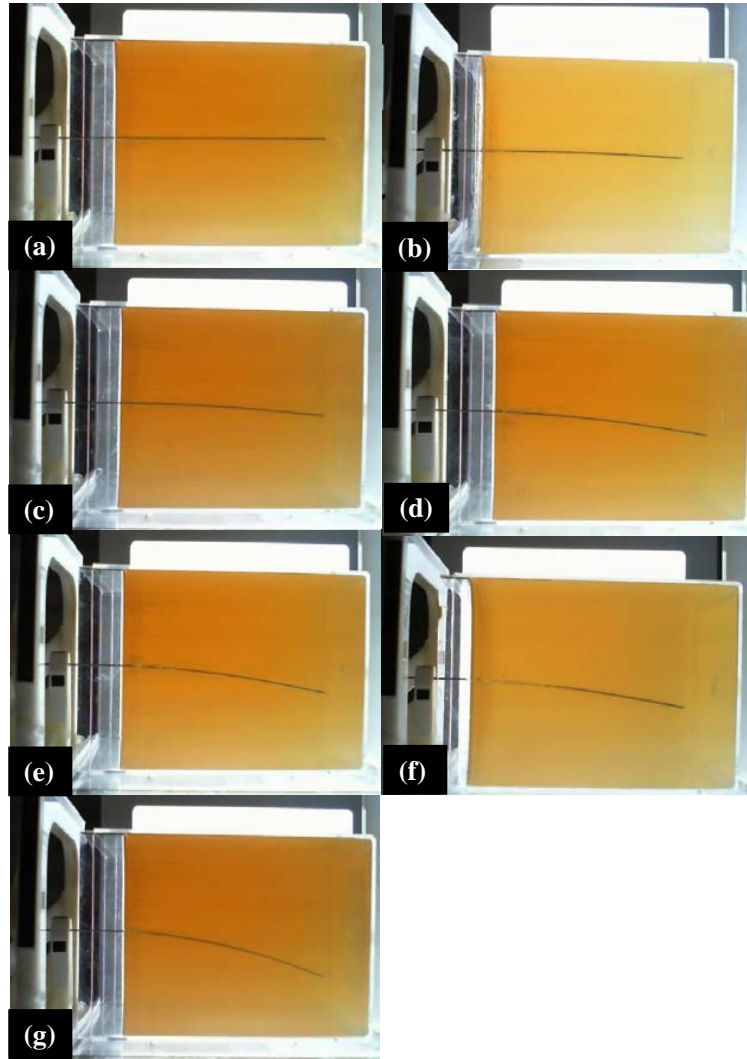
Figure 4.17: Representative needle tracks of insertions with varying steering effort captured by the side camera. (a) $\alpha = 0$ (b) $\alpha = 0.5$ (c) $\alpha = 0.8$ (d) $\alpha = 0.9$ (e) $\alpha = 0.95$ (f) $\alpha = 0.98$ (g) $\alpha = 1$.

mm are collected for both actual and desired needle tracks, and compared to assess the trajectory accuracy. As shown in Fig. 4.19 and 4.20, the predicted model fits well with the actual needle track, demonstrating the results with 0.49 mm RMS error, 0.33 mm SD and 1.43 mm RMS error, 0.67 mm SD for single-curve and double-curve trials respectively. Please note that deflection of around 10 mm with 100 mm insertion is
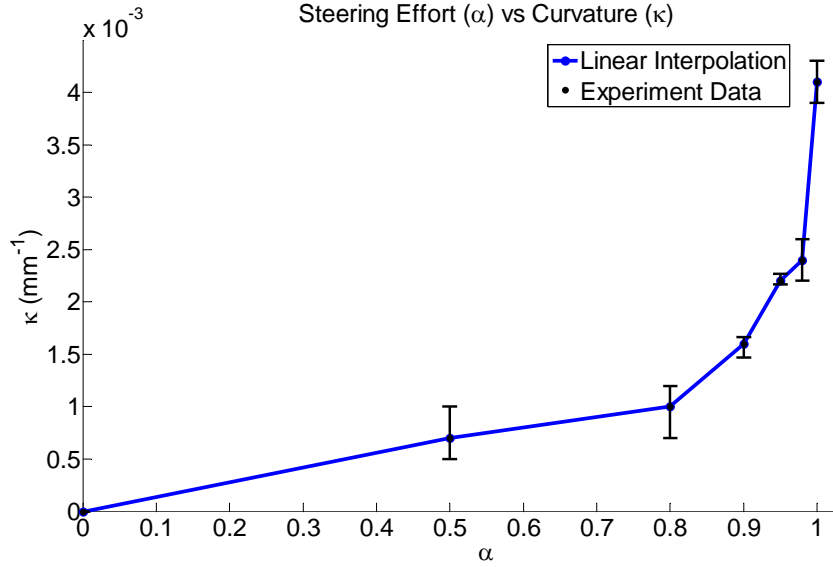
Figure 4.18: Relation of steering effort α and curvature κ.

realistic for active compensation of needle placement error for clinical applications. The modeling error for double-curve track is relatively bigger than single-curve track, which is mainly caused by the un-modeled torsional force. The torsional force could cause tip angle errors and reduce the potential curvature of the needle track, especially for the case of double-curve track.

4.2.6.2 3D Validation of CURV Model with CT

3D trajectory accuracy of the CURV model is evaluated with phantom studies in a Phillips CT Scanner. **High resolution CT images are utilized to reduce the needle tip artifact that presented in MR images and therefore to provide more precise evaluation of the trajectory accuracy.** Three insertions are performed with different control parameters: 1) inserting 50 mm with steering effort
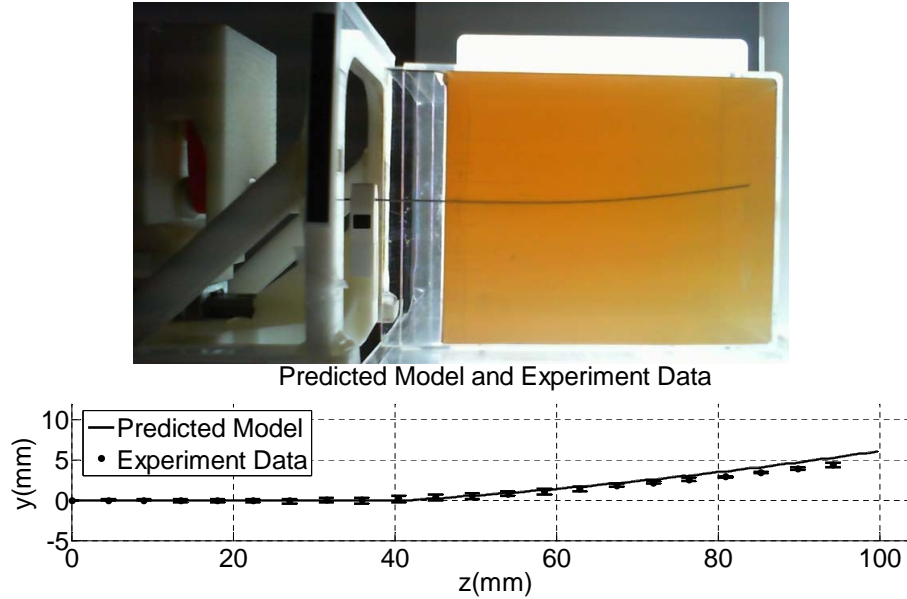
Figure 4.19: (Top) A representative needle track of single-curve trial captured by the camera. (Bottom) The predicted model with average and standard deviation of experimental data.

0 and then inserting 50 mm with steering effort 0.9, desired rotation angle for the whole insertion is 0°; 2) inserting 50 mm with steering effort 0.8 and then inserting 50 mm with steering effort 1, desired rotation angle for the whole insertion is 148°; 3) inserting 50 mm with steering effort 0.95 and then inserting 50 mm with steering effort 0, desired rotation angle for the whole insertion is 235°. Corresponding curvature κ and needle tip location l_2 are determined by Table. 4.1. Desired needle tracks are compared to the actual needle tracks that manually segmented from high resolution CT image (voxel size of 0.2865 mm $\times$ 0.2865 mm $\times$ 0.2865 mm) to assess the accuracy. The open-loop trajectory accuracy for the three trials are 0.496 mm RMS, 0.296 mm SD, and 0.537 mm RMS, 0.229 mm SD, and 0.559 mm RMS, 0.303 mm SD respectively, as show in Fig. 4.21. A representative CT image of needle track
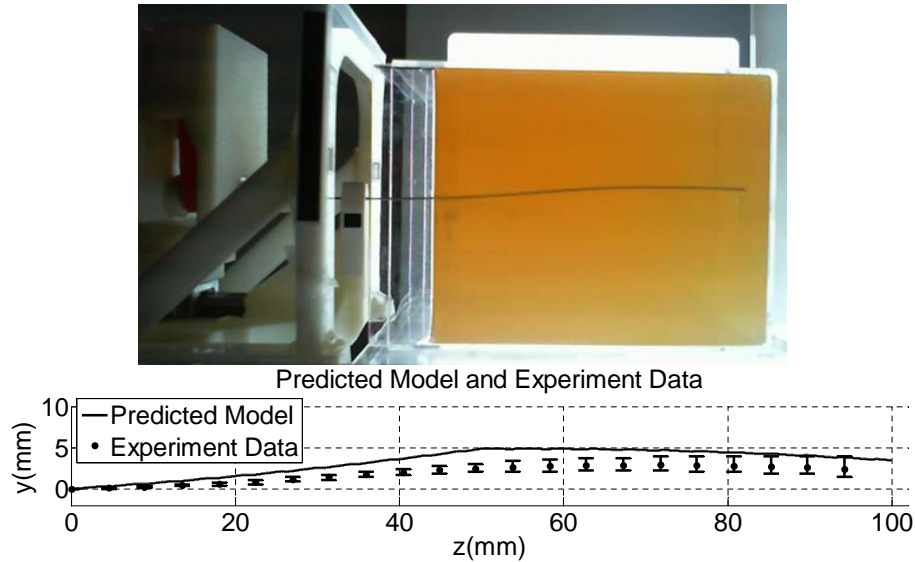
Figure 4.20: (Top) A representative needle track of double-curve trial captured by the camera. (Bottom) The predicted model with average and standard deviation of experimental data.

generated by the CURV steering model is shown in Fig. 4.22.

4.2.6.3 Closed-loop Accuracy Evaluation under Continuous Intraoperative MRI Guidance

The targeting accuracy of closed-loop control of CURV steering is evaluated with phantom studies inside a 3T MRI scanner (Achieva, Philips). Rubber rings are randomly embedded inside the gelatin phantom, serving as target markers. The needle is firstly inserted 5 mm into the phantom to acquire the initial needle tip entry point. During insertions, the needle tip position is autonomously tracked with Spoiled Gradient Echo MR imaging sequence T1-FFE (fast field echo, TR: 6.93 ms, TE: 3.37 ms, Flip angle: 5°), as described on Section 4.2.4.1. A diagnostic MR imaging sequence

158
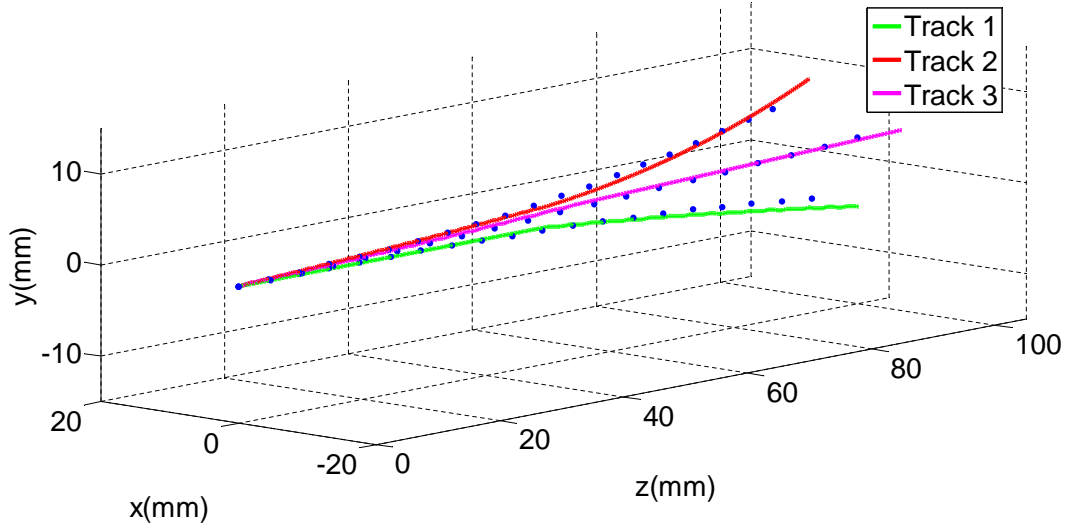
Figure 4.21: Results of three insertion trials in CT scanner. Green, red and magenta lines represent predicted trajectories based on the CURV steering model. Blue dots represent actual trajectories measured from CT images.

T2W-TSE (T2-weighted turbo spin echo, TR: 3030 ms, TE: 115 ms, slice thickness: 3 mm, reconstruction resolution: 0.5 mm × 0.5 mm) is acquired to identify the final tip position. 10 random targets are selected, and different entry points are considered for each insertion to prevent effects from previous needle tracks. The target accuracy is assessed by comparing the desired target positions to the actual tip positions that manually segmented from MRI confirm images. The accuracy results of closed-loop control of needle steering are summarized in Table 4.2. A representative MRI image of the needle track generated by the closed-loop CURV steering model, overlaid with tracked needle tips, is shown in Fig. 4.23. The experiment demonstrates that the RMS error of 3D targeting accuracy is 0.75 mm. In most clinical procedures, the in-plane error has more significant meaning than the error along S-axis, since the in-
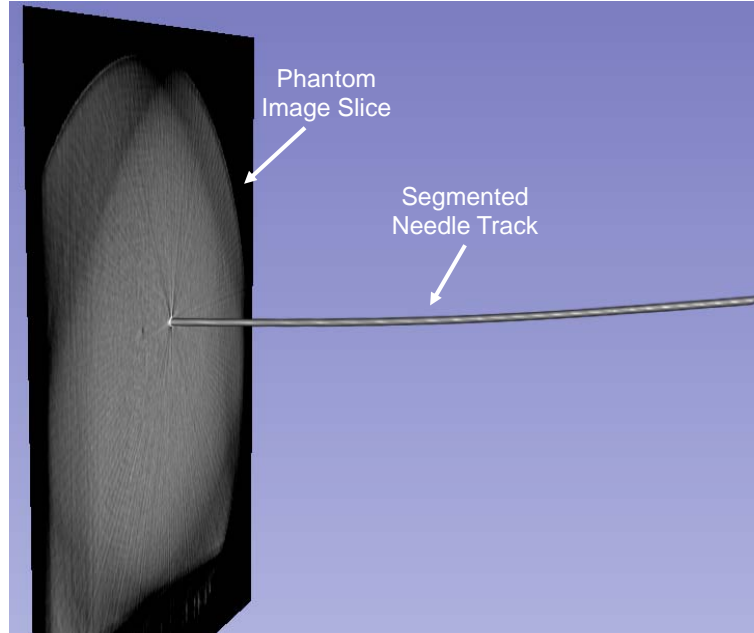
Figure 4.22: Segmented 3D CT image volume showing a representative curved needle track of a bevel-tip needle inserted into a gelatin phantom generated by the CURV steering model. The phantom is shown with single slice image at the entry point of needle track.

sertion depth could be adjusted to align with the target plane. Thereby, the in-plane errors are also assessed in this study and the RMS error is 0.73 mm.

Table 4.2: Accuracy Evaluation of Closed-loop CURV Steering with Automatic Insertion under MRI-Guidance

Target	Target Position (mm)			Actual Tip Position (mm)			Error (mm)				
NO.	R	A	S	R	A	S	R	A	S	In-plane (RA)	Total
1	18.22	54.58	-25.09	18.8	55.0	-24.9	0.58	0.42	0.19	0.72	0.74
2	13.35	63.20	-25.09	13.6	62.2	-25.0	0.25	1.00	0.09	1.03	1.03
3	10.35	55.33	-26.22	10.6	54.9	-26.3	0.25	0.43	0.08	0.50	0.50
4	14.47	61.95	-19.60	13.6	61.9	-19.6	0.87	0.05	0	0.87	0.87
5	15.47	54.95	-18.00	15.1	56.2	-18.1	0.37	1.25	0.10	1.30	1.31
6	8.50	61.95	-19.00	8.6	62.2	-19.0	0.10	0.25	0	0.27	0.27
7	9.10	53.95	47.00	9.4	54.0	46.5	0.30	0.05	0.50	0.30	0.59
8	17.10	61.58	49.00	17.0	62.0	48.9	0.10	0.42	0.10	0.43	0.44
9	17.73	60.58	50.00	17.9	61.3	49.8	0.17	0.72	0.20	0.74	0.77
10	14.48	51.58	49.00	14.4	51.9	48.9	0.08	0.32	0.10	0.33	0.34
Standard Deviation (mm)							0.24	0.37	0.14	0.33	0.31
Mean Error (mm)							0.31	0.49	0.14	0.65	0.69
RMS Error (mm)										0.73	0.75
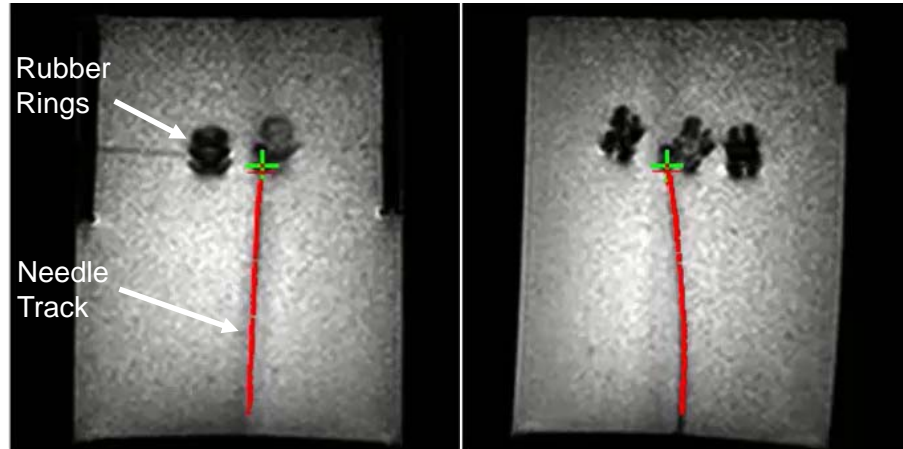
Figure 4.23: MRI image of a curved needle track generated by the closed-loop CURV needle steering inside a gelatin phantom, shown in 2D sagittal (left) and coronal (right) planes. Red dots represent the tracked needle tips, overlaying on the actual needle track. Red cross stands for the final tip position, and the green cross represents for the desired target.

4.2.6.4 Needle Steering with Teleoperated Insertion

The needle insertion is controlled by the master device, which is manually operated by the user. 10 random targets are selected. The accuracy of needle steering with teleoperated insertion is summarized in Table. 4.3

4.3 Concentric Tube Continuum Cannula

4.3.1 Kinematic Model

Our prototype concentric tube continuum cannula is made of three concentric elastic tubes. The outer tube and inner tube are naturally straight, while the middle tube has a pre-curved section at its tip with a constant curvature $\kappa = 0.0138/mm$. Further

Table 4.3: Accuracy Evaluation of Closed-loop CURV Steering with Teleoperated Insertion under MRI-Guidance

Target NO.	Target Position (mm)			Actual Tip Position (mm)			Error (mm)				
	R	A	S	R	A	S	R	A	S	In-plane (RA)	Total
1	13.05	52.53	46.00	13.1	53.3	46.1	0.05	0.77	0.10	0.77	0.78
2	13.70	62.90	46.00	14.1	62.4	45.9	0.40	0.50	0.10	0.64	0.65
3	16.70	62.03	48.00	16.6	62.0	48.1	0.10	0.03	0.10	0.10	0.14
4	17.90	54.67	49.00	17.6	54.5	49.0	0.30	0.17	0	0.34	0.34
5	10.10	60.95	34.00	10.7	61.0	33.9	0.60	0.05	0.10	0.60	0.61
6	14.48	62.95	38.00	15.2	63.0	37.9	0.72	0.05	0.10	0.72	0.73
7	16.48	53.95	38.00	15.9	53.0	37.9	0.58	0.95	0.10	1.11	1.12
8	17.73	57.95	36.00	18.1	58.0	36.1	0.37	0.05	0.10	0.37	0.39
9	6.73	57.95	36.00	7.6	59.0	36.1	0.87	1.05	0.10	1.36	1.37
10	15.35	53.95	38.00	14.5	54.0	37.9	0.85	0.05	0.10	0.85	0.86
Standard Deviation (mm)							0.27	0.39	0.03	0.35	0.35
Mean Error (mm)							0.48	0.37	0.09	0.69	0.70
RMS Error (mm)										0.77	0.78
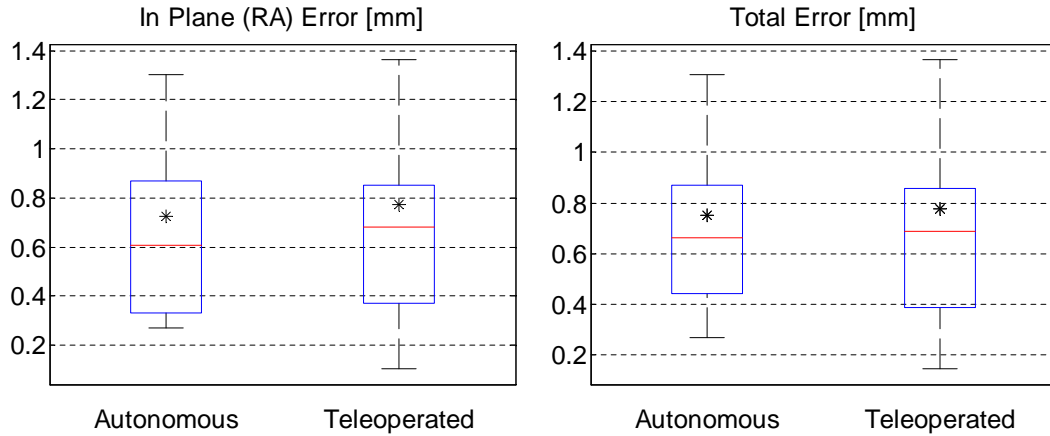
Figure 4.24: Comparison of the closed-loop needle steering accuracy with autonomous and teleoperated needle insertion. (Left) in plane (RA) position error, and (Right) total position error. ∗ represents for the RMS error.

tube geometry optimization is required for the specific clinical intervention based on anatomy and constraints, following the method proposed by Bergeles et al. [99]. The results presented for this example configuration may be generalized to other configurations based on tube geometry optimization. Nickel titanium, also known as nitinol, is used to fabricate the tubes and wire, due to its unique characteristics

162

of sustaining high strain without damage (sustain recoverable strain of as much as $\epsilon = 11\%$) [100], and high torsional rigidity compared to their flexural rigidity.

In general, torsional effects are important to consider whenever there are two or more tubes with overlapping curved sections. General model with no external loads has been studied by Dupont et al. [29] and Rucker et al. [28]. General model with external loads was presented by Rucker et al. [101] and Lock et al. [102]. The particular design in this study eliminates the need to consider torsion because there is only one pre-curved tube and hence no torsional deformation except that which is due to friction. So the model presented in this section is a special case where the general model reduces to a simple algebraic model due to the design choice of having only one precurved tube. However, the model in this study (and our recent conference papers [103] and [104]) is the only one to consider the angular offset resulting from tube clearances, which has been a source of error in prior models. The model was established under the main assumption of linear elasticity (constant Young's modulus) and the dominance of bending effects over the shear effects induced by bending. The kinematics model of the concetric tube cannula is developed by Dr. Webster at Vanderbilt University [26,93], and adopted in this study by calibrating the kinematic parameters of the specific design that used in this work and considering the angular offset of the tube clearances [105].

4.3.1.1   Mechanics of Concentric Tubes

An interaction effect occurs among the precured tubes, which are placed concentrically, causing bending into a combined shape different from the natural at-rest geometry of individual tubes. To describe the complete shape of the concentric tube robot, a mechanics model is established for the shape of a single "link" composed of several overlapping concentric curved tubes, based on the Bernoulli-Euler beam equation [93]:

$$\Delta \kappa = \frac{M}{EI} \qquad (4.13)$$

where $\Delta \kappa = \kappa - \kappa_i$ is the difference between the deformed curvature, κ, and the "at rest" precurvature, κ_i. M is the internal moment carried by the tube, E is the modulus of elasticity (Young's modulus), and I is the cross-sectional moment of inertia. In a similar way of describing the equilibrium position of linear springs of different lengths and stiffness when connected in parallel by a force balance, the resultant curvature in a segment of n overlapping tubes whose natural planes of curvature are aligned by:

$$k_r = \frac{\sum\limits_{i=1}^{n} E_i I_i k_i}{\sum\limits_{i=1}^{n} E_i I_i} \qquad (4.14)$$

for n tubes, where k_i are the preformed curvatures of the individual tubes.

4.3.1.2 Forward Kinematics

Forward kinematics of a concentric tube robot is a description of complete device shape in terms of the joint variables. The prototype concentric tube robot consists of four segments, each with constant curvature as shown in Fig.4.25. The length of each segment l_1, l_2, l_3, l_4 are calculated from the actuated distances q_1, q_2, q_3, which are the insertion distance of each tube's tip from its starting point. The starting point (i.e. home position) is defined to be the position where tips of each tube are at the constrained entry point. Considering the finite clearance between tubes, there would be an angular offset of α between the middle and outer tube, and an angular offset of λ between the middle and inner tube. The offset angles were experimentally measured using graph paper and goniometer, then calibrated by fitting the kinematic model.

The initial values of offset angles ($\alpha = 1.5°, \lambda = -2°$) are obtained by measuring the angle of 2 tangent lines at each segment, and then calibrated by fitting the theoretical model with experiment data to get the offset values which have minimum fitting errors. The constant tube length parameters are $L_1 = 65$ mm, $L_2 = 162$ mm, $L_c = 74$ mm, and $L_3 = 340$ mm.

The lengths of the sections shown in Fig.4.25 are given by:
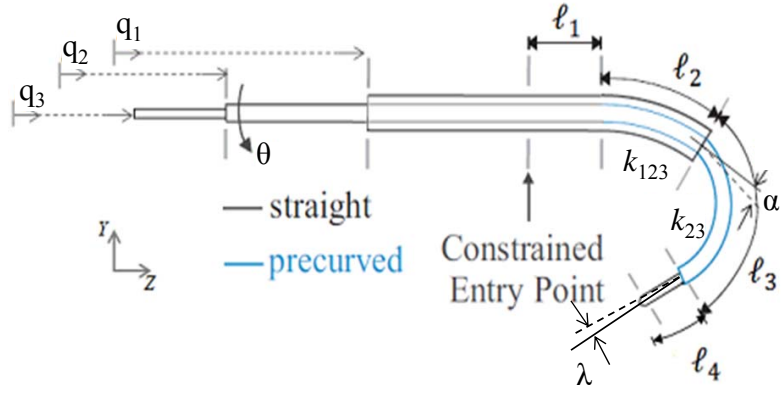
Figure 4.25: Illustration of the 3-segment concentric tube continuum manipulator kinematics with the joint variables.

$$l_1 = max(q_2 - L_c, 0)$$

$$l_2 = max(q_1 - l_1, 0)$$

$$l_3 = max(q_2 - l_2 - l_1, 0)$$

(4.15)

$$l_4 = max(q_3 - l_3 - l_2 - l_1, 0)$$

L_c is the length of the pre-curved section of the middle tube (tube 2). The curvatures

of overlapping sections k_{123} and k_{23} are:

$$k_{123} = \frac{E_2 I_2 k_2}{E_1 I_1 + E_2 I_2 + E_3 I_3}$$

(4.16)

$$k_{23} = \frac{E_2 I_2 k_2}{E_2 I_2 + E_3 I_3}$$

(4.17)

where E_i is the Young's Modulus of the ith tube (i.e. i=1,2,3, corresponding to outer, middle and inner tubes respectively) and I_i is the cross sectional moment of inertia of the tube. Forward kinematics consists of the series of homogeneous transformations, where the tip coordinate frame is determined with respect to a base frame located at the constrained entry point by:

$$T_{tip} = T_1 T_\theta T_2 T_\alpha T_3 T_\lambda T_4 \tag{4.18}$$

where intermediate transformations are defined as:

$$T_1 = \begin{bmatrix} 1 & 0 & 0 & 0 \\ 0 & 1 & 0 & 0 \\ 0 & 0 & 1 & l_1 \\ 0 & 0 & 0 & 1 \end{bmatrix}$$

$$T_\theta = \begin{bmatrix} cos\theta & -sin\theta & 0 & 0 \\ sin\theta & cos\theta & 0 & 0 \\ 0 & 0 & 1 & 0 \\ 0 & 0 & 0 & 1 \end{bmatrix}$$

$$T_2 = \begin{bmatrix} 1 & 0 & 0 & 0 \\ 0 & \cos(k_{23}l_2) & -\sin(k_{23}l_2) & \frac{\cos(k_{23}l_2)-1}{k_{23}} \\ 0 & \sin(k_{23}l_2) & \cos(k_{23}l_2) & \frac{\sin(k_{23}l_2)}{k_{23}} \\ 0 & 0 & 0 & 1 \end{bmatrix}$$

$$T_\alpha = \begin{bmatrix} 1 & 0 & 0 & 0 \\ 0 & \cos\alpha & -\sin\alpha & 0 \\ 0 & \sin\alpha & \cos\alpha & 0 \\ 0 & 0 & 0 & 1 \end{bmatrix}$$

$$T_3 = \begin{bmatrix} 1 & 0 & 0 & 0 \\ 0 & \cos(k_{123}l_3) & -\sin(k_{123}l_3) & \frac{\cos(k_{123}l_3)-1}{k_{123}} \\ 0 & \sin(k_{123}l_3) & \cos(k_{123}l_3) & \frac{\sin(k_{123}l_3)}{k_{123}} \\ 0 & 0 & 0 & 1 \end{bmatrix}$$

$$T_\lambda = \begin{bmatrix} 1 & 0 & 0 & 0 \\ 0 & \cos\lambda & -\sin\lambda & 0 \\ 0 & \sin\lambda & \cos\lambda & 0 \\ 0 & 0 & 0 & 1 \end{bmatrix}$$

$$T_4 = \begin{bmatrix} 1 & 0 & 0 & 0 \\ 0 & 1 & 0 & 0 \\ 0 & 0 & 1 & l_4 \\ 0 & 0 & 0 & 1 \end{bmatrix} \qquad (4.19)$$

Thus, T_{tip} gives the 6-DOF position and orientation of the tip of the concentric tube robot as a function of the measured actuator configurations: q_1, q_2, q_3 and θ.

4.3.1.3 Inverse Kinematics

To place the tip of the concentric tube robot at a desired target with specific joint configuration, the forward kinematic mapping given must be inverted. To this end, we perform a nonlinear optimization based on the Levenberg-Marquardt algorithm. This enables us to resolve the joint values which minimize the errors between the predicted kinematic model and desired tip position. The predicted tip position are resolved by a uniform 100×100 joint space discretization (middle tube translation $\times$ inner wire translation, i.e. $q_2 \times q_3$), and then computing the predicted tip position at each configuration using the forward kinematics model. Based on the configuration of the robot, the outer tube translation q_1 is a constant value in this study, and middle tube rotation can be calculated geometrically, i.e. $\theta = atan2(x, y)$, where x and y are the elements of needle tip Cartesian position vector. At each configuration, the nonlinear optimization function `lsqnonlin` in Matlab is utilized to resolve the joint

values (overall computation time within 250 milliseconds for 100×100 joint space calculation) that minimizes the errors between the predicted and desired tip position, as well as the residual errors, with predicted joint values as the initial guess of the `lsqnonlin` function. The final solutions of joint values are obtained by choosing the configuration which is the interpolation of multiple closest residual errors among all the configurations.

4.3.2 Experiments and Results

The performance of this robot, primarily the targeting accuracy in three different medium (free space, gelatin phantom and ex vivo tissue), has been studied and is reported in this section. A series of experiments were conducted to systematically demonstrate the capability and error sources of this robotic system.

4.3.2.1 Task Space Accuracy Assessment Utilizing Optical Tracking System

The accuracy of the robot in task space was evaluated using a Polaris (Northern Digital, Ontario, Canada) optical tracking system (OTS). The stated 3D volumetric accuracy of the Polaris is 0.35 mm, and based on our assessment the standard deviation of the readings for a given stable point is 0.10 mm. A 6-DOF passive tracking tool rigid body composed of a circular plate and 3 passive spheres was rigidly mount-

ed on the base of the robot, serving as the global reference during this experiment, i.e. all the data are recorded with respect to this 6-DOF reference frame. One passive sphere is attached at the tip of inner wire of the concentric tube robot to serve as the tip tracking marker of OTS, as shown in Fig. 4.26.
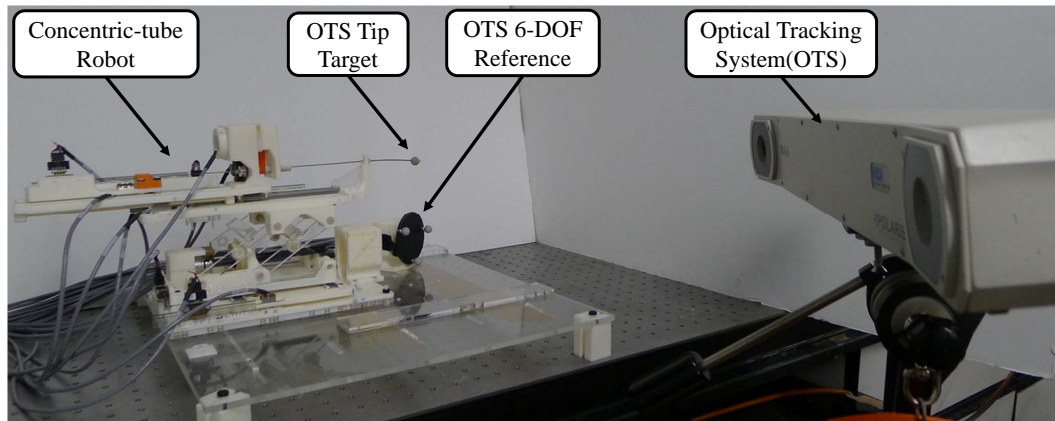
Figure 4.26: The optical tracking system for validation of concentric tube robot kinematics and assessment of free space accuracy.

The concentric tube robot is commanded to 12 targets (3 targets in each of 4 planes) that were specified as virtual points in the coordinate system of fiducial frame on the robot base. The actual tip position is measured by collecting 300 frames at 30 Hz using OTS, with respect to reference frame. The fiducial frame is registered to OTS reference frame via 3 feature points, i.e., the center point, and an arbitrary point in each of the x axis and the z axis of the fiducial frame. Based on these 3 featured points, the fiducial frame can be registered to the reference frame. The accuracy is evaluated by comparing the intended and actual tip position, both in the coordinate system of fiducial frame. The actual tip positions as determined via the OTS system are registered to intended targets with point cloud based registration to isolate the

robot accuracy from registration-related errors in the experiment.

The results obtained from the benchtop evaluation are shown in Fig.4.27, demonstrating RMS error of 1.94 mm and standard deviation of 0.97 mm for the 12 targets, validating the accuracy of the robotic system as well as the kinematics model.
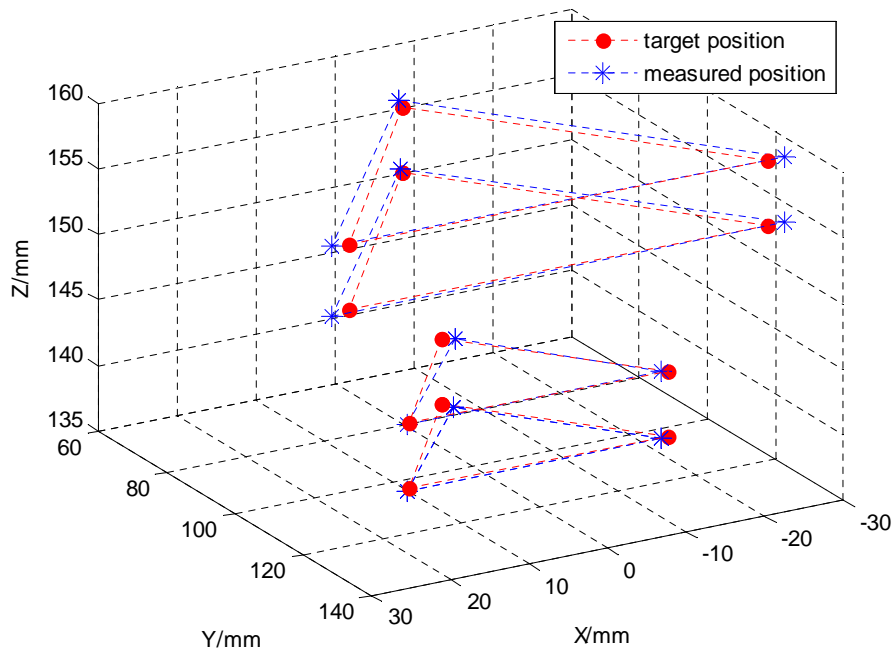
Figure 4.27: Free space evaluation of the accuracy of the active cannula robot. The concentric tube robot was moved to 12 desired points (red circles) in free space and the actual position was measured by the optical tracker (blue stars).

4.3.2.2 MRI-Guided Targeting With Gelatin Phantom

In light of the positioning capability of the robot in free space, the system was further evaluated with image-guided targeting based on desired pixels in the MR image volume. This study was performed in a gelatin phantom. Knox Gelatin (Kraft Foods Global Inc., IL) was mixed with boiling water at a concentration of 3% (by

weight). Soft phantom is utilized in this study, since the concentric tube cannula performs best in soft materials without considering the external load. The phantom was placed on the bed of a 3 Tesla MRI scanner (Philips Achieva, Best, Netherlands) between 2 flex coils to enhance the imaging quality. The robot was placed beside the phantom, and the bed was adjusted to place the phantom at the isocenter of the scanner. The phantom was imaged with a diagnostic T2-weighted fast spin echo protocol (repetition time 800 ms, echo time 11 ms, slice thickness 1.0 mm, 0.9 mm × 0.9 mm pixel size). The robot was commanded to 12 targets that were selected from the 3D MRI images and 70 images slices of the phantom were acquired for each trajectory to verify the trajectory. The actual tip positions as manually segmented in the MR images are registered to desired targets with point cloud based registration to isolate the robot accuracy from registration-related errors in this experiment.

The results from 12 robotic active cannula targeting overlaid with the theoretical model are shown in Fig. 4.29, which demonstrates an RMS error of 2.17 mm and standard deviation of 0.97 mm.

4.3.2.3   Demonstration of Available Redundancy

This concentric tube manipulator can achieve remote center of motion like movement to reach a given target point from various trajectories by utilizing different joint space configurations. With the active cannula, this could be potentially employed to avoid obstacles. To demonstrate this redundancy, a series of experiments

173
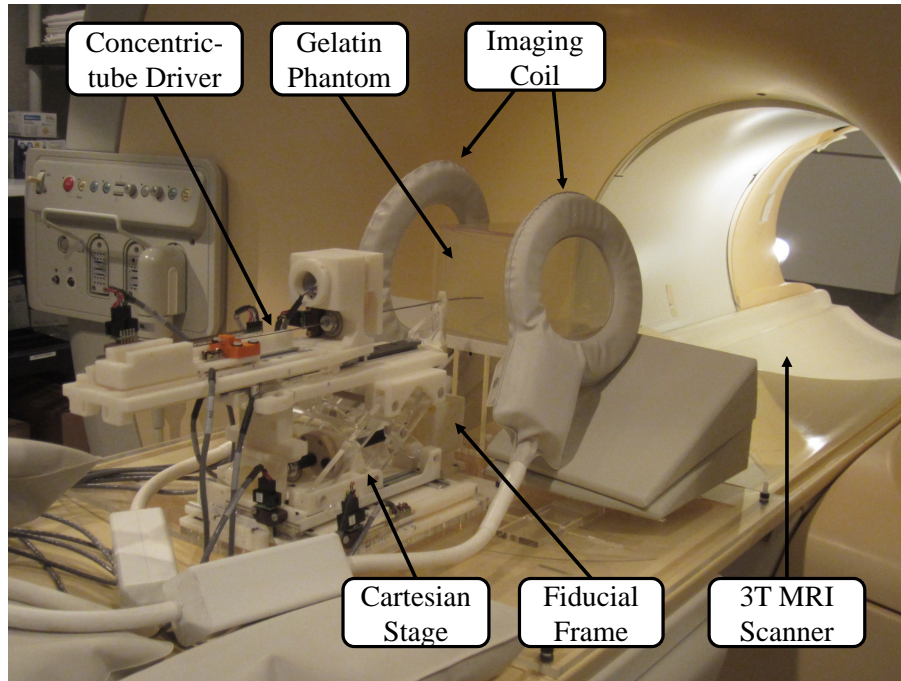
Figure 4.28: The phantom and robot experimental setup illustrating the concentric tube continuum robot at the entrance of the 3T MRI scanner bore.

were conducted in both free space and phantom trials.

Assessment in Free Space

This concept was qualitatively demonstrated based on camera recording and the accuracy in free space quantitatively evaluated by the OTS. An arbitrary target point was selected within the workspace of robot, and 3 solutions of trajectories with different joint configurations were solved based on the inverse kinematics. In these experiments, the rotation angle of middle tube was set to a constant value (90 degrees), i.e. the 3 trajectories are in the same plane. It should be noted that this is intended as an example of the ability to reach a target point from multiple trajectories, and the set of reachable paths includes a full 360 degree rotation. The simulated
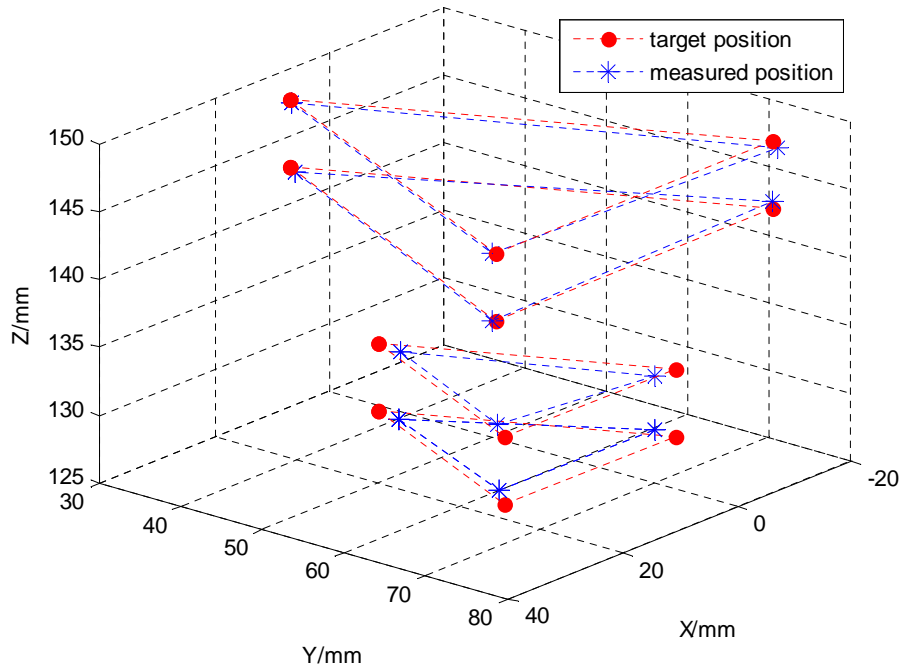
Figure 4.29: MRI-guided multiple-point targeting results inside a gelatin phantom. The concentric tube robot was controlled to move the needle tip to 12 desired points (red circles) in gelatin phantom and the actual position was measured by analyzing acquired MR images (blue stars).

3 trajectories with a common tip position are shown in Fig. 4.30.

To qualitatively demonstrate the concept, a benchtop test was setup with a digital 10.1 mega-pixel CCD camera (Panasonic Lumix DMC-LX5, Japan) rigidly mounted on the top of robot, with lens axis perpendicular to the horizontal plane. A grid paper was used as a reference to qualitatively localize relative tip positions of different trajectories. The robot was commanded to the given target point with 3 solved solutions, and their trajectories were recorded by the camera. The 3 trajectories were overlaid in the same figure shown in Fig. 4.31 to visually illustrate this kinematic redundancy.

175
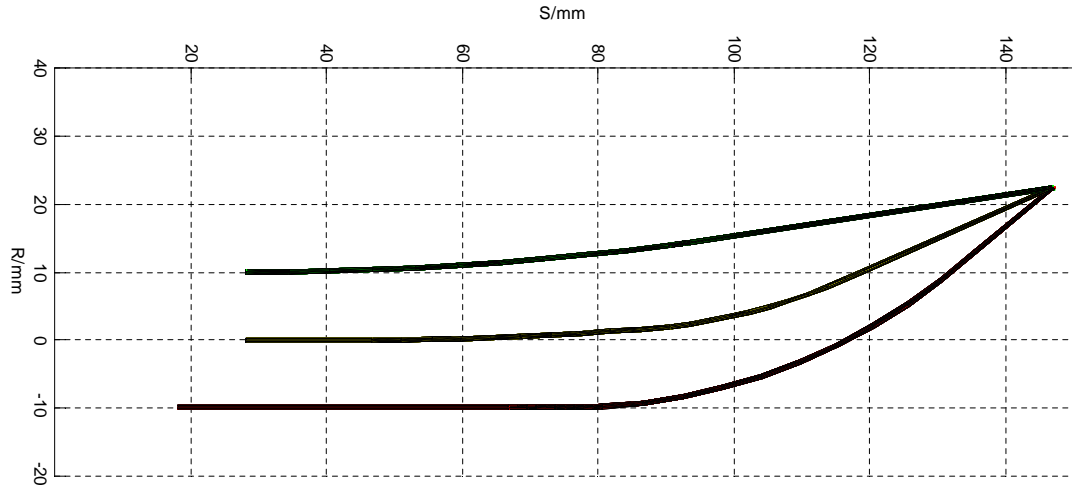
Figure 4.30: Simulation of the remote center of motion like kinematics of the concentric continuum robot. Three needle placement trajectories reach the same target point, achieved by applying different configurations of both the Cartesian base and the concentric tubes.

For a quantitative analysis, using a similar procedure described in Section 4.3.2.1, a spherical tracking marker was attached on the innermost tip of active cannula to record the actual tip position with respect to the 6-DOF reference frame. The robot was commanded to the 3 solved trajectories (the same target position from multiple approach paths), and then the accuracy was evaluated by comparing the theoretical and actual tip positions. The actual tip positions as determined via the OTS system are registered to intended targets with point cloud based registration to isolate the robot accuracy from registration-related errors in the experiment.The experiment demonstrated RMS error of 0.48 mm, and standard deviation of 0.16 mm.

Assessment with Phantom Trials in MRI

This dexterity that can reach the same target with different path due to position
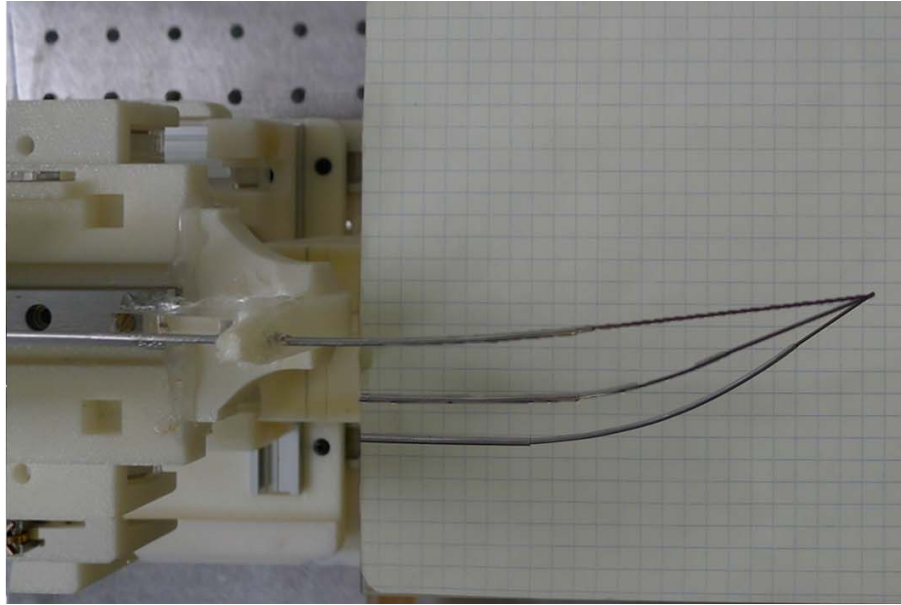
Figure 4.31: Overlaid camera images of three actual robot trajectories targeting the same point from multiple approach trajectories.

kinematic redundancy was evaluated with phantom trials under live MRI guidance. With the same experimental setup as described in Section 4.3.2.2, the active cannula was placed in the soft gelatin phantom to an arbitrary point with 3 different sets of joint configurations, imaged with T2-weighted protocol. Fig. 4.32 shows slices from the 3D MR image volume of the 3 trajectories. The accuracy of tip positions was evaluated by comparing the theoretical (calculated based on the kinematic model) and actual tip positions (determined by the position of the corresponding signal void in each slice) with point cloud based registration to subtract the registration-related errors, which demonstrating RMS error of 0.59 mm, and standard deviation of 0.12 mm in reaching the same point from different paths.
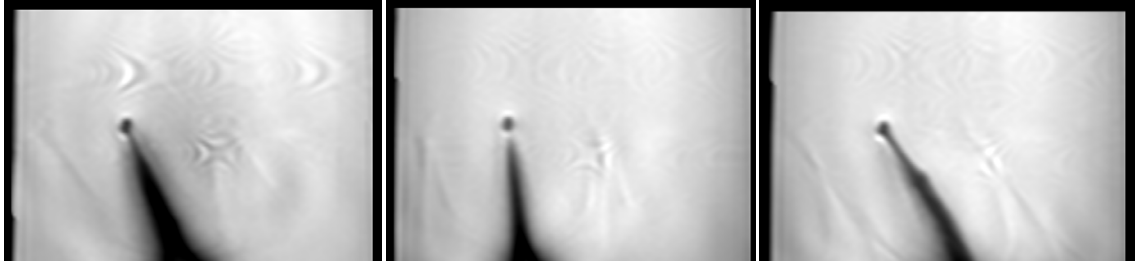
Figure 4.32: MR images of 3 different concentric tube robot needle insertion trajectories to the same target location in the soft gelatin phantom. Inverse kinematics was utilized to reach the same target with different joint space configurations.

4.3.2.4 MRI-Guided Targeting Within Ex Vivo Tissue

An ex vivo liver tissue study was conducted as a demonstration under live MRI guidance. A fresh porcine liver, with approximated dimension of 200 mm × 150 mm × 50 mm was used as the specimen. The specimen was rigidly attached to the phantom frame, which was mounted on the robot base, to reduce the motion of specimen during insertion.

Three targets were selected from the MRI volume, then the concentric tube robot calculated inverse kinematics to command the motors to generate the tube motion to desired reference point. The final path was imaged with T2-weighted fast spin echo protocol (repetition time 800 ms, echo time 11 ms, slice thickness 1.0 mm, 0.9 mm × 0.9 mm pixel size) for accuracy evaluation. Fig. 4.34 shows the MRI image volume for one of the curved trajectories. In this image, 70 axial slices (0.9 mm × 0.9 mm × 1.0 mm voxel size) composed into a 3D volume which is re-sliced into the three orthogonal planes shown. In each set of MRI images, the actual 3D trajectory of the inserted cannula is measured by determining the position of the corresponding signal
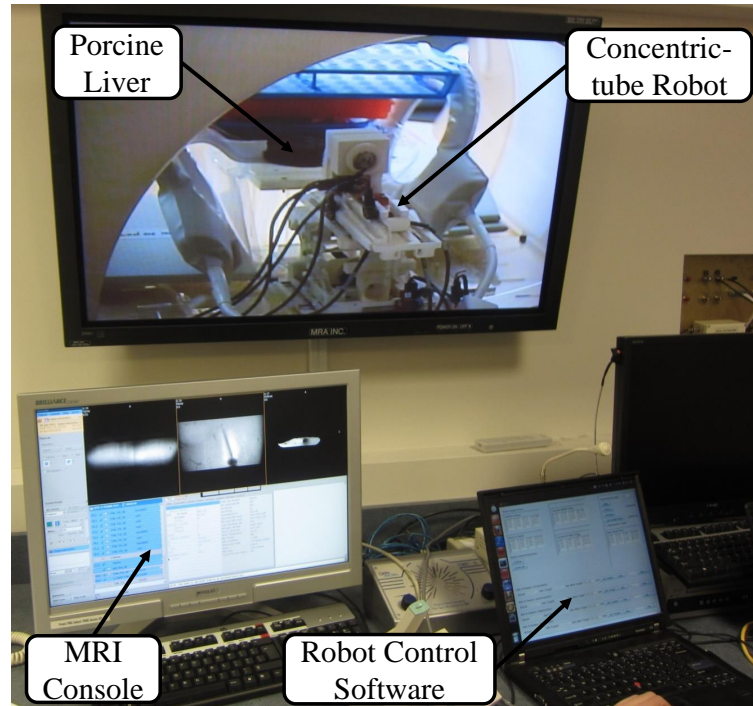
Figure 4.33: Experimental setup for ex vivo tissue evaluation. The interventional robot is inside 3T MRI scanner bore deploying concentric tubes, and the MRI console outside displaying the live MR image of the curved path.

void in each slice.

Fig. 4.35 shows the three curved trajectories to reach targets in the ex vivo tissue and red spheres indicate the desired positions. For a quantitative evaluation, Table 4.4 shows the needle placement error in terms of the desired position in MRI and the manually segmented actual needle tip position. The actual tip positions are registered to desired targets with point cloud based registration to isolate the robot accuracy from registration-related system errors. The Cartesian positioning errors of the three trajectories are: 3.79 mm, 2.87 mm, and 6.48 mm, respectively. Clinically, there is no consensus about the targeting accuracy standard depending on different organ interventions and treatment methods. But roughly, it is agreed that 1 cm or ideally
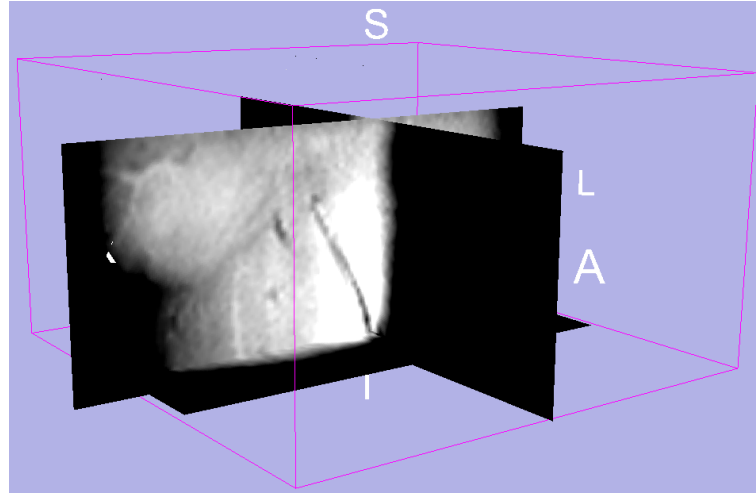
Figure 4.34: Volumetric MR image showing a representative active cannula path inserted into a ex vivo liver by the robot inside the MRI scanner. The cannula is inserted along the I-S direction (vertical in this figure) and is shown in the coronal plane along with additional two cross-sectional planes.

5 mm accuracy (e.g. 5 mm is the grid spacing of prostate biopsy guide template) is

satisfactory.

Table 4.4: Accuracy Assessment of MRI-Guided Needle Placement to 3 Targets Inside An Ex Vivo Liver Tissue.

No	Target Position[mm]			Final Tip Position[mm]			Error[mm]			Total Error[mm]	In-plane(RA) Error[mm]
	R	A	S	R	A	S	R	A	S		
1	34.79	63.31	138.17	31.13	63.30	137.19	3.66	0.01	0.98	3.79	3.66
2	34.04	63.23	130.00	31.94	63.20	128.04	2.10	0.03	1.96	2.87	2.10
3	2.10	63.10	118.77	7.87	63.14	121.71	-5.77	-0.04	2.94	6.48	5.77
RMS Mean							4.13	0.03	2.12	4.64	4.12
Standard deviation							5.05	0.04	2.59	1.87	1.84

Note: R, A and S are the coordinates of the needle tip, while RA plane corresponds to axial plane in MRI scanner coordinate system.
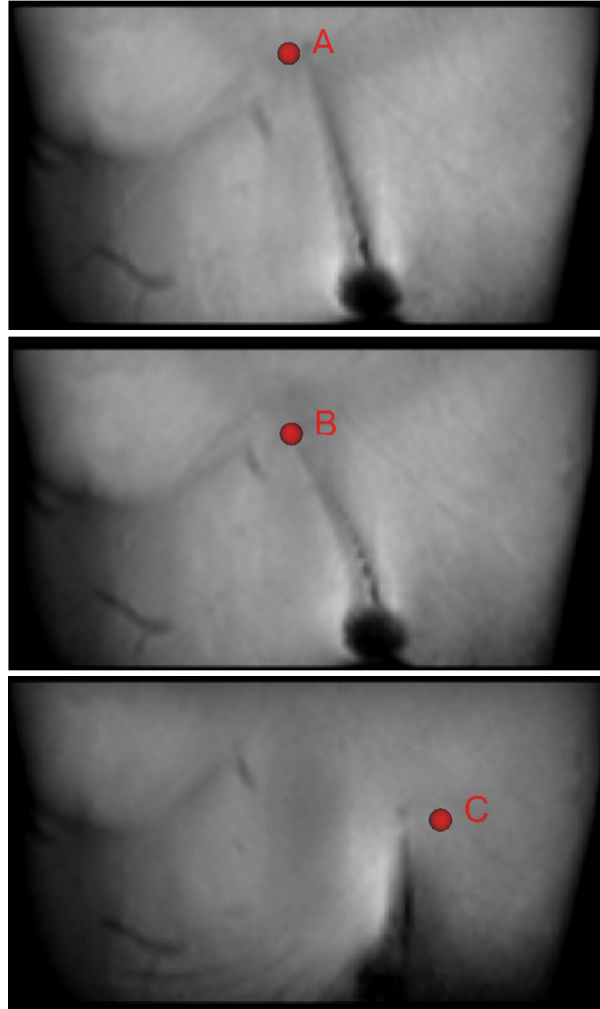
Figure 4.35: Ex vivo tissue results showing three different selected targets (red spheres) and the corresponding needle trajectory and needle tip location on axial TSE T2 weighted MR images.

4.4 Discussion and Conclusion

This chapter presents the modeling and control of two approaches of steerable needle intervention, i.e. asymmetric tip steerable needle and concentric-tube continuum cannula. Combing the mechanism of steerable needle with advanced MRI guidance modality, it enables the image-guided technologies for minimally invasive surgery

where narrow and winding intervention pathway are required.

Asymmetric Tip Steerable Needle

In the first section, we propose a novel needle steering model that enables effective control of variable curvature with Gaussian-based continuous rotation, while decoupling control of the insertion and rotation axes. Variable curvature control enhances the controllability by providing multiple and flexible options compared to discrete maximum curvature. In contrast to duty-cycled approach, CURV steering model possess following merits: 1) Continuous rotation potentially attenuate static frictional effects that present on the needle during pure insertion; 2) smooth motion transition could reduce the strain on actuation system, and alleviate the electro-magnetic noise during MR imaging procedures; 3) Decoupling the control of insertion from rotation readily enables active control of the needle path for the applications that precise coordination of insertion and rotation is rarely possible. A major potential application of the CURV steering model is to be integrated with teleoperated insertion such as the robotic system developed in our previous work [97], to implement active compensation for needle placement error. The comparison of the CURV steering model and duty-cycled approach is summarized in Table. 4.5. The validation of the CURV steering model is conducted with experimental phantom studies in 2D with camera images and in 3D with CT images. The experiment results demonstrate that the proposed CURV steering model is able to produce preplanned needle trajectories with realistic curvatures for clinical applications. The RMS errors of trajectory accuracy

are less than 1.5 mm in both 2D plane and 3D space.

Table 4.5: Comparison of CURV and Duty-Cycled Approach

	Duty-cycled Spinning	Gaussian-based CURV Steering	Advantages of CURV
Rotation Profile	Duty-cycle	Continuous Gaussian distribution	Attenuate static friction
Rotation Transition	Sharp step transition	Smooth transition	Reduce strain on actuation system; Alleviate EMI noise during MRI
Insertion	Precisely coordinated with rotation	Independent control from rotation	Enable shared autonomy

Imaged-based closed-loop control of CURV steering model is presented to compensate and correct the modeling error during procedures. Phantom experiments were performed using continuously acquired live MR images as position feedback, demonstrating 0.75 mm RMS error. Compared to the results that were achieved in our previous study which utilizes only maximum and straight curvature (total error 2.50 mm) [96], it indicates the benefits of variable curvature control of the proposed CURV steering model. The targeting accuracy is better than the image-guided system which is build upon the same nonholonomic kinematic model (positioning error 4 mm) [106] and the semi-automatic needle steering system which uses duty-cycled approach (positioning error 2.8 mm) [107]. Although MRI-based needle tracking is utilized in this study, this approach is applicable to various imaging modalities such as CT and Ultrasound. The error sources include imager error (camera, CT, or MR image resolution, and calibration error), manipulator placement error (backlash, robot alignment,

and actuation error), and unmodeled interaction forces between the phantom and the steerable needle. The unmodeled interaction forces have been reported to cause significant placement errors, which could be classified as torsional friction [108], translational friction [109], and tissue motion [110]. Further improvement of the steering model is to implement needle-tissue interaction compensation.

Although rotating the needle continuously during insertion is able to effectively adjust the curvature, it may cause damage to the tissue surrounding the needle. Even though it is not yet verified if the tissue damage incurred by the needle is clinically significant, it would be beneficial to reduce the damage. Custom design of the asymmetric-tip needle might be adopted in future work to minimize the tissue damage while achieving high steering capabilities, such as the flexure-based needle design presented in [111]. Homogenous gelatin phantom is utilized in this study to demonstrate the viability of the CURV steering model. The model parameters may be different when varying designs of needle and properities of phantom/tissue are utilized. The model parameters could be experimentally calibrated regarding to a specific needle tissuse configuration. Even though there may be modeling errors, the image-based closed-loop control approach could be able to correct the errors on the fly. This study demonstrates the potential to use image-based closed-loop control of CURV steering to avoid obstacles. A simple solution is to set an intermediate target on the desired path and closed to obstacle to implement obstacle bypassing. However, further studies on the high level motion planning are required to implement trajetory

optimization, especially in terms of motion constraints, which is beyond the scope of this study.

Concentric Tube Continuum Cannula

In the second section, we present the kinematic modeling and accuracy evaluation of the MRI-guided concentric tube continuum robot. The targeting capability of the system in free space was accomplished with an RMS error of 1.96 mm. The closed-loop targeting capability of the system was further evaluated in soft gelatin phantom under live MRI guidance with an RMS error of 2.18 mm. Compared with the results in free space, small additional errors are introduced by the interaction force with the external medium (i.e. gelatin phantom) and the ability to detect needle artifact in MRI image. While for the ex vivo tissue interventional procedures under the same MRI image sequence, the RMS error of 4.64 mm is mostly due to the interaction force with the external medium, i.e. porcine liver, which is relatively large compared to that of the soft gelatin phantom. This obviously imposes challenges in in vivo needle placement and targeting.

Our proposed image-guided closed-loop control method only utilizes MRI to define targets and evaluate targeting accuracy. To further utilize the imaging capability of MRI, one effort from our group is to dynamically scan, track and align imaging plane to visualize the needle trajectory for closed-loop control of needle tip motion [96]. We envision that the same imaging technique can be extended from a bevel-tip needle steering scenario [96] to the concentric tube robot applications. Future research will

focus on improving accuracy of the kinematic model by integrating frictional force and compensating the interaction force with tissue.

Asymmetric-tip needle is driven by the external asymmetric force between the tip and tissue. Therefore it could be made in compact dimension and is suitable for insertions withins soft tissue. While the bending force of concentric tube continuum cannula is derived from elastic tube interaction in the backbone itself, not from the external needle-tissue interaction. Therefore it could be more dexterous and suitable for open space procedures, such as endonasal surgery etc.

Chapter 5

Conclusions

This dissertation explored the research topics related to developing and modeling of robotic system for intraoperative MRI-guided interventions. The system is developed based on a modular design approach, making it readily transported and setup for supporting clinical workflow of MRI-guided procedures, as well as readily extensible and reconfigurable to other clinical applications. Stereotactic neurosurgery and prostate cancer therapy are studied as the primary clincial applications for this system. A conclusion of this work is presented below with an extension of future work.

5.1   Summary of Work and Contributions

Robotic System for MRI-Guided Stereotactic Neurosurgery

Designed two generations of novel robot mechanism that is compatible with high

field MRI environment, with deep brain stimulation and brain tumor ablation as two primary clinical applications. Proposed the robot-assisted clinical work and demonstrated the potential to reduce conventional procedure time. Developed an integrated actuation, control, sensing and navigation system for robot-assisted MRI-guided interventions. Evaluated image quality benchmark of the robotic system, and targeting accuracy of the system in free space and under MRI-guidance.

Robotic System for MRI-Guided Transperineal Prostate Interventions

Developed a fully integrated robotic system for MRI-guided transperineal prostate biopsy, which has been approved by IRB for clinical trials. The clinically oriented robotic system described in chapter 3 is developed based on a modular approach, with the modules connected through a network. Safety is a crucial requirement for a clinical system; therefore, even in the case of robot failure, safety mechanisms are considered during the design phases. Sterility is a unique and critical requirement for clinical devices; for this reason the robot manipulator is designed with non-sterilizable and sterilizable components. The clinical grade system has been evaluated with preclinical MRI phantom studies and preliminary patient studies. More extensive clinical cases are currently ongoing at BWH.

Prototype version of fully actuated robotic system has been further studied for automatically deploy the needle, overcoming potential limitations of manual insertion by allowing the clinician to control the robot from beside the patient but outside the tightly constrained bore.

Steerable Needle Interventions

Proposed a novel needle steering model that enables effective control of variable curvature with Gaussian-based continuous rotation, while decoupling the control of insertion and rotation axes. Variable curvature control enhances the controllability by providing multiple and flexible options compared to discrete maximum curvature. The validation of the CURV steering model is conducted with experimental phantom studies in 2D with camera images and in 3D with CT images. Imaged-based closed-loop control of CURV steering model is presented to compensate and correct the modeling error during procedures. Phantom experiments were performed using continuously acquired live MR images as position feedback.

Integrated the concentric tube continuum robotics with advanced MRI-guidance techniques. The system enables MRI-guided deployment of a precurved and steerable concentric tube continuum mechanism, and is suitable for clinical applications where a curved trajectory is needed. Demonstrated available redundancy of MRI-guided concentric tube continuum robot. Assessed the system accuracy with MRI phantom and ex vivo tissue studies.

5.2 Impact and Lessons Learned

Impact

The system developed in this work is based on modular design approach, comprised

189

of surgical navigation user interface, robot control software, MRI robot controller, and needle placement manipulator, with all modules connected through network-based communication media. A major merit of network based modular design approach is that each module can be developed and tested individually, making it readily transported and setup for supporting clinical workflow of MRI-guided procedures, as well as readily extensible and reconfigurable to many other clinical applications. MRI's broad spectrum of imaging options including thermometry, diffusion, spectroscopy, oxygenation, and flow can be incorporated into the intraoperative plan.

The novel needle steering model proposed in this work opens the doors to many possibilities for minimally invasive therapy, where specified paths with preplanned curves are required to avoid anatomical obstacles (e.g. delicate organs, vasculature, nerves, and bones) or compensate for placement errors. Incorporated with intraoperative continuous MRI enables the technologies for closed-loop control with dynamic position feedback, which could compensate and correct the modeling error during procedures.

Lessons Learned

The first and most important lesson learned from this work is to know the real needs and requirements. The development of medical robotics is highly relying on the inputs from the users, i.e. the clinicians. There is commonly a misalignment between the real needs of clinicians and the actual solutions proposed by the engineers. Regarding to the development of robotic system for prostate biopsy, fully-actuated robotic devices

may seem to be an excellent engineering solution. But taking account of the safety, FDA regulations, and the clinical workflow, robot-assisted alignment with manual insertion is in fact a practical and feasible solution to start with. With this in mind, the first step of developing the robotic system is thorough analyzing the needs and requirements. The robotic systems developed in this study are closely collaborated with clinical teams. Clinical requirements are analyzed in the iterative design process, and thorough pre-clinical studies are performed to validate the accuracy, clinical workflow and safety mechanism.

The other important lesson learned in this study is to make technologies transferable and extensible. Developing the infrastructure usually takes significant efforts, cost and time. It would have substantial benefits to transfer and extent the developed framework to widespread applications. Modular design approach is adopted in this study, and reconfigured to support all the research platform for varying application, i.e. stereotactic neurosurgery, prostate cancer therapy, and steerable needle interventions. It is also readily extensible to many other Image-guided clinical applications, such as liver ablation, percutaneous kidney intervention and etc.

5.3   Future Work

The system framework developed in this study have been approved to perform clinical trials for MRI-guided prostate biopsy with manual insertion and first-in human

trials to evaluate the system's effectiveness and accuracy for MR image-guide prostate biopsy are underway. The hardware development for robotic system has been mostly set solid foundation. However, for the fully actuated prostate intervention and more complex neurosurgery, further evaluation and improvement are required to advance for clinical trials on human, especially in the aspects of clinical workflow design, safety mechanism, and sterilization. Phantom studies have been conducted in this work, validating the feasibility of the proposed robotic system. But, for in-vivo interventions, the inhomogeneity and tissue interaction force may cause needle placement errors. Hence, thorough pre-clinical evaluations, i.e. ex-vivo and cadaver experiments, etc., would be a necessary step in the future.

Regarding to the brain tumor ablation, one essential future work is temperature and thermal dose monitoring through MR thermal imaging (MRTI). MRTI could be used to provide real-time feedback for modifying the treatment power and directional control parameters as the ablation progresses, which is the key part to the outcome and safety of the procedures.

In terms of steerable needle interventions, one potential research area is dynamics modeling and compensation. Kinematics model is studied in this work and proved to obtain acceptable results. However, placement errors are observed due to the torsional friction. Modeling of the dynamic effect on the steerable interventions could be effective to improve the needle deployment accuracy.

References

[1] F. A. Jolesz, "Invited. Interventional and intraoperative MRI: A general overview of the field," *Journal of Magnetic Resonance Imaging*, vol. 8, no. 1, pp. 3–7, 1998.

[2] R. Gassert, R. Moser, E. Burdet, and H. Bleuler, "MRI/fMRI-compatible robotic system with force feedback for interaction with human motion," *Mechatronics, IEEE/ASME Transactions on*, vol. 11, no. 2, pp. 216–224, 2006.

[3] G. S. Fischer, I. Iordachita, C. Csoma, J. Tokuda, S. P. DiMaio, C. M. Tempany, N. Hata, and G. Fichtinger, "MRI-compatible pneumatic robot for transperineal prostate needle placement," *IEEE/ASME Transactions on Mechatronics*, vol. 13, no. 3, pp. 295–305, 2008.

[4] S. Song, N. Hata, I. Iordachita, G. Fichtinger, C. Tempany, and J. Tokuda, "A workspace-orientated needle-guiding robot for 3T MRI-guided transperineal prostate intervention: evaluation of in-bore workspace and MRI compatibility," *The International Journal of Medical Robotics and Computer Assisted Surgery*, vol. 9, no. 1, pp. 67–74, 2013.

[5] M. R. Van den Bosch, M. R. Moman, M. Van Vulpen, J. J. Battermann, E. Duiveman, L. J. van Schelven, H. de Leeuw, J. J. Lagendijk, and M. A. Moerland, "MRI-guided robotic system for transperineal prostate interventions: proof of principle," *Physics in medicine and biology*, vol. 55, no. 5, p. N133, 2010.

[6] D. Stoianovici, A. Patriciu, D. Petrisor, D. Mazilu, and L. Kavoussi, "A new type of motor: Pneumatic step motor," *Mechatronics, IEEE/ASME Transactions on*, vol. 12, no. 1, pp. 98–106, 2007.

[7] D. Stoianovici, C. Kim, G. Srimathveeravalli, P. Sebrecht, D. Petrisor, J. Coleman, S. B. Solomon, and H. Hricak, "MRI-safe robot for endorectal prostate biopsy," *IEEE/ASME Transactions on Mechatronics*, no. 99, pp. 1–11, 2013.

[8] D. Stoianovici, D. Song, D. Petrisor, D. Ursu, D. Mazilu, M. Muntener, M. Mutener, M. Schar, and A. Patriciu, "MRI Stealth robot for prostate interventions." *Minim Invasive Ther Allied Technol*, vol. 16, no. 4, pp. 241–248, 2007.

[9] M. G. Schouten, J. Ansems, W. K. J. Renema, D. Bosboom, T. W. Scheenen, and J. J. Fütterer, "The accuracy and safety aspects of a novel robotic needle guide manipulator to perform transrectal prostate biopsies," *Medical physics*, vol. 37, no. 9, pp. 4744–4750, 2010.

[10] D. Yakar, M. G. Schouten, D. G. H. Bosboom, J. O. Barentsz, T. W. J. Scheenen, and J. J. Futterer, "Feasibility of a pneumatically actuated MR-compatible robot for transrectal prostate biopsy guidance," *Radiology*, vol. 260, no. 1, pp. 241–247, 2011.

[11] S. Zangos, C. Herzog, K. Eichler, R. Hammerstingl, A. Lukoschek, S. Guthmann, B. Gutmann, U. J. Schoepf, P. Costello, and T. J. Vogl, "MR-compatible assistance system for punction in a high-field system: device and feasibility of transgluteal biopsies of the prostate gland," *Eur Radiol*, vol. 17, no. 4, pp. 1118–1124, Apr 2007.

[12] S. Zangos, A. Melzer, K. Eichler, C. Sadighi, A. Thalhammer, B. Bodelle, R. Wolf, T. Gruber-Rouh, D. Proschek, R. Hammerstingl *et al.*, "MR-compatible assistance system for biopsy in a high-field-strength system: initial results in patients with suspicious prostate lesions," *Radiology*, vol. 259, no. 3, pp. 903–910, 2011.

[13] S. Song, J. Tokuda, K. Tuncali, C. M. Tempany, E. Zhang, and N. Hata, "Development and preliminary evaluation of a motorized needle guide template for MRI-guided targeted prostate biopsy," *Biomedical Engineering, IEEE Transactions on*, vol. 60, no. 11, pp. 3019–3027, 2013.

194

[14] A. Krieger, S. Song, N. B. Cho, I. I. Iordachita, P. Guion, G. Fichtinger, and L. L. Whitcomb, "Development and evaluation of an actuated MRI-compatible robotic system for MRI-guided prostate intervention," *Mechatronics, IEEE/ASME Transactions on*, vol. 18, no. 1, pp. 273–284, 2013.

[15] G. S. Fischer, A. Krieger, I. Iordachita, C. Csoma, L. L. Whitcomb, and G. Fichtinger, "MRI compatibility of robot actuation techniques–a comparative study," in *International Conference on Medical Image Computing and Computer-Assisted Intervention.* Springer, 2008, pp. 509–517.

[16] V. Duindam, J. Xu, R. Alterovitz, S. Sastry, and K. Goldberg, "Three-dimensional motion planning algorithms for steerable needles using inverse kinematics," *The International Journal of Robotics Research*, vol. 29, no. 7, pp. 789–800, 2010.

[17] J. A. Engh, D. S. Minhas, D. Kondziolka, and C. N. Riviere, "Percutaneous intracerebral navigation by duty-cycled spinning of flexible bevel-tipped needles," *Neurosurgery*, vol. 67, no. 4, pp. 1117–1123, 2010.

[18] K. Masamune, E. Kobayashi, Y. Masutani, M. Suzuki, T. Dohi, H. Iseki, and K. Takakura, "Development of an MRI-compatible needle insertion manipulator for stereotactic neurosurgery," *Journal of Image Guided Surgery*, vol. 4, pp. 242–248, 1995.

[19] G. R. Sutherland, I. Latour, and A. D. Greer, "Integrating an image-guided robot with intraoperative MRI," *Engineering in Medicine and Biology Magazine, IEEE*, vol. 27, no. 3, pp. 59–65, 2008.

[20] D. B. Comber, E. J. Barth, and R. J. Webster, "Design and control of an magnetic resonance compatible precision pneumatic active cannula robot," *Journal of Medical Devices*, vol. 8, no. 1, p. 011003, 2014.

[21] M. Ho, A. McMillan, J. Simard, R. Gullapalli, and J. Desai, "Toward a mesoscale SMA-actuated MRI-compatible neurosurgical robot," *Robotics, IEEE Transactions on*, vol. 28, no. 1, pp. 213 –222, Feb. 2012.

[22] M. Lang, A. Greer, and G. Sutherland, "Intra-operative robotics: NeuroArm," *Intraoperative Imaging*, vol. 109, pp. 231–236, 2011.

[23] B. Yang, U. Tan, A. McMillan, R. Gullapalli, and J. Desai, "Design and Control of a 1-DOF MRI-compatible pneumatically actuated robot with long transmission lines," *Mechatronics, IEEE/ASME Transactions on*, vol. 16, no. 6, pp. 1040 –1048, 2011.

[24] H. Liao, T. Inomata, I. Sakuma, and T. Dohi, "3-D augmented reality for MRI-guided surgery using integral videography autostereoscopic image overlay," *Biomedical Engineering, IEEE Transactions on*, vol. 57, no. 6, pp. 1476–1486, June 2010.

[25] N. Hirai, A. Kosaka, T. Kawamata, T. Hori, and H. Iseki, "Image-guided neurosurgery system integrating AR-based navigation and open-MRI monitoring," *Computer Aided Surgery*, vol. 10, no. 2, pp. 59–72, 2005.

[26] R. J. Webster III, J. S. Kim, N. Cowan, G. Chirikjian, and A. Okamura, "Nonholonomic modeling of needle steering," *International Journal of Robotics Research*, vol. 25, no. 5-6, pp. 509–25, 2006.

[27] T. R. Wedlick and A. M. Okamura, "Characterization of pre-curved needles for steering in tissue," in *Engineering in Medicine and Biology Society, 2009. EMBC 2009. Annual International Conference of the IEEE*. IEEE, 2009, pp. 1200–1203.

[28] D. C. Rucker, R. J. Webster, G. S. Chirikjian, and N. J. Cowan, "Equilibrium conformations of concentric-tube continuum robots," *The International Journal of Robotics Research*, 2010.

[29] P. Dupont, J. Lock, B. Itkowitz, and E. Butler, "Design and control of concentric-tube robots," *Robotics, IEEE Transactions on*, vol. 26, no. 2, pp. 209 –225, april 2010.

[30] F. O. M. Joseph, M. Kumar, K. Franz, B. Konh, P. Hutapea, Y.-J. Zhao, A. P. Dicker, Y. Yu, and T. K. Podder, "Control of shape memory alloy actuated flexible needle using multimodal sensory feedbacks," *Journal of Automation and Control Engineering Vol*, vol. 3, no. 5, 2015.

[31] E. Ayvali and J. P. Desai, "Accurate in-plane and out-of-plane ultrasound-based tracking of the discretely actuated steerable cannula," in *Robotics and*

Automation (ICRA), 2015 IEEE International Conference on. IEEE, 2015, pp. 5896–5901.

[32] S. C. Ryu, Z. F. Quek, J.-S. Koh, P. Renaud, R. J. Black, B. Moslehi, B. L. Daniel, K.-J. Cho, and M. R. Cutkosky, "Design of an Optically Controlled MR-Compatible Active Needle," *Robotics, IEEE Transactions on*, vol. 31, no. 1, pp. 1–11, 2015.

[33] R. J. Roesthuis, N. J. van de Berg, J. J. van den Dobbelsteen, and S. Misra, "Modeling and steering of a novel actuated-tip needle through a soft-tissue simulant using fiber bragg grating sensors," in *Robotics and Automation (ICRA), 2015 IEEE International Conference on.* IEEE, 2015, pp. 2283–2289.

[34] D. Glozman and M. Shoham, "Image-guided robotic flexible needle steering," *Robotics, IEEE Transactions on*, vol. 23, no. 3, pp. 459 –467, jun. 2007.

[35] S. P. DiMaio and S. E. Salcudean, "Needle steering and motion planning in soft tissues," *Biomedical Engineering, IEEE Transactions on*, vol. 52, no. 6, pp. 965–974, June 2005.

[36] V. G. Mallapragada, N. Sarkar, and T. K. Podder, "Robot-assisted real-time tumor manipulation for breast biopsy," *Robotics, IEEE Transactions on*, vol. 25, no. 2, pp. 316–324, 2009.

[37] J. A. Engh, G. Podnar, D. Kondziolka, and C. N. Riviere, "Toward effective needle steering in brain tissue," in *Engineering in Medicine and Biology Society, 2006. EMBS'06. 28th Annual International Conference of the IEEE.* IEEE, 2006, pp. 559–562.

[38] S. Y. Ko, L. Frasson, and F. Rodriguez y Baena, "Closed-loop planar motion control of a steerable probe with a programmable bevel inspired by nature," *Robotics, IEEE Transactions on*, vol. 27, no. 5, pp. 970–983, 2011.

[39] N. J. Cowan, K. Goldberg, G. S. Chirikjian, G. Fichtinger, R. Alterovitz, K. B. Reed, V. Kallem, W. Park, S. Misra, and A. M. Okamura, "Robotic needle steering: design, modeling, planning, and image guidance," in *Surgical Robotics*. Springer, 2011, pp. 557–582.

[40] N. Abolhassani, R. Patel, and M. Moallem, "Needle insertion into soft tissue: A survey," *Medical engineering & physics*, vol. 29, no. 4, pp. 413–431, 2007.

[41] G. Li, H. Su, G. Cole, W. Shang, K. Harrington, A. Camilo, J. G. Pilitsis, G. S. Fischer *et al.*, "Robotic System for MRI-Guided Stereotactic Neurosurgery," *Biomedical Engineering, IEEE Transactions on*, vol. 62, no. 4, pp. 1077–1088, 2015.

[42] T. Hartkens, D. Hill, A. Castellano-Smith, D. Hawkes, C. Maurer, A. Martin, H. Liu, and C. Truwit, "Measurement and analysis of brain deformation during neurosurgery," *Medical Imaging, IEEE Transactions on*, vol. 22, pp. 82–92, 2003.

[43] P. A. Starr, A. J. Martin, J. L. Ostrem, P. Talke, N. Levesque, and P. S. Larson, "Subthalamic nucleus deep brain stimulator placement using high-field interventional magnetic resonance imaging and a skull-mounted aiming device: technique and application accuracy," *Journal of Neurosurgery*, vol. 112, no. 3, pp. 479–490, 2010.

[44] P. Larson, P. A. Starr, J. L. Ostrem, N. Galifianakis, M. S. L. Palenzuela, and A. Martin, "203 application accuracy of a second generation interventional MRI stereotactic platform: initial experience in 101 DBS electrode implantations," *Neurosurgery*, vol. 60, p. 187, 2013.

[45] D. T. Gering, A. Nabavi, R. Kikinis, N. Hata, L. J. O'Donnell, W. E. L. Grimson, F. A. Jolesz, P. M. Black, and W. M. Wells, "An integrated visualization system for surgical planning and guidance using image fusion and an open MR," *Journal of Magnetic Resonance Imaging*, vol. 13, no. 6, pp. 967–975, 2001.

[46] J. Tokuda, G. S. Fischer, X. Papademetris, Z. Yaniv, L. Ibanez, P. Cheng, H. Liu, J. Blevins, J. Arata, A. J. Golby *et al.*, "Openigtlink: an open network protocol for image-guided therapy environment," *The International Journal of Medical Robotics and Computer Assisted Surgery*, vol. 5, no. 4, pp. 423–434, 2009.

[47] R. H. Taylor, A. Menciassi, G. Fichtinger, and P. Dario, "Medical robotics and

computer-integrated surgery," in *Springer handbook of robotics.* Springer, 2008, pp. 1199–1222.

[48] Y. Wang and J. Sackier, "Robotically enhanced surgery: from concept to development," *Surg Endosc*, vol. 8, pp. 63–6, 1996.

[49] H. Reichenspurner, R. J. Damiano, M. Mack, D. H. Boehm, H. Gulbins, C. Detter, B. Meiser, R. Ellgass, and B. Reichart, "Use of the voice-controlled and computer-assisted surgical system zeus for endoscopic coronary artery bypass grafting," *The Journal of thoracic and cardiovascular surgery*, vol. 118, no. 1, pp. 11–16, 1999.

[50] G. Guthart and J. K. Salisbury Jr, "The intuitivetm telesurgery system: Overview and application." in *ICRA.*   Citeseer, 2000, pp. 618–621.

[51] D. Stoianovici, L. L. Whitcomb, J. H. Anderson, R. H. Taylor, and L. R. Kavoussi, "A modular surgical robotic system for image guided percutaneous procedures," in *Medical Image Computing and Computer-Assisted InterventationMICCAI98.*   Springer, 1998, pp. 404–410.

[52] R. H. Taylor, J. Funda, B. Eldridge, S. Gomory, K. Gruben, D. LaRose, M. Talamini, L. Kavoussi, and J. Anderson, "A telerobotic assistant for laparoscopic surgery," *Engineering in Medicine and Biology Magazine, IEEE*, vol. 14, no. 3, pp. 279–288, 1995.

[53] R. H. Taylor and D. Stoianovici, "Medical robotics in computer-integrated surgery," *Robotics and Automation, IEEE Transactions on*, vol. 19, no. 5, pp. 765 –781, Oct. 2003.

[54] G. A. Cole, J. G. Pilitsis, and G. S. Fischer, "Design of a robotic system for MRI-guided deep brain stimulation electrode placement," in *IEEE Int Conf on Robotics and Automation*, May 2009.

[55] J. W. Young, "Head and face anthropometry of adult US civilians," *Technical Information Center Document*, 1993.

[56] G. A. Cole, K. Harrington, H. Su, A. Camilo, J. G. Pilitsis, and G. S. Fischer, "Closed-loop actuated surgical system utilizing real-time in-situ MRI guidance," in *Experimental Robotics.* Springer, 2014, pp. 785–798.

[57] W. Shang and G. S. Fischer, "A high accuracy multi-image registration method for tracking MRI-guided robots," in *SPIE Medical Imaging*, February 2012.

[58] *Determination of Signal-to-Noise Ratio (SNR) in Diagnostic Magnetic Resonance Imaging, NEMA Standard Publication MS 1-2008.* The Association of Electrical and Medical Imaging Equipment Manufacturers, 2008.

[59] H. Elhawary, A. Zivanovic, M. Rea, B. Davies, C. Besant, D. McRobbie, N. de Souza, I. Young, and M. Lamprth, "The feasibility of MR-image guided prostate biopsy using piezoceramic motors inside or near to the magnet isocentre," *International Conference on Medical Image Computing and Computer Assisted Intervention (MICCAI)*, vol. 9, pp. 519–526, 2006.

[60] A. Krieger, S. Song, N. Cho, I. Iordachita, P. Guion, G. Fichtinger, and L. Whitcomb, "Development and evaluation of an actuated MRI-compatible robotic system for MRI-guided prostate intervention," *Mechatronics, IEEE/ASME Transactions on*, vol. 18, no. 1, pp. 273–284, 2013.

[61] G. Fischer, G. Cole, and H. Su, "Approaches to creating and controlling motion in MRI," in *Engineering in Medicine and Biology Society, EMBC, Annual International Conference of the IEEE*, 2011, pp. 6687–6690.

[62] G. Ghoshal, V. Salgaonkar, J. Wooton, E. Williams, P. Neubauer, L. Frith, B. Komadina, C. Diederich, and E. C. Burdette, "Ex-vivo and simulation comparison of multi-angular ablation patterns using catheter-based ultrasound transducers," in *SPIE BiOS.* International Society for Optics and Photonics, 2013, pp. 85 840Y–85 840Y.

[63] S. J. Scott, P. Prakash, V. Salgaonkar, P. D. Jones, R. N. Cam, M. Han, V. Rieke, E. C. Burdette, and C. J. Diederich, "Interstitial ultrasound ablation of tumors within or adjacent to bone: Contributions of preferential heating at the bone surface," in *SPIE BiOS.* International Society for Optics and Photonics, 2013, pp. 85 840Z–85 840Z.

[64] P. Prakash, V. A. Salgaonkar, E. C. Burdette, and C. J. Diederich, "Hepatic ablation with multiple interstitial ultrasound applicators: initial ex vivo and computational studies," in *SPIE BiOS*. International Society for Optics and Photonics, 2011, pp. 79 010R–79 010R.

[65] S. Eslami, W. Shang, G. Li, N. Patel, G. S. Fischer, J. Tokuda, N. Hata, C. M. Tempany, and I. Iordachita, "In-bore prostate transperineal interventions with an MRI-guided parallel manipulator: system development and preliminary evaluation," *The International Journal of Medical Robotics and Computer Assisted Surgery*, 2015.

[66] H. Su, W. Shang, G. Cole, G. Li, K. Harrington, A. Camilo, J. Tokuda, C. M. Tempany, N. Hata, and G. S. Fischer, "Piezoelectrically-actuated robotic system for MRI-guided prostate percutaneous therapy," *Mechatronics, IEEE/ASME Transactions on*, vol. 99, no. 3, pp. 1–13, 2015.

[67] J. Tokuda, S. Song, K. Tuncali, C. Tempany, and N. Hata, "Configurable Automatic Detection and Registration of Fiducial Frames for Device-to-Image Registration in MRI-Guided Prostate Interventions," in *Medical Image Computing and Computer-Assisted Intervention–MICCAI 2013*. Springer, 2013, pp. 355–362.

[68] "American cancer society: key statistics about prostate cancer," http://www.cancer.org/cancer/prostatecancer/detailedguide/prostate-cancer-key-statistics, 2016.

[69] G. J. Kelloff, P. Choyke, and D. S. Coffey, "Challenges in clinical prostate cancer: role of imaging," *AJR. American journal of roentgenology*, vol. 192, no. 6, p. 1455, 2009.

[70] M. Han, D. Chang, C. Kim, B. J. Lee, Y. Zuo, H.-J. Kim, D. Petrisor, B. Trock, A. W. Partin, R. Rodriguez *et al.*, "Geometric evaluation of systematic transrectal ultrasound guided prostate biopsy," *The Journal of urology*, vol. 188, no. 6, pp. 2404–2409, 2012.

[71] H. Hricak, P. L. Choyke, S. C. Eberhardt, S. A. Leibel, and P. T. Scardino,

"Imaging prostate cancer: A multidisciplinary perspective 1," *Radiology*, vol. 243, no. 1, pp. 28–53, 2007.

[72] R. C. Susil, C. Mard, A. Krieger, J. A. Coleman, K. Camphausen, P. Choyke, G. Fichtinger, L. L. Whitcomb, C. N. Coleman, and E. Atalar, "Transrectal prostate biopsy and fiducial marker placement in a standard 1.5T magnetic resonance imaging scanner." *J Urol*, vol. 175, no. 1, pp. 113–120, Jan 2006.

[73] D. Beyersdorff, A. Winkel, B. Hamm, S. Lenk, S. A. Loening, and M. Taupitz, "MR Imaging–guided Prostate Biopsy with a Closed MR Unit at 1.5 T: Initial Results 1," *Radiology*, vol. 234, no. 2, pp. 576–581, 2005.

[74] A. V. D'Amico, C. M. Tempany, R. Cormack, N. Hata, M. Jinzaki, K. Tuncali, M. Weinstein, and J. P. Richie, "Transperineal magnetic resonance image guided prostate biopsy." *J Urol*, vol. 164, no. 2, pp. 385–387, Aug 2000.

[75] T. Penzkofer, K. Tuncali, A. Fedorov, S. Song, J. Tokuda, F. M. Fennessy, M. G. Vangel, A. S. Kibel, R. V. Mulkern, W. M. Wells *et al.*, "Transperineal In-Bore 3-T MR Imaging–guided Prostate Biopsy: A Prospective Clinical Observational Study," *Radiology*, vol. 274, no. 1, pp. 170–180, 2014.

[76] D. Yakar, M. G. Schouten, D. G. Bosboom, J. O. Barentsz, T. W. Scheenen, and J. J. Fütterer, "Feasibility of a pneumatically actuated MR-compatible robot for transrectal prostate biopsy guidance," *Radiology*, vol. 260, no. 1, pp. 241–247, 2011.

[77] G. Tilak, K. Tuncali, S. Song, J. Tokuda, O. Olubiyi, F. Fennessy, A. Fedorov, T. Penzkofer, C. Tempany, and N. Hata, "3T MR-guided in-bore transperineal prostate biopsy: A comparison of robotic and manual needle-guidance templates," *Journal of Magnetic Resonance Imaging*, vol. 42, no. 1, pp. 63–71, 2015.

[78] A. Fedorov, R. Beichel, J. Kalpathy-Cramer, J. Finet, J.-C. Fillion-Robin, S. Pujol, C. Bauer, D. Jennings, F. Fennessy, M. Sonka *et al.*, "3D Slicer as an image computing platform for the Quantitative Imaging Network," *Magnetic resonance imaging*, vol. 30, no. 9, pp. 1323–1341, 2012.

[79] A. Fedorov, K. Tuncali, F. M. Fennessy, J. Tokuda, N. Hata, W. M. Wells, R. Kikinis, and C. M. Tempany, "Image registration for targeted MRI-guided transperineal prostate biopsy," *Journal of Magnetic Resonance Imaging*, vol. 36, no. 4, pp. 987–992, 2012.

[80] J. Tokuda, K. Tuncali, I. Iordachita, S. Song, A. Fedorov, S. Oguro, A. Lasso, F. M. Fennessy, C. M. Tempany, and N. Hata, "In-bore setup and software for 3T MRI-guided transperineal prostate biopsy," *Physics in medicine and biology*, vol. 57, no. 18, p. 5823, 2012.

[81] S. Eslami, G. S. Fischer, S. Song, J. Tokuda, N. Hata, C. M. Tempany, and I. Iordachita, "Towards Clinically Optimized MRI-Guided Surgical Manipulator for Minimally Invasive Prostate Percutaneous Interventions: Constructive Design," in *Robotics and Automation (ICRA), 2013 IEEE International Conference on.* IEEE, 2013, pp. 1228–1233.

[82] "Neuron robotics: Bolwer protocol," http://neuronrobotics.com/Bowler-Protocol/Overview, 2015.

[83] G. Ploussard, J. I. Epstein, R. Montironi, P. R. Carroll, M. Wirth, M.-O. Grimm, A. S. Bjartell, F. Montorsi, S. J. Freedland, A. Erbersdobler *et al.*, "The contemporary concept of significant versus insignificant prostate cancer," *European urology*, vol. 60, no. 2, pp. 291–303, 2011.

[84] T. A. Stamey, F. Freiha, J. McNeal, E. Redwine, A. Whittemore, and H. Schmid, "Localized prostate cancer," *Cancer*, vol. 71, no. S3, pp. 933–38, 1993.

[85] H. Su, W. Shang, K. Harrington, A. Camilo, G. A. Cole, J. Tokuda, C. Tempany, N. Hata, and G. S. Fischer, "A Networked Modular Hardware and Software system for MRI-guided Robotic Prostate Interventions," in *SPIE Medical Imaging (Image-Guided Procedures, Robotic Interventions, and Modeling Conference)*, San Diego, USA, 2012.

[86] D. C. Rucker, J. Das, H. B. Gilbert, P. J. Swaney, M. Miga, N. Sarkar, R. J. Webster *et al.*, "Sliding mode control of steerable needles," *Robotics, IEEE Transactions on*, vol. 29, no. 5, pp. 1289–1299, 2013.

[87] K. B. Reed, A. Majewicz, V. Kallem, R. Alterovitz, K. Goldberg, N. J. Cowan, and A. M. Okamura, "Robot-assisted needle steering," *Robotics & Automation Magazine, IEEE*, vol. 18, no. 4, pp. 35–46, 2011.

[88] D. S. Minhas, J. A. Engh, M. M. Fenske, and C. N. Riviere, "Modeling of needle steering via duty-cycled spinning," in *Engineering in Medicine and Biology Society, 2007. EMBS 2007. 29th Annual International Conference of the IEEE*. IEEE, 2007, pp. 2756–2759.

[89] G. J. Vrooijink, M. Abayazid, S. Patil, R. Alterovitz, and S. Misra, "Needle path planning and steering in a three-dimensional non-static environment using two-dimensional ultrasound images," *International Journal of Robotics Research (In Proof)*, 2014.

[90] M. Bernardes, B. V. Adorno, P. Poignet, and G. Borges, "Robot-assisted automatic insertion of steerable needles with closed-loop imaging feedback and intraoperative trajectory replanning," *Mechatronics*, vol. 23, no. 6, pp. 630–645, 2013.

[91] S. Patil, J. Burgner, R. J. Webster, and R. Alterovitz, "Needle steering in 3-D via rapid replanning," *Robotics, IEEE Transactions on*, vol. 30, no. 4, pp. 853–864, 2014.

[92] A. Majewicz, J. J. Siegel, A. A. Stanley, and A. M. Okamura, "Design and evaluation of duty-cycling steering algorithms for robotically-driven steerable needles," in *Robotics and Automation (ICRA), 2014 IEEE International Conference on*. IEEE, 2014, pp. 5883–5888.

[93] R. J. Webster, J. M. Romano, and N. J. Cowan, "Mechanics of precurved-tube continuum robots," *Robotics, IEEE Transactions on*, vol. 25, no. 1, pp. 67–78, 2009.

[94] R. J. Webster III, *Design and mechanics of continuum robots for surgery*, 2008, vol. 69, no. 04.

[95] R. M. Murray, Z. Li, S. S. Sastry, and S. S. Sastry, *A mathematical introduction to robotic manipulation*. CRC press, 1994.

[96] N. A. Patel, T. van Katwijk, G. Li, P. Moreira, W. Shang, S. Misra, and G. S. Fischer, "Closed-loop asymmetric-tip needle steering under continuous intraoperative MRI guidance," in *Engineering in Medicine and Biology Society (EMBC), 2015 37th Annual International Conference of the IEEE*. IEEE, 2015, pp. 4869–4874.

[97] W. Shang, H. Su, G. Li, and G. S. Fischer, "Teleoperation system with hybrid pneumatic-piezoelectric actuation for MRI-guided needle insertion with haptic feedback," in *Intelligent Robots and Systems (IROS), 2013 IEEE/RSJ International Conference on*. IEEE, 2013, pp. 4092–4098.

[98] G. Li, H. Su, W. Shang, J. Tokuda, N. Hata, C. M. Tempany, and G. S. Fischer, "A fully actuated robotic assistant for MRI-guided prostate biopsy and brachytherapy," in *SPIE Medical Imaging*. International Society for Optics and Photonics, 2013, pp. 867 117–867 117.

[99] C. Bergeles, A. H. Gosline, N. V. Vasilyev, P. J. Codd, P. J. del Nido, and P. E. Dupont, "Concentric tube robot design and optimization based on task and anatomical constraints," *Robotics, IEEE Transactions on*, vol. 31, no. 1, pp. 67–84, 2015.

[100] T. Duerig, A. Pelton, and D. Stöckel, "An overview of nitinol medical applications," *Materials Science and Engineering: A*, vol. 273, pp. 149–160, 1999.

[101] D. Rucker, B. Jones, and R. J. Webster III, "A geometrically exact model for externally loaded concentric-tube continuum robots," *Robotics, IEEE Transactions on*, vol. 26, no. 5, pp. 769 –780, oct. 2010.

[102] J. Lock, G. Laing, M. Mahvash, and P. E. Dupont, "Quasistatic modeling of concentric tube robots with external loads," in *Intelligent Robots and Systems (IROS), 2010 IEEE/RSJ International Conference on*. IEEE, 2010, pp. 2325–2332.

[103] H. Su, D. Cardona, W. Shang, A. Camilo, G. Cole, D. Rucker, R. Webster, and G. Fischer, "MRI-guided concentric tube continuum robot with piezoelectric actuation: a feasibility study," in *Robotics and Automation (ICRA), IEEE International Conference on*, 2012, pp. 1939–1945.

[104] R. Lathrop, D. C. Rucker, R. J. Webster III *et al.*, "Guidance of a steerable cannula robot in soft tissue using preoperative imaging and conoscopic surface contour sensing," in *Robotics and Automation (ICRA), 2010 IEEE International Conference on*. IEEE, 2010, pp. 5601–5606.

[105] H. Su, G. Li, D. C. Rucker, R. J. Webster III, and G. S. Fischer, "A Concentric Tube Continuum Robot with Piezoelectric Actuation for MRI-Guided Closed-Loop Targeting," *Annals of Biomedical Engineering*, pp. 1–11, 2016.

[106] V. Kallem and N. J. Cowan, "Image-guided control of flexible bevel-tip needles," in *Robotics and Automation, 2007 IEEE International Conference on*. IEEE, 2007, pp. 3015–3020.

[107] M. C. Bernardes, B. V. Adorno, P. Poignet, G. A. Borges *et al.*, "Semi-automatic needle steering system with robotic manipulator." in *ICRA*, 2012, pp. 1595–1600.

[108] J. P. Swensen, M. Lin, A. M. Okamura, and N. J. Cowan, "Torsional dynamics of steerable needles: modeling and fluoroscopic guidance," *Biomedical Engineering, IEEE Transactions on*, vol. 61, no. 11, pp. 2707–2717, 2014.

[109] A. Asadian, R. V. Patel, and M. R. Kermani, "Dynamics of translational friction in needle–tissue interaction during needle insertion," *Annals of biomedical engineering*, vol. 42, no. 1, pp. 73–85, 2014.

[110] E. Dehghan, X. Wen, R. Zahiri-Azar, M. Marchal, and S. E. Salcudean, "Needle-tissue interaction modeling using ultrasound-based motion estimation: Phantom study," *Computer Aided Surgery*, vol. 13, no. 5, pp. 265–280, 2008.

[111] P. J. Swaney, J. Burgner, H. B. Gilbert, and R. J. Webster, "A flexure-based steerable needle: high curvature with reduced tissue damage," *Biomedical Engineering, IEEE Transactions on*, vol. 60, no. 4, pp. 906–909, 2013.